Shape distortions in fabric reinforced composite products due to processing induced fibre reorientation

E.A.D. Lamers

This thesis was written at the University of Twente within the framework of the Brite Euram project *PRECIMOULD* (BE97–4351) and the NIVR project *High Precision Rubber Pressing* (BRP 49209UT).

Samenstelling van de promotiecommissie:

voorzitter en secretaris:	
Prof. dr. ir. H.J. Grootenboer	Universiteit Twente
promotoren:	
Prof. dr. ir. R. Akkerman	Universiteit Twente
Prof. dr. ir. J. Huétink	Universiteit Twente
leden:	
Prof. ir. A. Beukers	Technische Universiteit Delft
Prof. A.C. Long	University of Nottingham
Prof. dr. ir. J.J.M. Slot	Universiteit Twente
Prof. dr. ir. M.M.C.G. Warmoeskerken	Universiteit Twente

CIP-GEGEVENS KONINKLIJKE BIBLIOTHEEK, DEN HAAG

Lamers, E.A.D.

Shape distortions in fabric reinforced composite products due to processing induced fibre reorientation/
E.A.D. Lamers – Ill.
Thesis Enschede, – With ref.
ISBN 90-365-2043-6
1st Printing April 2004
Subject headings: distortions, composites, draping, FE-modelling, composites forming

Printed by FEBO druk, Enschede.

SHAPE DISTORTIONS IN FABRIC REINFORCED COMPOSITE PRODUCTS DUE TO PROCESSING INDUCED FIBRE REORIENTATION

PROEFSCHRIFT

ter verkrijging van
de graad van doctor aan de Universiteit Twente,
op gezag van de rector magnificus,
prof. dr. F.A. van Vught,
volgens besluit van het College voor Promoties
in het openbaar te verdedigen
op vrijdag 23 april 2004 om 16.45 uur

door

Edwin Adriaan Derk Lamers

geboren op 2 september 1972
te Hengelo

Dit proefschrift is goedgekeurd door de promotoren:

Prof. dr. ir. R. Akkerman
Prof. dr. ir. J. Huétink

Summary

Woven fabric reinforced composite materials are typically applied in plate or shell structures, such as ribs, stiffeners and skins. Products of these types can be produced with several production processes. A few examples are diaphragm forming, matched metal die forming and rubber press forming. Shape distortions can occur during manufacturing of composite products. During the development stage of the products these distortions often exceed the high dimensional accuracy required in, for example, the aeronautical and car industry. Costly trial and error methods are generally applied to meet the dimensional accuracy. Modelling the shape distortions on beforehand can aid to reduce the development costs of these products.

To predict shape distortions, the mechanical properties (stiffness) and thermal expansion behaviour (shrinkage and warpage), referred to as thermo–elastic properties, of the product need to be included in the model. The distortions can be introduced by, for example, thermal loading or stresses induced by forming. Obviously, the materials used and the lay–up of the composite affect the resulting behaviour. However, due to processing induced fibre reorientation, the thermo–elastic properties of the composite change locally as a function of the fibre reorientation. The fibre arrangement and resulting local composite properties need to be taken into account in order to model the product distortions.

Here, the objective is to model the shape distortions using a Finite Element method with computationally effective plate elements. First, the fibre reorientation during processing is predicted, including the processing induced fibre stresses. The processing induced fibre reorientation, or draping, is considered for single– and multi–layered bi–axial fabric composites. The material model accounts for the intra– and inter–ply shear behaviour of these composites. The drape model predicts a clear dependency between the drape–ability and lay–up of multi–layered composites. Experiments on rubber press formed fabric reinforced thermoplastic laminates confirm this dependency.

Secondly, the product distortions are predicted, accounting for the locally changed composite properties due to the fibre reorientation during forming. A weave model, to predict the thermo–elastic properties of the deformed weave while accounting for the local structure of the weave, is combined with the results from the drape model. The results are validated on the shape distortions of a woven fabric reinforced thermoplastic composite with a double dome geometry. Additionally, the shape distortions of a hemispherical product and a wing leading edge stiffener are demonstrated.

Contents

Summary **v**

1 Introduction **1**
1.1 Composite materials . . . 1
1.1.1 Fabric reinforced composites . . . 3
1.2 Production methods . . . 3
1.2.1 Thermosetting composites . . . 4
1.2.2 Thermoplastic composites . . . 4
1.3 Thermo–elastic properties . . . 5
1.4 Scope of the thesis . . . 6
1.5 Outline of the thesis . . . 6

2 Drape material model **9**
2.1 Review on draping . . . 9
2.1.1 Discrete approach . . . 10
2.1.2 Continuum approach . . . 12
2.1.3 Draping of multi–layered composites . . . 14
2.2 Material model for draping . . . 15
2.2.1 Single layer material model . . . 15
2.2.2 Multi–layer material model . . . 20
2.3 Characterising material properties . . . 22
2.3.1 Picture Frame tests . . . 22
2.3.2 Pull–out tests . . . 28
2.4 Conclusions . . . 29
2.5 Recommendations . . . 29

3 Finite Element drape modelling **31**
3.1 Updated Lagrangian implicit Finite Element method . . . 31
3.1.1 Updated Lagrangian method . . . 32
3.1.2 Implicit Finite Element method . . . 32
3.2 Single layer material model implementation . . . 33
3.2.1 Fibre direction update . . . 33
3.2.2 Stress update . . . 33
3.2.3 Material tensor . . . 34
3.3 Multi–layer material model implementation . . . 35
3.3.1 Ply deformations . . . 35
3.3.2 Fibre direction update . . . 38
3.3.3 Stress update . . . 39

3.3.4 Material tensor . . . 40
3.3.5 Convection of the state variables . . . 40
3.4 Simulation control and boundary conditions . . . 43
3.4.1 Simulation Control . . . 43
3.4.2 Boundary conditions . . . 43
3.5 Drape experiments . . . 44
3.6 Drape simulations . . . 45
3.6.1 Geometrical draping . . . 45
3.6.2 Finite Element draping . . . 46
3.7 Discussion . . . 48
3.7.1 Global drape behaviour . . . 48
3.7.2 Verification of the fibre redistribution . . . 49
3.7.3 Stresses induced by draping . . . 51
3.7.4 Multi–layer model versus multiple membrane elements through–the–thickness . . . 53
3.8 Conclusions . . . 55
3.9 Recommendations . . . 55

4 Woven fabric composite properties 57
4.1 Review on thermo–elastic modelling . . . 57
4.2 Methodology . . . 58
4.3 Geometrical analysis . . . 59
4.3.1 Macro level geometrical modelling . . . 59
4.3.2 Meso level geometrical modelling . . . 60
4.3.3 Mini level geometrical modelling . . . 61
4.3.4 Micro level geometrical modelling . . . 67
4.4 Thermo–elastic analysis . . . 68
4.4.1 Micro level thermo–elastic modelling . . . 68
4.4.2 Mini level thermo–elastic modelling . . . 69
4.4.3 Meso level thermo–elastic modelling . . . 73
4.4.4 Macro level thermo–elastic modelling . . . 76
4.5 Woven fabric model verification . . . 77
4.5.1 Mechanical testing . . . 77
4.5.2 Thermal testing . . . 78
4.6 Results and discussion . . . 79
4.6.1 Mechanical . . . 81
4.6.2 Thermal . . . 83
4.7 Conclusion . . . 84
4.8 Recommendations . . . 84

5 Thermo–elastic properties of doubly curved products 87
5.1 Review . . . 87
5.2 Strategy . . . 88
5.2.1 From draping to cooling . . . 89
5.2.2 Thermo–elastic loading . . . 90
5.2.3 Finite Element implementation . . . 90
5.3 Shape distortions of products . . . 90
5.3.1 Double dome geometry . . . 90

5.3.2 Hemispherical product 92
5.3.3 Wing leading edge stiffener 94
5.4 Conclusion 97
5.5 Recommendations 97

6 Conclusions and recommendations **99**

A Continuum mechanics **113**
A.1 Kinematics 113
A.1.1 Coordinate systems 114
A.1.2 Deformation 115
A.1.3 Vector kinematics 116
A.2 Strain measures 117
A.3 Stress measures 118
A.4 The equilibrium problem 118
A.4.1 Weak form 119

B Material model implementation **121**
B.1 Single layer fibre update 121
B.2 Material tensor 122

C Drape material model verification **125**
C.1 Molenkamp test 125

D Drape applications **127**
D.1 Sphere 127
D.2 Cone 128
D.3 Rib 129

Chapter 1

Introduction

Over the last years, the demand for high stiffness and strength and low weight materials, such as fibre reinforced plastics, has grown in the transport industry. Especially in the aeronautical industry, the use of fabric reinforced plastics increased significantly. By decreasing the production cost with short production cycle times and increasing reproducibility by automation, fabric reinforced plastics are becoming better economical competitors to other construction materials such as aluminium. Typically, thin walled structures are produced with composite materials.

The advantages of continuous fibre reinforced composites are: high strength combined with low weight and the ability to lay–up the fibres with the strength in the required direction, enabling an optimised design of the structure. Obviously these combinations are desirable in the aircraft industry and therefore increasingly used in airframe components.

However, the expected growth in composite applications predicted in the late 70's has not been achieved. Shrinkage and warpage during production can result in unacceptable dimensional change of the products. Incapacity of current models to predict these distortions is one of the reasons for making the engineer reluctant to use the composite materials. Fibre reorientation is one of the major factors causing these dimensional changes. Especially when producing doubly curved parts, the process of draping causes the angle between the warp and fill yarns to vary over the product with this double curvature. As a result of this reorientation, the thermo–elastic properties of the fibre reinforced composite material show a corresponding distribution, in turn leading to a distribution of residual stresses.

The Brite Euram research project *PRECIMOULD* (BE97–4351) and the Netherlands Agency for Aerospace Programs supported project *High Precision Rubber Pressing* (BRP 49209UT), were initiated in order to solve these production related problems. The *PRECIMOULD* project focussed on shape distortions in thermosetting composite materials whereas the *High Precision Rubber Pressing* project focussed on the use of thermoplastic composite materials. This thesis is written within the framework of these projects.

1.1 Composite materials

Composites are used in various forms [60]. The field of composites is restricted to a combination of fibres and plastics in this research. The fibres are embedded in the

plastic, which acts as a force transducer and holds the fibres in place. The plastic and fibres have very dissimilar properties. The plastic, a polymer material, generally has a low modulus and strength while it has a high thermal expansion and high capacity to absorb moisture. Normally, the plastic behaves isotropically. The fibres have a relatively high strength and modulus and a low thermal expansion and low capacity to absorb moisture compared to the plastic. Several fibre materials are anisotropic by nature. Many possible combinations of fibres and plastics are employed: short fibre, long fibre and continuous fibre reinforced plastics.

The first form, short fibre reinforced plastic, has fibres up to approximately five millimetres. This type of reinforcement is primarily used in injection moulding applications in combination with thermoplastics. The effect of the reinforcement is not very significant, it merely increases the properties of the plastic. Production cycle times are relatively short, generally up to one minute.

The second form, long fibre reinforced plastic, is employed with both thermosetting and thermoplastic materials. The fibre length in these materials ranges from approximately 5 millimetres up to five centimetres. Most of the fibres are oriented in the plane of the product after forming since the wall thickness in these products is generally smaller than the length of the fibres. Therefore, the through–thickness properties can differ significantly from the in–plane properties. The structural efficiency of the reinforcement is low, but the properties of the composite are significantly better than those of pure plastic. Some widely employed production methods are hand lay–up, compression moulding and press–forming. Production cycle times are generally longer than with injection moulding applications. The production times range from several minutes up to several hours.

The third form, continuous fibre reinforced composites, is primarily used with thermosetting matrix materials, but the use with thermoplastics is increasing. The fibres are arranged in, for example, unidirectional plies or fabrics. Layers are stacked on top of each other, resulting in a laminate. The material properties are dominated by the fibres, which are mainly oriented in the plane of the product. As a result, the through–thickness properties generally differ significantly from the in–plane properties of the material. The reinforcement is structurally most efficient with this combination of fibres and plastic, compared to short and long fibre reinforced plastics. Typical production methods are hand lay–up, liquid composite moulding, autoclave–forming and press–forming. Most processes with thermosetting materials are labour intensive, slow and expensive. The production cycle times are often several hours when using thermosetting plastics, due to the curing time of the thermosetting material. Automated production with these composite materials is not widely employed. The production costs can be reduced by automation and reduction of production cycle time. Cycle times can be reduced when using thermoplastic materials since the cooling times of thermoplastics are significantly shorter than the curing times of thermosetting materials. Typically, the production cycle time with thermoplastic materials is in the order of minutes.

The composites considered in this thesis are continuous fibre reinforced plastics. Here, the continuous fibres are arranged in woven fabrics, one of the most employed reinforcement architectures. The woven fabrics, or weaves, are easily handled and widely available. The production of weaves is automated, resulting in a reproducible, high quality material. Manufacturers produce both dry and pre–impregnated fabrics. Thermosetting or thermoplastic polymers can be used to impregnate the weaves.

1.1.1 Fabric reinforced composites

Bi–axially woven fabrics are considered in this thesis. These fabrics are woven from two fibre families. The two fibre directions are called warp and fill direction, respectively. The fibres are combined into bundles, often referred to as yarns. Each yarn can consist of several thousand fibres.

The warp and fill yarns are arranged into weave patterns. The weave pattern, such as a plain weave or a satin weave pattern, affects the behaviour of the weave, both during the forming stages and when the product is in use. Examples of a plain weave and a satin weave are presented in figure 1.1.

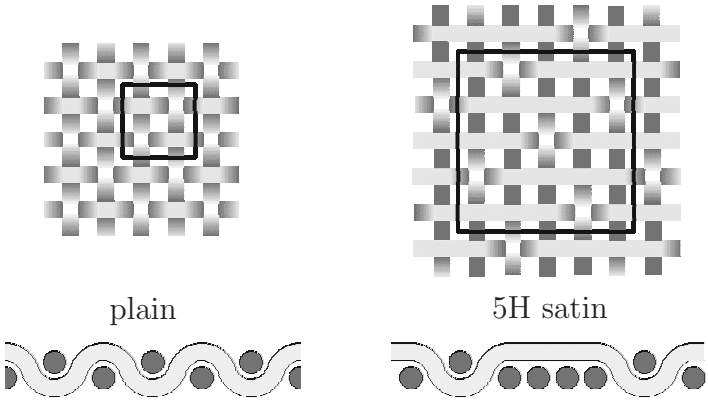

Figure 1.1: Schematic representation of a plain weave and a 5 harness satin weave.

The plain weave on the left–hand side in figure 1.1 shows the typical one–over–one arrangement of the warp and fill yarns. A repetitive unit, or Repetitive Volume Element (RVE), is indicated with a black square. RVE's are the smallest parts that can represent the complete weave. The size of the plain weave unit cell is two–by-two yarns. A five harness satin (5H satin) weave is presented on the right–hand side of figure 1.1. Each yarn passes over four yarns and then under one yarn of the other direction. The size of a 5H satin unit cell is five–by–five yarns.

The weave pattern is *balanced* if the amount of warp and fill fibres on each side of the weave per unit area is equal. The weave is *regular* if the amount of warp and fill fibres per unit width is the same. The number of fibres per unit width is often referred to as the yarn count. Plain weaves are both balanced and regular for most applications. Satin weaves can be regular but never balanced, either more warp or fill fibres are on a side of the weave.

The advantages of these materials are their ease of use and good in–plane deformability. Weaves deform hardly in the fibre directions but can undergo large shear deformations. Shear is the main deformation mode during composite forming operations.

1.2 Production methods

Many production methods [52, 60] are applied to manufacture woven fabric reinforced composites. These methods can be split into two groups: methods to manufacture

thermosetting composite products and methods to manufacture thermoplastic composite products.

1.2.1 Thermosetting composites

Several production methods are available for manufacturing thermosetting composite products. The mostly employed methods are; hand lay–up, liquid composite moulding and autoclave–forming.

The hand lay–up production method is used when very small series of products are produced. The dry or pre–impregnated fabric is draped onto the mould by hand. The draped fabric is wetted with the uncured thermosetting polymer if required. Repetitively, new layers of fabric are placed onto the mould until the laminate has reached the required thickness. The product then cures on the mould and is released when it is sufficiently form stable.

Liquid composite moulding is applied when series of approximately 10 up to 1000 products have to be manufactured. The method is much better controllable than the hand lay–up method and can produce high quality products with a complicated geometry. It requires the production of a dry pre–form. The pre–form can either be draped onto the mould or produced by, for example, structural stitching. The dry pre–form is placed in a closed mould, where it is injected with the uncured thermosetting polymer. The composite cures in the mould and the product is released when it is sufficiently form stable. Often a post–curing step is employed to fully cure the product.

Pre–impregnated thermosetting fabric composites are mostly formed in autoclave processes. The impregnated fabric is stacked onto the mould until the required laminate thickness is obtained. The laminate then is compressed in the autoclave, and the curing cycle starts. The product is released after curing.

The production of thermosetting fabric reinforced composites is labour intensive. Especially the stacking of the laminate requires significant human resource. The curing of the composite often requires several hours, thereby increasing the manufacturing time dramatically. The production methods are slow and expensive, but can be used for complex products up to several metres.

1.2.2 Thermoplastic composites

Thermoplastic fabric reinforced composites are generally used in pre–impregnated form. The pre–impregnated fabrics are formed using thermo–forming processes. Three generally used methods are: autoclave–forming, diaphragm–forming and press–forming.

The production of thermoplastic composites is similar to the production of thermosetting composites in case autoclave–forming is applied. First, the individual layers are stacked onto the mould. Then, the laminate and mould are placed into the autoclave where it is pressurised, heated, consolidated and subsequently cooled. The product is released from the mould when it is sufficiently form stable. Production cycle times are generally shorter with thermoplastic composites than with thermosetting composites. The production time is reduced since cooling of the thermoplastic matrix material uses less time than the curing of the thermosetting material. The production of thermoplastic and thermosetting composites is however, as labour intensive with autoclave–forming.

A pre–form of impregnated layers of fabric is produced prior to diaphragm–forming. This pre–form is placed between two diaphragms and subsequently heated until the

polymer is molten. The whole package is hydrostatically pressed on the mould to ensure consolidation. The laminate is cooled and subsequently released from the mould. The production cycle times are relatively short. The vacuum–bagging of the pre–form is however fairly labour intensive.

A flat laminate plate of several square metres is produced prior to forming for the press–forming production method. The production of flat plates is automated, and pre–forms are cut from these flat plates prior to pressing. The pre–form is heated, and subsequently pressed onto the mould. The product is consolidated and then cooled until it is form stable before it is released from the mould. Cutting and pressing can be automated straightforwardly. Pressing cycle times are within minutes, and the whole production method is therefore suitable for mass–production.

1.3 Thermo–elastic properties

The stiffness properties of the plastic material are significantly lower than those of the fibre materials. As a result, the stiffness in the longitudinal direction of the fibres is significantly higher than the stiffness properties in the transverse direction. Therefore, the stiffness of the composite material depends highly on the orientation of the fibres. The composite is generally builtup from several plies. More homogeneous stiffness properties can be achieved by orientating these plies, or laminae, in different directions and stacking them on top of each other. The stacking sequence, or lay–up, significantly influences the stiffness properties of the laminates.

The thermal expansion of the fibre material is generally significantly lower than the thermal expansion of the plastic. A relatively low thermal expansion in the longitudinal fibre direction of the composite results from this. The thermal expansion of the composite is significantly higher in the transverse direction. The response of the laminate to a uniform change in temperature therefore depends on the lay–up, similarly to the stiffness properties of the composite.

The Classical Laminate Theory (CLT) [56] is based on Kirchhoff's plate theory and well capable of modelling the in–plane properties of laminates built from unidirectional plies. The mechanical response to loading, determined by the stiffness properties, and the deformations due to a homogeneous change in temperature, or thermal behaviour, are covered by this theory. The mechanical properties coupled with the thermal behaviour of composite products are called thermo–elastic properties. Obviously, also the fibre volume fraction, or the ratio between the volume of all fibres and the total volume, will strongly influence the thermo–elastic properties. Normally, the CLT is applied to flat laminates, with plies of constant thickness, having homogeneous ply properties. Unidirectional micromechanical models are generally used to predict these ply properties [80].

This thesis considers fabric reinforced plastics. The CLT cannot be applied directly to the composite due to the weave pattern and the undulation of the yarns in the fabric. Several authors [1, 18, 19, 25, 49, 50, 76, 77] have modelled the thermo–elastic properties of orthogonal weaves. Little work has been done to model the properties of weaves that have lost their orthogonality due to forming.

1.4 Scope of the thesis

When forming a flat woven fabric composite laminate, into doubly curved products, the originally orthogonal arrangement of the yarns in the weave becomes highly disturbed during the forming operation. This fibre reorientation is widely accepted and modelled using a variety of techniques [8, 11, 15, 40, 55, 59]. As a result of this reorientation, the thermo–elastic properties of the fibre reinforced composite material show a corresponding distribution. The inhomogeneous distribution of the thermo–elastic properties in the product result in a distribution of residual stresses during the production process. These stresses can result in unacceptable shape distortions of the product.

Modelling the shape distortions on beforehand and subsequently adapting the mould shape can minimise the occurring distortions. It is necessary to develop methods for the determination of the thermo–elastic properties of the products resulting from the forming technique. Predicting the thermo–elastic properties is not a straightforward exercise but necessary in the design and manufacturing of such a product.

The currently employed modelling techniques [28, 29, 71] determine, (a) the determination of the fibre re–arrangement within the product after pressing, (b) the thermo–elastic properties of composites built from non–orthogonal woven fabrics and (c) the combination of both to find the thermo–elastic properties of the product. The mechanical response of the structure due to loading can be determined with these thermo–elastic properties. Similarly, distortions such as the shrinkage and warpage of the product due to a temperature change can be predicted. The currently available modelling techniques have flaws in predicting the fibre re–arrangement after forming, are not fully capable of incorporating the thermo–elastic properties of woven fabric composite products, or are very complex. The aim of this thesis is to improve these modelling techniques.

Modelling would be comparable to the existing CLT already available for flat laminates, where the fibre orientation is predetermined and regularly arranged. In this thesis, the fibre reorientation due to production (draping) is predicted. Also, the CLT is extended to the prediction of properties for non–orthogonal weaves. Finally, both the results from draping and the thermo–elastic properties of non–orthogonal weaves are combined to model the resulting behaviour of a complete woven fabric reinforced composite product. The predicted thermo–elastic properties of the product are then applied to model the distortions of the products due to forming.

1.5 Outline of the thesis

The outline of this thesis follows the steps during forming and subsequent cooling of the product. A schematic representation of the modelling process is depicted in figure 1.2.

The forming stage of the initial flat composite pre–form (draping) is treated in chapters 2 and 3. Chapter 2 presents the constitutive behaviour of the composite material during forming. Chapter 3 describes the Finite Element implementation of this drape material model. In this chapter, the drpe model is extended to the fibre re–arrangement onto doubly curved surfaces. Next, a weave model to predict the thermo–elastic properties of flat woven fabric reinforced composites is given in chapter 4. The presented weave model extends the CLT to account for the undulation of the yarns in the weave and the

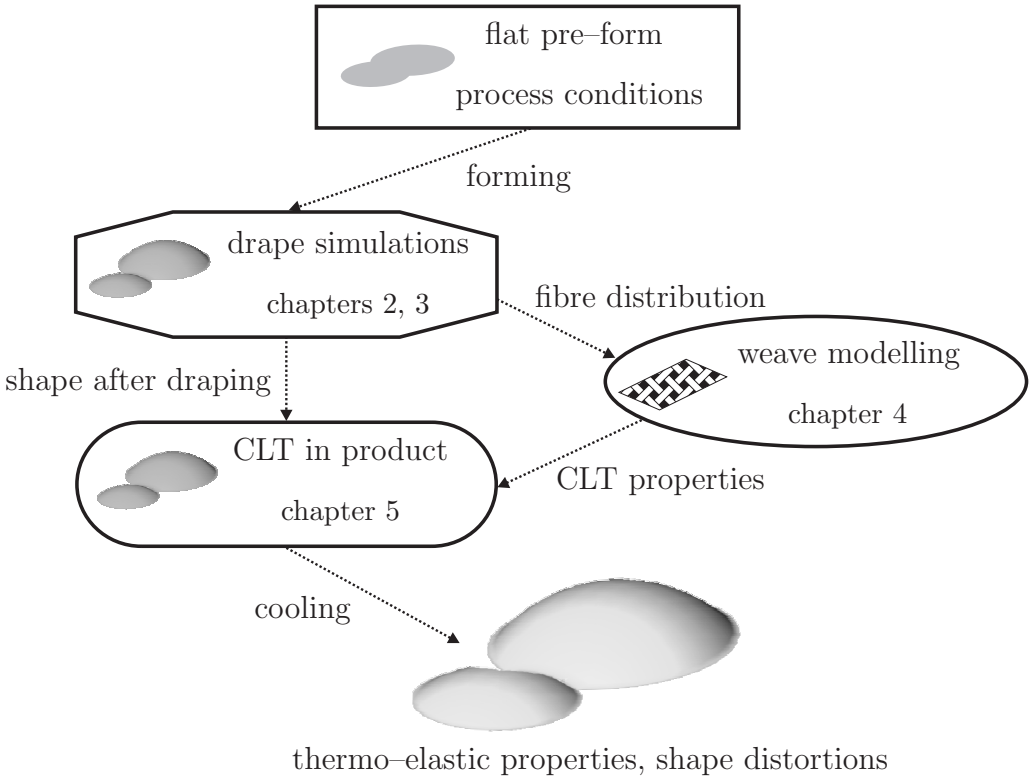

Figure 1.2: Schematic view on the modelling stages.

fabric architecture. This chapter is basically in intermediate stage in the modelling of the thermo–elastic properties of composite material since it merely models the properties of flat composites. Chapter 5 combines the results of the drape simulations with the weave model. The thermo–elastic properties of doubly curved composite products are predicted as a result, while accounting for the fibre re–arrangement during forming and the shape of the product. The distortions of the product are predicted as a function of the change in temperature. Finally, conclusions are drawn and recommendations given in chapter 6.

Chapter 2

Drape material model

Fibre reorientation occurs when forming a reinforced structure such as a fabric onto a doubly curved surface. A change in the angle between warp and fill yarns results from this. The composite properties change inhomogeneously, corresponding to the varying angle between warp and fill yarns. Many composite properties are determined by the angle between the warp and fill yarns, such as the mechanical properties, the coefficients of thermal expansion, the local fibre volume fractions, the local thickness and the permeability. The extent of the fibre reorientation is affected by the product shape and the forming process. Tensile stresses in the fabric yarns might occur during forming. Also, wrinkling risks are present due to the incapability of the fabric to deform any further beyond a maximum shear deformation. The local change in composite properties must be taken into account to predict the properties of a product. Modelling the draping process will predict the fibre orientations and stresses resulting from the production process, and help the engineer in the product development process. Here, a drape material model for bi–axially reinforced composite materials will be presented. The implementation of the drape material model in a Finite Element (FE) code is treated in chapter 3.

2.1 Review on draping

When forming composites, either a dry or pre–impregnated fabric can be draped over a mould. When forming a dry fabric over the mould, the result is a pre–form, which generally is then injected with a polymer. This method is generally called Liquid Composite Moulding (LCM).

When draping pre–impregnated composites, the fabric is embedded in the matrix material. Possibly, several plies are stacked into a laminate. The pre–form is heated above the glass transition or melting temperature of the polymer matrix, formed on the tool and subsequently cooled or cured until the product is form stable.

Various drape models for dry and pre–impregnated fabrics have been proposed in the past. Recently a review on the forming of composite sheet forming has been published by Lim and Ramakrishna [37]. Two approaches are distinguished in their review: the mapping approach and the mechanics approach. In this thesis, the models are split into two other approaches; the discrete approach and the continuum approach. This split is based on the representation of the material by the models.

The discrete and continuum based drape approaches will be discussed briefly in the next sections. Then, the draping of multi–layered composites will be discussed.

2.1.1 Discrete approach

Three schemes are distinguished in the discrete drape approach, the mapping schemes, the particle based schemes and the truss based schemes.

Mapping based schemes

Mapping schemes are most commonly employed in commercial packages to predict draping. A layer of fabric is represented by a square mesh which is fitted onto the drape surface. The mapping scheme is based on the assumption that the fabric mainly deforms due to shear deformation and fibre extension can be neglected. The resin, if present, is also neglected during the simulation. The fabric always remains in a fixed position on the draping surface after being mapped. The shape of the product must be represented in algebraic expressions when modelling draping with a mapping scheme.

Several methods are used for predicting the fibre reorientation of the fabric. The geometrical model, also referred to as the kinematics or fishnet model, is a widely used model to predict the resulting fibre reorientation for doubly curved fabric reinforced products. Based on a pinned–joint description of the weave, this model was initially described by Mack and Taylor in 1956 [40]. The model assumes inextensible fibres pinned together at their crossings, allowing free rotation at these joints. They analytically solved the fibre redistribution of a fabric orientated in the bias direction on the circumference of simple surfaces of revolution, such as cones, spheres and spheroids. The resulting fibre orientations were solved as a function of the constant height coordinate of the circumference.

From the early 80's up to the late 90's many authors presented numerically based drape solutions, based on the same assumptions as Mack and Taylor [40]. The author refers to Robertson *et al.* [58], Smiley *et al.* [67], Heisley and Haller [27], Long and Rudd [39], Bergsma [7] and Trochu *et al.* [73]. Typically, draping starts from an initial point and two initial fibre directions. Further points are then generated at a fixed equal distance from the previous points creating a mesh of quadrilateral cells. There is no unique solution for the geometrical drape method. This problem is generally solved by defining two fibre paths on the drape surface. In 1995 Bergsma [7] introduced "strategies" in order to find solutions for the drape algorithm, without pre–defining fibre paths. Bergsma [7] also included a basic mechanism to incorporate the locking phenomenon in his drape simulations.

Alternatively to the fishnet model, Van der Weeën [79] presented a computationally efficient energy based mapping method in 1991. Rather than creating a new cell on a geometric basis, the cell in the mesh is mapped onto the drape surface by minimising the elastic energy in the drape cell, while only accounting for the deformation energy used to extend the fibres.

The mapping scheme is quite simple in its application and implementation, and does not require a powerful computer. The results of the mapping scheme agrees well with reality if the product shape is convex.

However, the mapping schemes do not predict unique solutions. User interference or "strategies" are required to solve the drape problem. Inaccurate drape predictions are obtained with products where bridging occurs or when the pre–form slides over the mould during forming. The scheme is not suited to accurately incorporate the processing conditions during draping or to give an accurate representation of the

composite properties. Especially in tight weaves, the error of assuming a zero in–plane fabric shear stiffness during draping leads to errors. From the late 70's it is experimentally shown that the resin material also affects the deformation properties [55]. In addition, the geometrical approach might find infeasible solutions when draping products with holes.

Forming of multi–layered composites is simulated by repeatedly draping single layers of fabric, since the model only represents one layer of fabric. The computational times thus increase linearly with the number of fabric layers in the composite, while the through–thickness shear interaction between the individual layers is not accounted for.

Particle based schemes

From the first half of the 1990's particle based schemes are used to predict the fabric drape behaviour. The fabric, or cloth, is represented as a discontinuous sheet using micro–mechanical structural elements. These elements, also called particles, interact and must be chosen small enough to still represent the weave's behaviour.

An interacting particle model was developed by Breen *et al.* [11] in 1994. Energy functions define the interaction between the particles, placing the particles at the crossings of the yarns in the fabric. The energy contribution in the particles consists of thread repelling, thread stretching, thread bending, thread trellising and gravity. The total energy in the cloth is simply the sum of the energy of all particles. The modelling strategy for particle based solutions is generally time dependent [11]. In the first time step, the model accounts for the gravity and the collision between the cloth and the drape surface. In the next step a stochastic energy–minimising technique is used to find the local energy minima for the cloth. Finally, permutations are introduced to produce a more asymmetric final configuration.

Similarly to the energy based functions, also force based functions were developed for the interactions of the particles (Colombo *et al.* [20]). This representation method is applied in commercially available software [20], since it is computationally more attractive than the energy based particle interaction functions.

In 2002, Cordier and Magnenat-Thalmann [21] simulated the cloth behaviour on dressed virtual humans in real–time. They propose a hybrid drape algorithm combining the advantages of physically (particle) based and geometric deformations, avoiding the computationally expensive collision calculations as much as possible. The cloth is segmented into three sections in their simulations. Clothes that remain at constant distance to the drape body, are modelled in the first section. Typically, these are stretch clothes. In the second layer, the loose cloth follows predefined discs, representing the limbs. Finally, floating cloth such as skirts is represented in the third section. A force based particle method is used for modelling the floating cloth, incorporating the collision with the underlying body and the cloth itself. Their model shows that real–time modelling of cloth behaviour is feasible using middle range computers (up to 1GHz PC's).

The method requires the mechanical properties of the cloth and the product shape as input. Typically, the method is used for modelling the shape of hanging cloth on objects or humans in the fashion industry. The emphasis is therefore not the deformation and stresses within the fabric but the resulting shape of the cloth as a whole. Possibly, this is why no implementation in the technical industry has been found for this method in the literature.

Truss based schemes

Fabrics are woven using a periodic arrangement of fibre bundles. These periodic arrangements are called Repetitive Volume Elements (RVE), or unit cells. The fibres in these unit cells can be represented using trusses. The fibre interaction, such as shear–locking of the fabric, is modelled with diagonal stringers. In 1999, Kato *et al.* [32] proposed a fabric lattice model based unit cell representation.

Recently, Tanov and Brueggert [72] modelled the inflation of a car side airbag in an FE simulation, using a loosely woven fabric model. The yarns in the fabric were represented by pinned–joined bars with two locking springs on the diagonal of their unit cell. A schematic representation of this unit cell is depicted in figure 2.1(b).

Sharma and Sutcliffe [65] also represented the unit cell in a network of pinned–joined trusses in 2003. The edge trusses represent the fibres in the fabric. To introduce shear stiffness in the unit cell, one diagonal spring is introduced, as presented in figure 2.1(a). An FE analysis is performed with this pinned–joined net of trusses, resulting in a drape prediction.

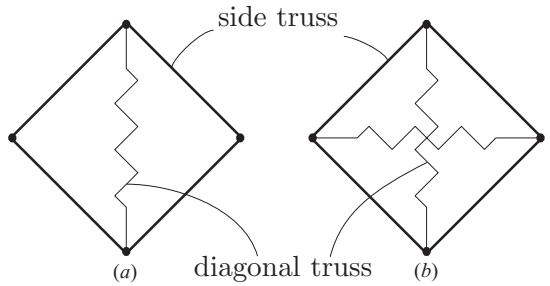

Figure 2.1: Schematic representation of the unit cell by truss elements; (a) one diagonal spring element (b) two diagonal spring elements.

The advantage of these model are the simple mechanics and ease of use. Little input is required and the simulation time is relatively short compared to continuum based approaches.

The resin behaviour is not incorporated into these models. The forming of multi–layered composites is done similarly to the mapping schemes 2.1.1 since also these models are based on the representation of a single layer of fabric. Through–thickness shear interaction between the fabric layers during forming is not accounted for.

2.1.2 Continuum approach

Several constitutive models were proposed for modelling fabric draping. They are based on elastic material models, viscous material models or multi–component models. Most constitutive material laws are formulated in plate or shell theory. Generally, the models are implemented in FE formulations. The models are described below.

Elastic Models

Since the mid nineties FE simulations with elastic models were applied. One of the earliest models was applied by Chen and Govindaraj [15]. They developed an elastic orthotropic continuum based model to represent the fabric drape behaviour. The material model was based on a flexible shell theory. A non–linear FE formulation was used to predict the forming of a fabric onto a table.

At the same time, Kang and Yu [31] developed a similar shell based drape model. They used a convective coordinate system in a total Lagrangian formulation with an orthotropic continuous based elastic material model. A Newton rootfinding method was used to solve the incremental formulation of the total Lagrangian scheme. Again, the draping of a cloth onto a table was simulated.

A few years later Boisse *et al.* [8] modelled the bi–axial fabric behaviour in forming processes. The undulation of the yarns in the fabric was accounted for in the bi–axial weave model, assuming fibres with stiffness in the fibre direction only. Boisse *et al.* [9] presented a refined version of the material model in 2001.

Recently, Ivanov and Tabiei [30] developed an elastic material model based on the RVE of a plain weave fabric. A homogenisation technique accounts for the weaves microstructure, with the assumption of transversely isotropic yarns. The shear properties of the fabric were neglected up to the locking angle, then the yarn shear properties were used.

Elastic material laws are fairly simple. The implementation of these models in FE packages is therefore, compared to more advanced material models, reasonably simple too. Generally, the matrix material behaviour is viscoelastic. The properties of the matrix cannot be taken into account correctly with a purely elastic material law. Only single layers of fabric were draped using these models in the literature.

Viscous Models

In 2000, Spencer [68] modelled the behaviour of impregnated woven fabrics as a viscous fluid. The fibres were assumed inextensible in his model, effectively restraining the deformation of the fluid in the fibre directions. The fluid was also assumed incompressible. In the plane stress situation, the model simplifies to a single parameter model and is able to simulate the draping behaviour of the fabric. Similarly, Spencer [69] proposed a viscoplasticity model for draping fabric reinforced composites.

The elastic behaviour of the fabric itself is not incorporated into the material models. Therefore, processing–induced fibre stresses are unaccounted for in these models. The models account for the drape behaviour of one layer of fabric only.

Multi–component Models

Multi–component models are a combination of several material models. The fibres are often represented as elastic materials in these models. Some models incorporate the fabric shear behaviour, others account for the resin behaviour in viscous material laws.

In 2001 Sidhu *et al.* [66] proposed a bi–component FE analysis for modelling dry fabric forming. The yarns were represented as trusses, using a linear elastic material law. A layer of shell elements accounted for the friction between the yarns and for the

locking of the fabric. The material behaviour in the shells was non–linearly elastic and orthotropic. The nodes of the truss and the shell elements were connected in the FE formulation. Friction between the fabric and the tooling was not incorporated in the simulation of the stamping of a spherical shape.

Cherouat and Billoët [16] presented a model for draping thermoplastic composite materials in 2001. The yarns in the fabric were represented using truss elements. The material law representing the yarns was non–linear elastic and based on three deformation mechanics; straightening, relative rotation and tensile stretching. The resin was modelled as an isotropic viscoelastic medium in a layer of shell elements. Again the nodes of the two meshes are connected in the FE simulations. Coulomb friction between the tooling and the fabric was assumed in the forming simulation of a hemispherical product.

McEntee and Ó Brádaigh [43] modelled the drape behaviour of a multi–layered thermoplastic composite on tools with a single curvature in 1998. 2D elements were stacked through–the–thickness of the sheet, each ply represented by a row of elements. The constitutive relation in each ply was based on the "ideal fibre reinforced fluid" model by Rogers [59]. A layer of contact elements was placed between the ply elements. Experiments demonstrated the presence of a resin rich layer between the individual plies during forming, justifying a viscous contact behaviour.

Also in 1998, De Luca *et al.* [23] modelled the drape behaviour of composite laminates in a dynamic explicit FE scheme. Each single fabric layer in the laminate is represented by a layer of elements. Per layer, a bi–phase material model is applied, decoupling the behaviour of the elastic fibres and the viscous matrix. The shell element layers were stacked in the thickness direction of the sheet. Between the shell elements, a "specialized viscous–friction law" was applied. The model predicts a clear interaction between the laminate lay–up and the drape–ability. Experimental results confirm the importance of this interlaminar shear effect. The method provides good results but becomes quite slow by expanding the problem computationally.

Recapitulating, draping can be modelled using the combination of continuum based material models and the FE method. If the draping surface is defined, and material properties are known, the FE method can generate a solution for the draping problem, incorporating the boundary conditions. The results of the simulation combine the information about the material deformation with the loading required for shaping. The interlaminar shear effects during forming can play a significant role in the drape–ability of multi–layered composites components. The drape behaviour of multi–layered composites can be modelled by stacking multiple element layers through–the–thickness of the sheet and connecting them by friction laws.

The FE method can give reasonably accurate results. The accuracy depends among others, on the assumptions in the material model and the solution scheme. Implicit schemes are known to give more reliable results than dynamic explicit schemes (Van den Boogaard [74]). The drape modelling should be considered as a non–linear problem due to the large deformations of the fabric during draping. This complicates the FE problem slightly.

2.1.3 Draping of multi–layered composites

Current drape predictions are based on single fabric layer models or an assembly of single fabric layer models. In some production processes the fabric layers are formed

sequentially onto the mould. Interlaminar shear between the individual fabric layers is small in such a production process. Modelling each single fabric layer sequentially suffices for such a process.

However, the interaction between the layers in the sheet is important when draping multi–layered composites. FE simulations with multiple elements through–the–thickness of the sheet are used to account for this interaction between the layers. A friction law accounts for the interlaminar shear between the individual fabric layers. The drawback of using multiple sheet elements on top of each other is the increase of the complexity of the FE model. The total number of Degrees Of Freedom (DOF's) grows linearly with the layers in the model. A non–linear system of equations is solved with an implicit FE method. The computation times to solve such a non–linear system of equations increase at least to the power of two with the increasing number of DOF's. As a result the computational time with increasing layers in the drape simulation behaves correspondingly.

Here, the aim is to find a computationally more efficient method to predict the drape behaviour of multi–layered fabric composites. A multi–layer drape material model will be developed within an implicit FE scheme to achieve this. The drape model incorporates the inter–ply and intra–ply shear behaviour of multi–layered fabric reinforced composites. The need for multiple elements through–the–thickness of the laminate is redundant by accounting for the interlaminar shear within the multi–layer model. The same type of FE element will be used for the single layer and multi–layer material model. The number of DOF's in an FE simulation with a multi–layer material model will therefore be equal to the number DOF's of the single layer model. Hence, the computation time for solving the non–linear system of equations will be comparable.

2.2 Material model for draping

Continuum mechanics defines the kinematics, stresses, strains and the conservation laws for arbitrary continuous media (Appendix A). However, continuum mechanics alone is not sufficient to describe the forming behaviour of a material. A constitutive relation is also required.

Here, based on linear elastic fibres and a Newtonian viscous resin, material models for single layer and multi–layered composites are presented. In both models an isothermal approach is used, if necessary incorporating an interaction between the warp and fill fibre families. First, a single layer intra–ply material model is presented in section 2.2.1. Based on this model, a model will be derived for multi–layered woven fabric composite materials in section 2.2.2, incorporating inter–ply shear behaviour.

2.2.1 Single layer material model

The single layer drape material constitutive equation derived here is an extension to the "Fabric Reinforced Fluid" (FRF) model by Spencer [68]. Extending the FRF model with elastic components enables the model to incorporate fibre stresses and an elastic fabric shear response in drape predictions. The composite components, the woven fabric and the resin, are subjected to an affine deformation (see figure 2.2). Thus, similarly to parallel spring–damper models, the stress $\underline{\sigma}$ can be split into two parts or:

$$\underline{\sigma} = \underline{\sigma}_e + \underline{\tau}, \tag{2.1}$$

where $\underline{\sigma}_e$ is the elastic stress contribution and $\underline{\tau}$ is an extra viscous stress contribution induced by the resin in the fabric. The elastic and viscous contributions to the stress are solved separately.

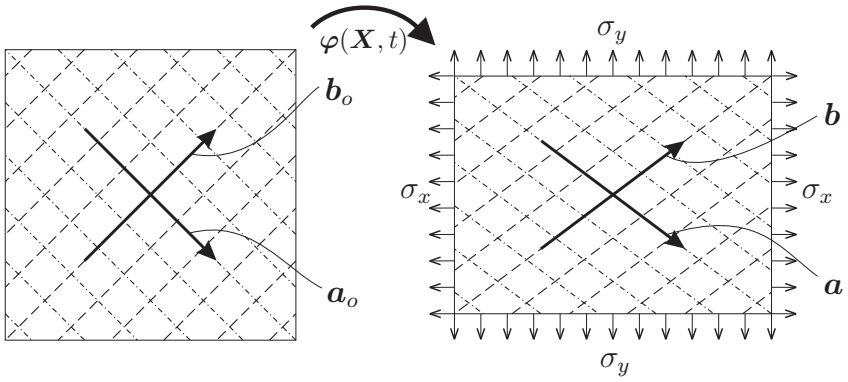

Figure 2.2: Affine deformation of fibres and matrix.

In figure 2.2, $\boldsymbol{a}$ and $\boldsymbol{b}$ are vectors, representing the warp and fill fibre families of the fabric, $\boldsymbol{\varphi}(\boldsymbol{X},t)$ maps the original configuration, with subscript o, to the current configuration in time and $\sigma_{x,y}$ are the stresses in x and y direction respectively.

Elastic stress contribution

The elastic stress $\underline{\sigma}_e$ is split as:

$$\underline{\sigma}_e = \underline{\sigma}_p + \underline{\sigma}_k + \underline{\sigma}_a + \underline{\sigma}_b + \underline{\sigma}_f, \tag{2.2}$$

where $\underline{\sigma}_p$ is stress due to hydrostatic pressure, $\underline{\sigma}_k$ is the due to compression of the material, $\underline{\sigma}_{a,b}$ are the elastic contributions of the fibre families a and b and $\underline{\sigma}_f$ is the elastic contribution of the fabric itself, caused by the interaction of the fibre families.

The hydrostatic stress is defined by:

$$\underline{\sigma}_p = -p\underline{I}, \tag{2.3}$$

where p is the hydrostatic pressure. The stress due to compression of the material is defined by:

$$\underline{\sigma}_k = K\,\mathrm{tr}(\underline{\varepsilon})\,\underline{I}, \tag{2.4}$$

where K is the bulk modulus of the matrix material, $\underline{\varepsilon}$ is the strain tensor and tr is the trace operation.

Assuming a continuous distribution of the fibres, the two fibre families of the fabric can be described with two vectors $\boldsymbol{a}(\boldsymbol{X},t)$ and $\boldsymbol{b}(\boldsymbol{X},t)$ which can vary spatially and in time, or:

$$\boldsymbol{a}(\boldsymbol{X},t) = \underline{F}(\boldsymbol{X},t)\cdot\boldsymbol{a}_o(\boldsymbol{X}), \qquad \boldsymbol{b}(\boldsymbol{X},t) = \underline{F}(\boldsymbol{X},t)\cdot\boldsymbol{b}_o(\boldsymbol{X}), \tag{2.5}$$

where $\underline{F}(\boldsymbol{X},t)$ is the deformation gradient and $\boldsymbol{a}_o(\boldsymbol{X})$, $\boldsymbol{b}_o(\boldsymbol{X})$ are the original fibre orientation unit vectors at $t=0$.

The fibres are assumed to be inextensible in Spencer's model. Here, this strict condition is relieved somewhat by assigning a finite stiffness to the fibres. In this way it

is not necessary to use Lagrange multipliers in the FE calculations. However, allowing fibre extension leads to a change in length of the characteristic vectors $\boldsymbol{a}$ and $\boldsymbol{b}$ of the fibre families. The corresponding unit vectors are introduced as:

$$\boldsymbol{a}^* = \frac{\boldsymbol{a}}{\|\boldsymbol{a}\|}, \qquad \boldsymbol{b}^* = \frac{\boldsymbol{b}}{\|\boldsymbol{b}\|}. \tag{2.6}$$

The fibres are modelled as linear elements, having no stiffness properties in any direction but the fibre longitudinal direction. The stretch of the fibre is defined as:

$$\lambda_a = \frac{\|\boldsymbol{a}\|}{\|\boldsymbol{a}_o\|} = \sqrt{\boldsymbol{a}_o \cdot \underline{F}^{\mathrm{T}} \cdot \underline{F} \cdot \boldsymbol{a}_o}. \tag{2.7}$$

The stress contribution of the fibre then becomes:

$$\underline{\sigma}_a = V_{f_a} E_a (\lambda_a - 1) \underline{A}^*, \tag{2.8}$$

where

$$\underline{A}^* = \boldsymbol{a}^* \boldsymbol{a}^*, \tag{2.9}$$

and E_a is the fibre longitudinal modulus and V_{f_a} the volume fraction of fibre family a. $\underline{A}^*$ is found from the dyadic product of the unit vector $\boldsymbol{a}^*$. An analogous relation holds for fibre family b, resulting in:

$$\underline{\sigma}_b = V_{f_b} E_b (\lambda_b - 1) \underline{B}^*, \tag{2.10}$$

where

$$\underline{B}^* = \boldsymbol{b}^* \boldsymbol{b}^*, \tag{2.11}$$

and V_{f_b} the volume fraction and E_b is the fibre longitudinal modulus of fibre family b.

The fabric elastic stress $\underline{\sigma}_f$ is caused by the interaction between the fibres, ultimately leading to the shear–locking. This phenomenon must be incorporated in the model, in order to predict wrinkling due to shear–locking. The shear response of the fabric can be determined with for instance the picture or trellis frame experiment, as shown by McGuinness and Ó Brádaigh [44] and Prodromou and Chen [57].

The shear–locking phenomenon is modelled as a non–linear elastic response, which depends on the direction of the two fibre families. The direction of the fibre families are depicted in figure 2.3.

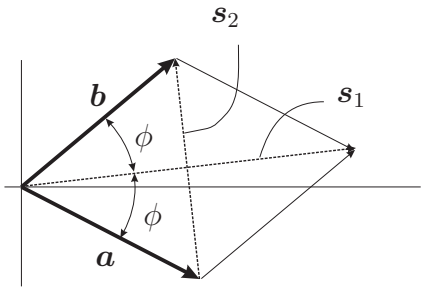

Figure 2.3: Directions of the two fibre families a and b and the bias directions of the weave.

The two bias directions of the weave, $\boldsymbol{s}_1$ and $\boldsymbol{s}_2$, are depicted in figure 2.3. The angle ϕ is the angle between the $\boldsymbol{s}_1$ direction and the fibre families a and b. Often, 2ϕ is referred to as the enclosed fibre angle. ϕ reads:

$$\phi = \tfrac{1}{2} \arccos\left(\boldsymbol{a}^* \cdot \boldsymbol{b}^*\right). \tag{2.12}$$

The material shear angle θ depends on ϕ as:

$$\theta = 2(\phi_o - \phi), \tag{2.13}$$

where the subscript o refers to the initial configuration. Generally, ϕ_o is 45° for weaves. The non–linear elastic shear–locking responses is modelled as an exponential function, depending on the material shear angle θ as:

$$\underline{\sigma}_f = V_f \, m \, (e^{n\theta} - e^{-n\theta}) \tfrac{1}{2} (\underline{C}^* + \underline{C}^{*\,\mathrm{T}}), \tag{2.14}$$

with

$$\underline{C}^* = \boldsymbol{a}^* \boldsymbol{b}^*, \tag{2.15}$$

and V_f is the overall fibre volume fraction, and m, n are constants depending on the fabric architecture, which can be evaluated from shear experiments. The overall fibre volume fraction is the sum of the fibre volume fractions of the fibre families, or:

$$V_f = V_{f_a} + V_{f_b}. \tag{2.16}$$

Viscous stress contribution

The resin is described as a purely viscous medium. The stress response of purely viscous incompressible fluids is represented by an isotropic tensor–valued function of the rate of deformation tensor (Schowalter [64]). The rate of deformation tensor $\underline{D}$ is the symmetric part of the velocity gradient tensor $\underline{L}$ (see Appendix A.1). When $\underline{D}$ meets the incompressibility condition, the most general representation for the viscous stress contribution $\underline{\tau}$ of incompressible viscous fluids can be written as a power series expansion, or:

$$\begin{aligned} \underline{\tau} &= \underline{\tau}(\underline{D}) \\ &= -p\underline{I} + \psi_1 \underline{D} + \psi_2 \underline{D}^2, \end{aligned} \tag{2.17}$$

where p is the hydrostatic pressure, $\underline{I}$ is the unit tensor and $\psi_{1,2}$ are functions of the invariants $\mathrm{tr}\,\underline{D}^2$ and $\mathrm{tr}\,\underline{D}^3$. In Spencer's FRF model [68], the viscous stress contribution depends on the rate of deformation and also on the fibre directions:

$$\underline{\tau} = \underline{\tau}(\underline{D}, \boldsymbol{a}^*, \boldsymbol{b}^*). \tag{2.18}$$

Spencer derived an expression for a linear incompressible anisotropic viscous response of the resin material with inextensible fibres. In this case, the viscous stress contribution is given in its most general form by:

$$\begin{aligned} \underline{\tau}(\underline{D}, \boldsymbol{a}^*, \boldsymbol{b}^*) = {} & 2\eta\underline{D} + 2\eta_1(\underline{A}^* \cdot \underline{D} + \underline{D} \cdot \underline{A}^*) + 2\eta_2(\underline{B}^* \cdot \underline{D} + \underline{D} \cdot \underline{B}^*) + \\ & 2\eta_3(\underline{C}^* \cdot \underline{D} + \underline{D} \cdot \underline{C}^{*\,\mathrm{T}}) + 2\eta_4(\underline{C}^{*\,\mathrm{T}} \cdot \underline{D} + \underline{D} \cdot \underline{C}^*) \end{aligned}. \tag{2.19}$$

In equation (2.19), η, η_1, η_2, η_3 and η_4 are characteristic anisotropic viscosities generally being functions of the angle between the fibre families a and b.

Spencer's relation for the viscous stress contributions is based on inextensible fibres. The fibre stresses are constitutively determined by the strain in the fibre direction in the material model derived here. As a result, $\underline{D}$ not necessary meets the inextensibility conditions in the fibre directions. A modified rate of deformation tensor $\underline{D}^*$ is introduced to overcome this discrepancy:

$$\underline{D}^* = \underline{D} + c_1\underline{A}^* + c_2\underline{B}^* + c_3\underline{I}, \tag{2.20}$$

where $\underline{D}^*$ is the deviatoric part, satisfying the inextensibility and incompressibility conditions:

$$\begin{aligned} \underline{A}^* \colon \underline{D}^* &= 0, \\ \underline{B}^* \colon \underline{D}^* &= 0, \\ \underline{I} \colon \underline{D}^* &= 0. \end{aligned} \tag{2.21}$$

With these conditions it can be found that the unknowns $c_{1,2,3}$ are:

$$\begin{aligned} c_1 = \frac{1}{d}\big[&(3g_B - \mathrm{I}_B^2)(\underline{A}^* \colon \underline{D}) - (3g_{AB} - \mathrm{I}_A\mathrm{I}_B)(\underline{B}^* \colon \underline{D}) + \\ &(g_{AB}\mathrm{I}_B - \mathrm{I}_A g_B)\mathrm{I}_D\big] \\ c_2 = \frac{1}{d}\big[&(3g_A - \mathrm{I}_A^2)(\underline{B}^* \colon \underline{D}) - (3g_{AB} - \mathrm{I}_A\mathrm{I}_B)(\underline{A}^* \colon \underline{D}) + \\ &(g_{AB}\mathrm{I}_A - g_A\mathrm{I}_B)\mathrm{I}_D\big] \\ c_3 = \frac{1}{d}\big[&(g_{AB}\mathrm{I}_B - \mathrm{I}_A g_B)(\underline{A}^* \colon \underline{D}) + (g_{AB}\mathrm{I}_A - g_A\mathrm{I}_B)(\underline{B}^* \colon \underline{D}) - \\ &(g_{AB}^2 - g_A g_B)\mathrm{I}_D\big] \end{aligned} \tag{2.22}$$

where

$$d = g_A\mathrm{I}_B^2 + 3g_{AB}^2 - 2g_{AB}\mathrm{I}_A\mathrm{I}_B + g_B\mathrm{I}_A^2 - 3g_A g_B,$$

$$\mathrm{I}_A = \underline{A}^* \colon \underline{I}, \qquad \mathrm{I}_B = \underline{B}^* \colon \underline{I}, \qquad \mathrm{I}_D = \underline{D} \colon \underline{I},$$

and

$$g_A = \underline{A}^* \colon \underline{A}^*, \qquad g_B = \underline{B}^* \colon \underline{B}^*, \qquad g_{AB} = \underline{A}^* \colon \underline{B}^*.$$

Using equation (2.20) in equation (2.19) and substituting equations (2.8), (2.10), (2.14) and (2.19) in equation (2.1), the total stress becomes:

$$\begin{aligned} \underline{\sigma} = &-p\underline{I} + V_{f_a}\, E_a(\lambda_a - 1)\underline{A}^* + V_{f_b}\, E_b(\lambda_b - 1)\underline{B}^* + \\ &\tfrac{1}{2}V_f\, m\,(e^{n\theta} - e^{-n\theta})(\underline{C}^* + \underline{C}^{*\mathrm{T}}) + \\ &V_m\big[2\eta\underline{D}^* + 2\eta_1(\underline{A}^* \cdot \underline{D}^* + \underline{D}^* \cdot \underline{A}^*) + 2\eta_2(\underline{B}^* \cdot \underline{D}^* + \underline{D}^* \cdot \underline{B}^*) + \\ &2\eta_3(\underline{C}^* \cdot \underline{D}^* + \underline{D}^* \cdot \underline{C}^{*\mathrm{T}}) + 2\eta_4(\underline{C}^{*\mathrm{T}} \cdot \underline{D}^* + \underline{D}^* \cdot \underline{C}^*)\big], \end{aligned} \tag{2.23}$$

where V_m is the volume fraction of the matrix material. Note that the sum of the volume fractions of the constituents V_m, V_{f_a} and V_{f_b} equals 1.

Plane stress conditions

Normally, the composite is applied in a plate or sheet like form. The fibres in the sheet are assumed to be in the plane of the sheet or:

$$a_3 = 0, \qquad b_3 = 0.$$

Additionally, a plane stress situation is assumed, or:

$$\sigma_{13} = 0, \qquad \sigma_{23} = 0, \qquad \sigma_{33} = 0. \tag{2.24}$$

When applying (2.24) on (2.23), the resulting plane stress situation reads:

$$\begin{aligned}
\sigma_{11} = {} & V_{f_a} E_a(\lambda_a - 1)a_1^{*2} + V_{f_b} E_b(\lambda_b - 1)b_1^{*2} + \tfrac{1}{2} V_f\, m\, (e^{n\theta} - e^{-n\theta})\, a_1^* b_1^* + \\
& 2V_m D_{11}^*(\eta + 2\eta_1 a_1^{*2} + 2\eta_2 b_1^{*2} + 2(\eta_3 + \eta_4)a_1^* b_1^*) + \\
& 4V_m D_{12}^*(\eta_1 a_1^* a_2^* + \eta_2 b_1^* b_2^* + \eta_3 a_1^* b_2^* + \eta_4 a_2^* b_1^*) - 2V_m \eta D_{33}^* \\
\sigma_{12} = {} & V_{f_a} E_a(\lambda_a - 1)a_1^* a_2^* + V_{f_b} E_b(\lambda_b - 1)b_1^* b_2^* + \tfrac{1}{4} V_f\, m\, (e^{n\theta} - e^{-n\theta})(a_1^* b_2^* + a_2^* b_1^*) + \\
& 2V_m \eta D_{11}^*(\eta_1 a_1^* a_2^* + \eta_2 b_1^* b_2^* + \eta_3 a_2^* b_1^* + \eta_4 a_1^* b_2^*) + \\
& 2V_m D_{22}^*(\eta_1 a_1^* a_2^* + \eta_2 b_1^* b_2^* + \eta_3 a_1^* b_2^* + \eta_4 a_2^* b_1^*) + \\
& 2V_m D_{12}^* \left(\tfrac{1}{2}\eta + \eta_1(a_1^{*2} + a_2^{*2}) + \eta_2(b_1^{*2} + b_2^{*2}) + \eta_3(a_1^* b_1^* + a_2^* b_2^*) + \eta_4(a_1^* b_1^* + a_2^* b_2^*)\right) \\
\sigma_{22} = {} & V_{f_a} E_a(\lambda_a - 1)a_2^{*2} + V_{f_b} E_b(\lambda_b - 1)b_2^{*2} + \tfrac{1}{2} V_f\, m\, (e^{n\theta} - e^{-n\theta})\, a_2^* b_2^* + \\
& 2V_m D_{22}^*(\eta + 2\eta_1 a_2^{*2} + 2\eta_2 b_2^{*2} + 2(\eta_3 + \eta_4)a_2^* b_2^*) + \\
& 4V_m D_{12}^*(\eta_1 a_1^* a_2^* + \eta_2 b_1^* b_2^* + \eta_3 a_2^* b_1^* + \eta_4 a_1^* b_2^*) - 2V_m \eta D_{33}^*
\end{aligned} \tag{2.25}$$

The constitutive relation is symmetric with respect to the fibre families a and b when the fibre families are mechanically equivalent. This symmetry in the constitutive relation affects some parameters in the extra viscous stress contribution [68]. $\eta_1 = \eta_2$ and $\eta_3 = \eta_4$ result from this symmetry. Three parameters η, η_1 and η_3, generally being functions of $\cos 2\phi$, are required to determine the extra viscous stress response of the fabric. They can either be even or odd functions of $\cos 2\phi$.

The material input data can be evaluated from the picture frame shear tests [68]. Performing picture frame tests at different temperatures can incorporate the effect of temperature on the composite viscosities. Temperature dependent drape behaviour can be modelled by using these temperature dependent viscosities. However, the temperature of the fabric composite changes during forming. The composite cools during draping, especially in places where the initially hot composite is in contact with the relatively cold moulds. The model does not account for these temperature changes during draping.

2.2.2 Multi–layer material model

The mechanics of a single layer drape model were described in the previous section. The individual plies in the material must slide with respect to each other and deform individually to incorporate inter–ply behaviour of multi–layered composites. Figure 2.4 illustrates the deformation of a three ply laminate due to a load on the centre ply.
The laminate deforms from its original configuration to a current configuration. The layers are stacked on each other in the original configuration, having independent fibre

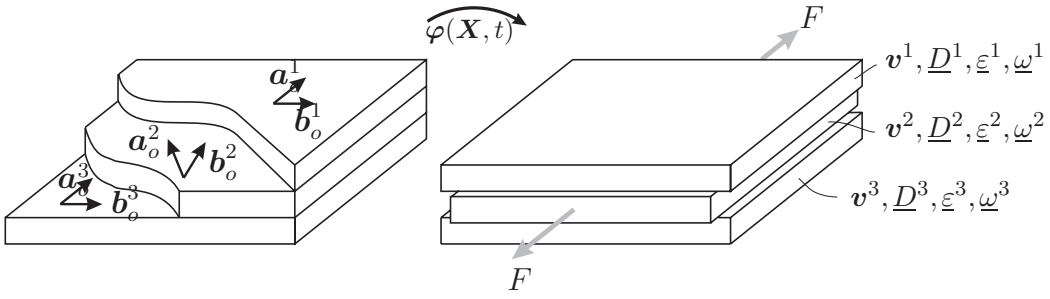

Figure 2.4: Individual deformation of layers during forming.

orientations $\boldsymbol{a}_o^i$ and $\boldsymbol{b}_o^i$, where i is the ply index. The plies are allowed to deform individually, conforming to their fibre orientations. The strains $\underline{\varepsilon}^i$, rotation $\underline{\omega}^i$, the velocities $\boldsymbol{v}^i$ and the rate of deformations $\underline{D}^i$ will generally also be non–uniform over the laminate thickness as a result.

Since the individual plies in the laminate can have different velocities, the interface between these plies must deform correspondingly. Therefore, a slip law needs to be defined which is able to describe the sliding of the individual plies.

In picture 2.5, a microscopic view of the cross–section of a glass four layered 8H satin fabric reinforced poly(phenylene sulphide) (PPS) compression moulded laminate is shown.

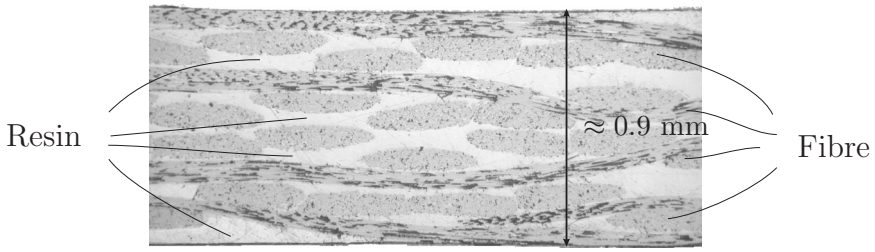

Figure 2.5: Resin rich layers between the fabric plies in an 8H satin glass fibre weave reinforced PPS.

The horizontal glass fibre yarns in dark grey indicate the separate fabric layers. Some yarn contact is noticed in figure 2.5. However, resin is observed between most of the plies. These plies are separated by the lighter coulored thin PPS layers. Based on the observations of these resin rich layers between the plies and following the work of McEntee and Ó Brádaigh [43], the interlaminar behaviour is assumed to be viscous. This leads to a viscous slip law expressed in the velocity differences between adjacent plies. The velocity difference $\boldsymbol{v}_{rel}^j$ between the plies is:

$$\boldsymbol{v}_{rel}^j = \boldsymbol{v}^{i+1} - \boldsymbol{v}^i, \tag{2.26}$$

where the suffix i indicates the ply and j indicates the interface layer. When assuming a friction law which depends linearly on the velocity difference between the plies, the interface traction $\boldsymbol{\gamma}^j$ is defined as:

$$\boldsymbol{\gamma}^j = \frac{1}{\beta_j}\boldsymbol{v}_{rel}^j, \tag{2.27}$$

where β_j is the constant friction factor per interface. As a result, the constant friction factor is:

$$\beta_j = \frac{h_j}{\eta_j}, \tag{2.28}$$

where h_j is the thickness of the interface layer and η_j the viscosity of the interface layer.

2.3 Characterising material properties

The material properties for the constitutive relations (2.25) and (2.27) must be obtained to model draping with FE. Two types of material characterisation are distinguished to determine the material parameters; measuring the intra–ply and inter–ply composite properties.

Little standardisation is done in the experimental field of pre–impregnated technical fabrics at production temperature. Some standardisation for measuring the intra–ply response of dry textiles is applied in the garment industry. The Kawabata Evaluation System for fabrics (KES-F) [33] is used to measure the formability of fashion cloths at room temperature. Unfortunately, KES-F is not applicable for testing pre–impregnated composite materials since it is not designed to test at high temperatures, apply large shear deformations or measure at high loading conditions.

The intra–ply material parameters required for the single layer material model are quite extensive. The fibre properties are available in literature [54], and therefore not experimentally determined here. The other material properties, m , n, η, η_1, η_2, η_3 and η_4, need to be quantified in experiments. Picture frame experiments are used to determine these intra–ply properties.

The inter–ply composite properties can be determined using pull–out tests [48].

2.3.1 Picture Frame tests

McGuinness and Ó Brádaigh [44] developed the picture or trellis frame experiment in order to measure the in–plane response of woven fabric reinforced composites. Since then, several authors (Prodromou and Chen [57], Mohammed *et al.* [47], Peng *et al.* [53]) applied the picture frame experiment to determine the properties of dry and pre–impregnated fabrics. An initially square frame deforms into a rhombus, imposing a shear deformation onto the fabric. The fabric is placed in the frame with the fibre directions parallel to the arms of the frame, as shown in figure 2.6. No extension is imposed on the fabric in the fibre directions as a result.
Left or right shear deformation, denoted with the subscripts l and r, are imposed on the fabric by extending the frame in vertical or horizontal direction respectively. The shear response of the composite can be determined by measuring the load response $F_{l,r}$ of the frame. The load, required to deform the fabric, is measured as a function of the crosshead displacement in a tensile testing machine. The shear response of the weave can differ for left and right shear [44]. The weave reacts unsymmetrically to shear deformation if the load response for left shear F_l differs from the load response for right shear F_r. Impregnated composites are tested above the glass transition or melt temperature of the matrix material. The entire picture frame, including the specimen, is placed in an oven in order to perform these high temperature tests.

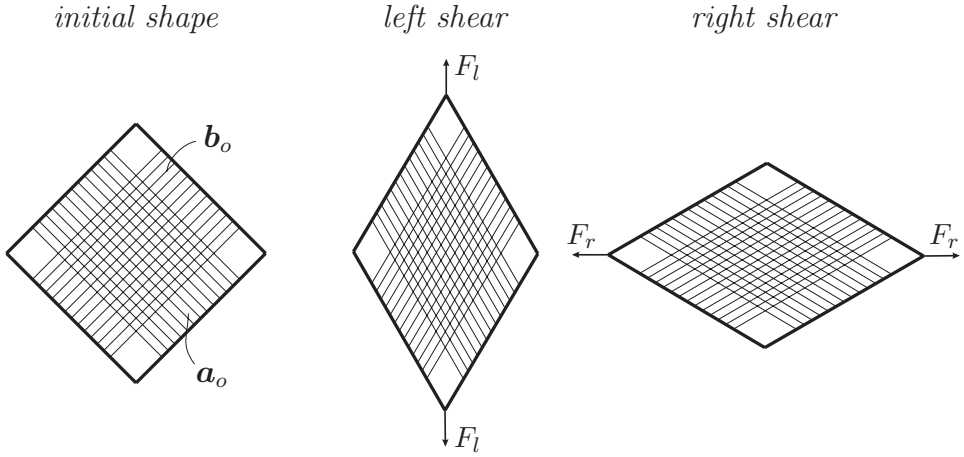

Figure 2.6: Schematic deformation of the composite in the picture frame experiment; initial configuration, imposing left shear and imposing right shear.

Picture frame kinematics

The crosshead displacement of the tensile testing machine causes the frame to shear. The velocity at which the crosshead travels is constant during the test, resulting in a variation of the shear rate of the fabric. The fabric deformation can be expressed in terms of the crosshead displacement and velocity.

A schematic view of the frame in undeformed and deformed state is shown in figure 2.7. The frame with side length l_f and initial frame angle ϕ_o is shown on the left hand side, using one line of symmetry. The deformed frame is presented on the right hand side.

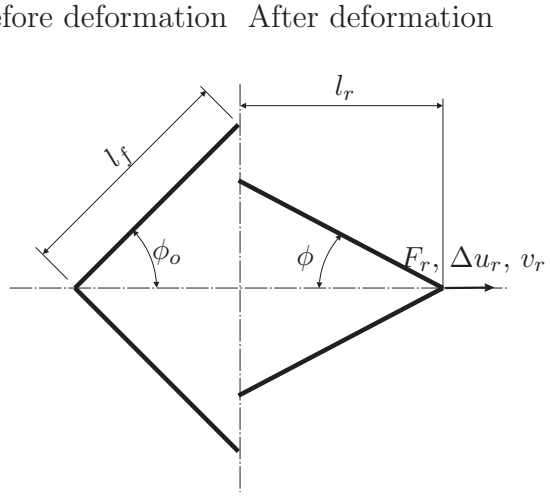

Figure 2.7: Schematic view on half of the picture frame; undeformed and deformed shape.

The displacement Δu_r and its velocity v_r for right shear are shown in figure 2.7. The length l_r of the frame in the deformed state as a function of the displacement is found

by:

$$l_r = l_f \cos\phi_o + \Delta u_r. \tag{2.29}$$

Expressed in the displacement Δu_r and the length of the sides of the picture frame l_f, the frame angle ϕ equals:

$$\phi = \arccos\left(\cos\phi_o + \frac{\Delta u_r}{l_f}\right). \tag{2.30}$$

When a left shear deformation is applied, the crosshead displacement Δu_l results in a frame angle ϕ:

$$\phi = \arcsin\left(\sin\phi_o + \frac{\Delta u_l}{l_f}\right), \tag{2.31}$$

where Δu_l is in the positive vertical direction. The material shear angle θ can be found straightforwardly by substituting equation (2.30) or (2.31) in equation (2.13).

The rate of deformation tensor $\underline{D}$ is [68]:

$$\underline{D} = \begin{bmatrix} -\tan\phi & 0 & 0 \\ 0 & \cot\phi & 0 \\ 0 & 0 & -2\cot 2\phi \end{bmatrix} \dot{\phi}, \tag{2.32}$$

where $\dot{\phi}$ is the time derivative of the frame angle. The rate of change of the frame angle for right shear deformation is found from:

$$\dot{\phi} = -\frac{v_r}{l_f \sin\phi}, \tag{2.33}$$

and the time derivative of the frame angle for left shear deformation is:

$$\dot{\phi} = \frac{v_l}{l_f \cos\phi}. \tag{2.34}$$

The fibre directions during testing are parallel to the sides of the frame. They are found from:

$$\boldsymbol{a} = (\cos\phi, -\sin\phi, 0), \quad \boldsymbol{b} = (\cos\phi, \sin\phi, 0). \tag{2.35}$$

Picture frame equilibrium

The shear fixture imposes a shear deformation on the fabric. When neglecting inertia effects, the stress and the strain distributions in the frame are homogeneous as a result. The fabric is loaded in–plane in the picture frame experiment. Additionally a plane stress situation is assumed, or $\sigma_{zz} = 0$, $\sigma_{xz} = 0$ and $\sigma_{yz} = 0$, so that only the planar stress components contribute to the load response of the fabric.

Volume changes can be assumed negligible during testing [44]. The thickness of the composite thus increases during testing. The thickness increase is inversely related to the reduction in surface area of the specimen. The thickness h during testing is related to the frame angle ϕ as:

$$h = \frac{h_o}{\sin 2\phi}, \tag{2.36}$$

where h_o is the initial thickness of the specimen.

The external loading, the measured loading by the tensile testing machine, must be in equilibrium with the internal stress during testing. Performing a static analysis [46] provides the load response of the frame due to an internal stress. Three parts were constructed using the *method of sections*. The top part shows the section using the horizontal symmetry line in the picture frame. The left hand side part shows the section using the vertical symmetry axis. The right hand side part shows the section using both lines of symmetry. All three sections must be in equilibrium. The three sections are shown in figure 2.8.

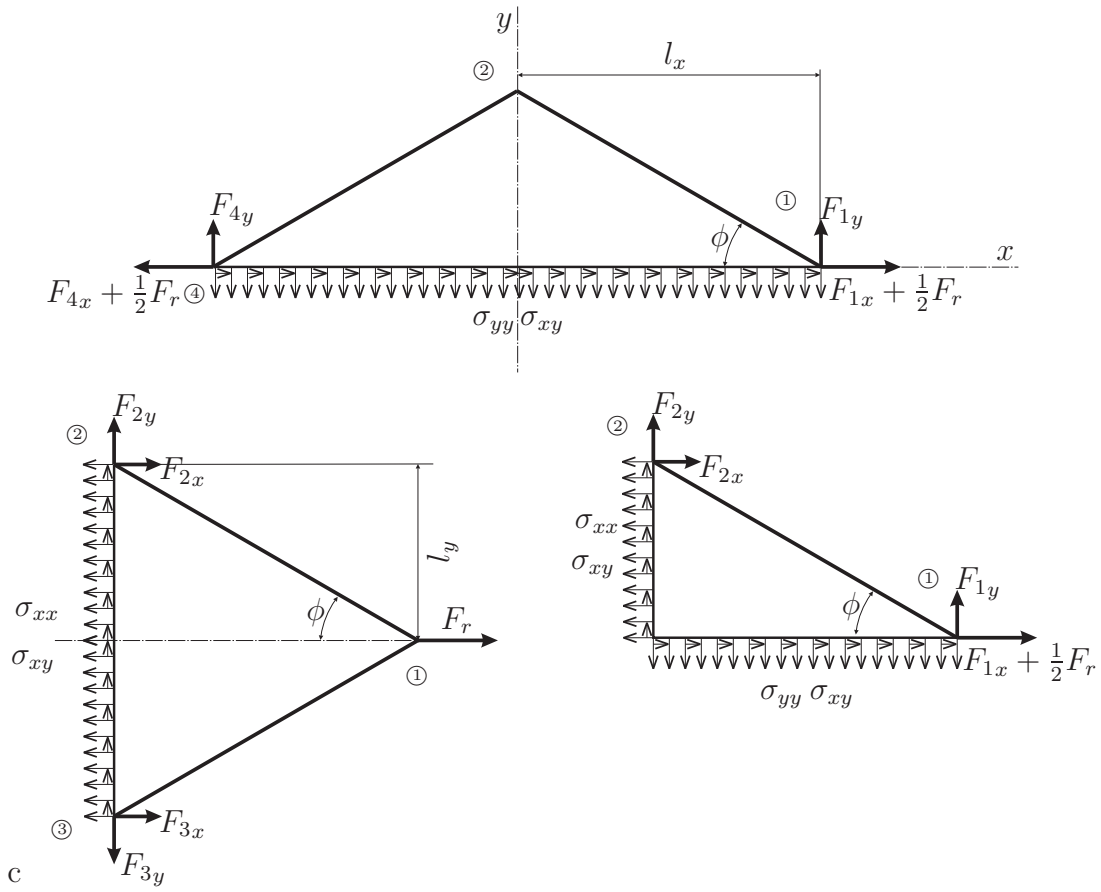

Figure 2.8: Load equilibrium in the picture frame, three sections are shown; the top part along the horizontal symmetry line, the left part along the vertical symmetry line, and a quarter of the frame using both symmetry lines. The four corners of the frame are denoted with the encircled numbers.

The Free Body Diagram (FBD) of the top section results in the following relations:

$$\sum F_x = 0 \quad \rightarrow \quad \tfrac{1}{2}F_r - \tfrac{1}{2}F_r - F_{4x} + F_{1x} + 2\sigma_{xy}hl_f \cos\phi = 0, \tag{2.37a}$$

$$\sum F_y = 0 \quad \rightarrow \quad F_{4y} + F_{1y} - 2\sigma_{yy}hl_f \cos\phi = 0, \tag{2.37b}$$

$$\sum M_1 = 0 \quad \rightarrow \quad 2F_{4y}l_f \cos\phi - 2\sigma_{yy}hl_f{}^2 \cos^{\phi} 2 = 0. \tag{2.37c}$$

The FBD of the part with the section along the vertical axis results in:

$$\sum F_x = 0 \quad \rightarrow \quad F_r + F_{2x} + F_{3x} - 2\sigma_{xx} h l_f \sin\phi = 0, \tag{2.38a}$$

$$\sum F_y = 0 \quad \rightarrow \quad F_{2y} - F_{3y} + 2\sigma_{xy} h l_f \sin\phi = 0, \tag{2.38b}$$

$$\sum M_3 = 0 \quad \rightarrow \quad F_r l_f \sin\phi - 2F_{2x} l_f \sin\phi - 2\sigma_{xx} h {l_f}^2 \sin^{\phi} 2 = 0. \tag{2.38c}$$

The FBD of a quarter of the picture frame gives:

$$\sum F_x = 0 \quad \rightarrow \quad \tfrac{1}{2}F_r + F_{1x} + F_{2x} + \sigma_{xy} h l_f \cos\phi - \sigma_{xx} h l_f \sin\phi = 0, \tag{2.39a}$$

$$\sum F_y = 0 \quad \rightarrow \quad F_{1y} + F_{2y} + \sigma_{xy} h l_f \sin\phi - \sigma_{yy} h l_f \cos\phi = 0, \tag{2.39b}$$

$$\sum M_1 = 0 \quad \rightarrow \quad \begin{array}{l} F_{2x} l_f \sin\phi + F_{2y} l_f \cos\phi - \tfrac{1}{2}\sigma_{xx} h {l_f}^2 \sin^{\phi} 2 - \\ \tfrac{1}{2}\sigma_{yy} h {l_f}^2 \cos^{\phi} 2 + \sigma_{xy} h {l_f}^2 \sin\phi\cos\phi = 0. \end{array} \tag{2.39c}$$

The response of the frame to a right shear deformation can be expressed in terms of stresses from these equations, it reads:

$$F_r = \frac{h_o}{\sin 2\phi}(\sigma_{xx} l_f \sin\phi - \sigma_{yy} l_f \cot\phi \cos\phi) \tag{2.40}$$

With a similar static analysis, the load response for left shear is found as:

$$F_l = \frac{h_o}{\sin 2\phi}(\sigma_{xx} l_f \tan\phi \sin\phi - \sigma_{yy} l_f \cos\phi) \tag{2.41}$$

The fibres are not extended in the picture frame experiment. As a result, λ_a and λ_b from equations (2.8) and (2.10) respectively, are 1, resulting in the absence of fibre stresses in the fibre families. Substituting (2.25) into (2.40) and (2.41) results in the load response of the fabric in terms of the material parameters. A non–linear fitting procedure is required to fit the material parameters m, n, η, η_1, η_2, η_3 and η_4 on the experimental data.

Picture frame experiments

Picture frame tests were performed on pre–consolidated laminates. Four layered glass fibre reinforced PPS 8H satin weave (Ten Cate Cetex© SS303) laminates were pressed. The specimens were prepared to fit into the frame. The dimensions of the specimens are shown in picture 2.9. Some fibres were removed in the zone next to the central area. Experience with the material and frame showed less wrinkling when removing fibres in this area. Five experiments were performed at 300℃ and three at 350℃ for right shear deformation. Also, two tests were performed for left shear deformation at 300°C. The velocity of the traverse of the tensile testing rig was set at 1000 mm/min for all tests. The deformed shape of the specimens is depicted in picture 2.9.
The corresponding load versus material deformation angle response of the test are given in figure 2.10. This load versus angle response is typical for the picture frame tests. The load increases with increasing deformation angle in a non–linear manner.
The load response of the specimens tested at 350℃ is significantly lower for the specimens tested at 300°C. A maximum difference of 22% was measured. The lower load is caused by the lower viscosity of the PPS matrix material at higher temperatures, resulting in

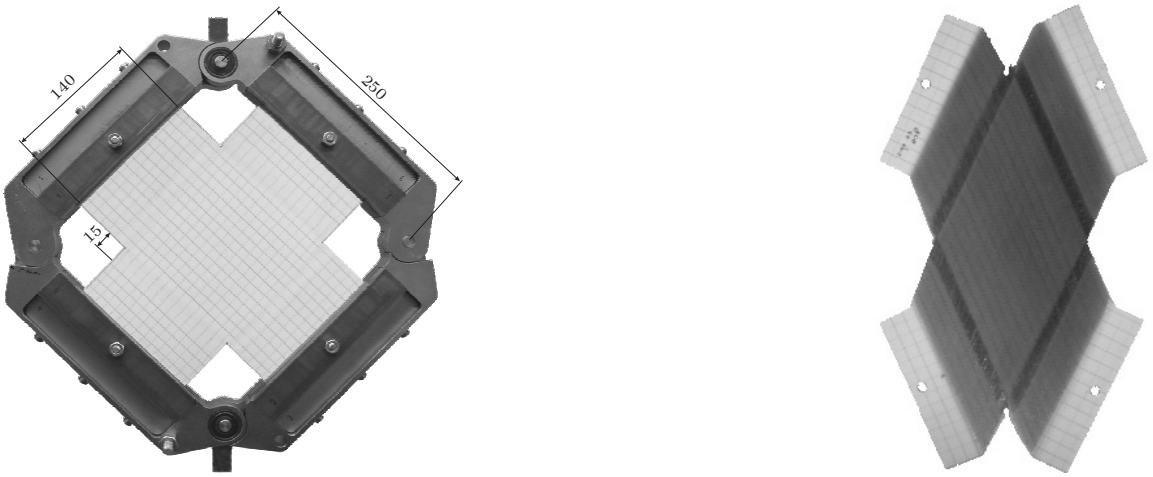

(a) *(b)*

Figure 2.9: (a): Composite clamped in the picture frame prior to testing. All dimensions are in mm.
(b): Deformed shape of the specimen after the shear test.

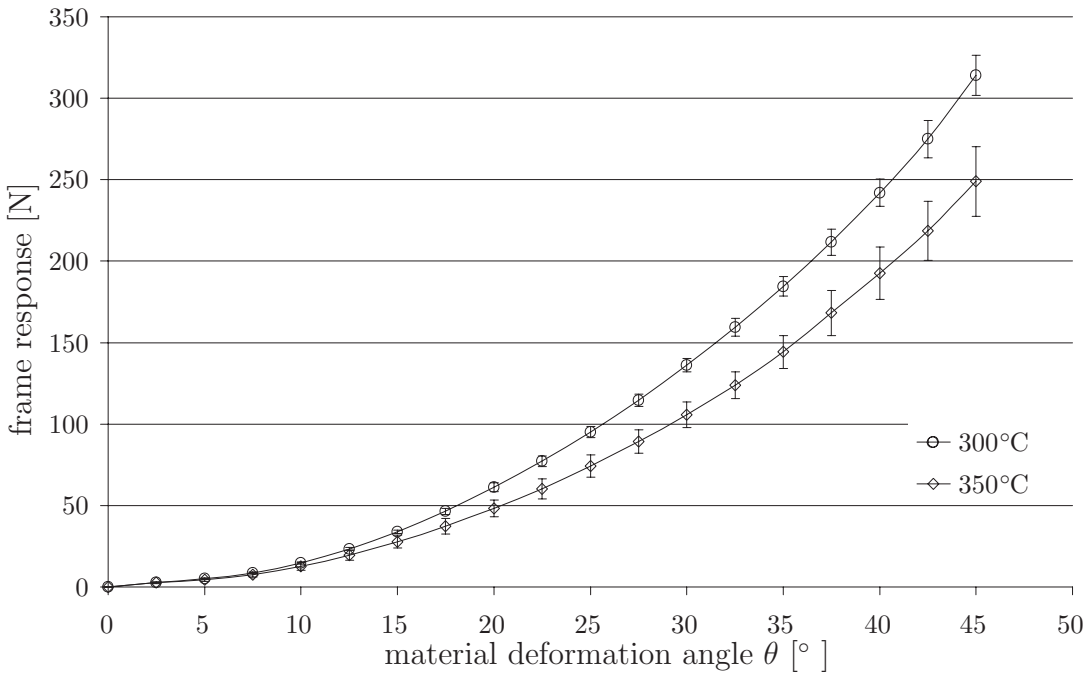

Figure 2.10: Load versus material deformation angle response during the picture frame test; test velocity 1000 mm/min*, temperature 300*°C and 350°C.

a smaller response of the viscous part of the composite. Larger differences between the results are expected when lowering the temperature below 285°C. The semi–crystalline PPS polymer start to crystallise below this temperature.

McGuinness and Ó Brádaigh [44] make clear that the load versus angle response of the impregnated fabric depends on the shearing direction. Left shear and right shear results in a different load response in their experiments. Here, left and right shear did not result in a significant change in load response, the composite intra–ply shear behaviour

is symmetrical.

A relation between composite viscosities results from in–plane symmetrical behaviour (see Spencer [68]). η_1 equals η_2 and are even functions of $\cos 2\phi$, while η_3 equals η_4 and are odd functions of $\cos 2\phi$. Fitting of the material input parameters on the experimental results gives the data listed in table 2.1.

Table 2.1: Fitted intra–ply material data

		300°C		350°C	
property		$2\phi \leq \frac{1}{2}\pi$	$2\phi > \frac{1}{2}\pi$	$2\phi \leq \frac{1}{2}\pi$	$2\phi > \frac{1}{2}\pi$
m	MPa	0.218	0.218	0.182	0.182
n	-	3.290	3.290	3.156	3.156
η	MPa s	0.281	0.281	0.205	0.205
η_1	Pa s	16.503	16.503	30.315	30.315
η_2	Pa s	16.503	16.503	30.315	30.315
η_3	MPa s	-0.394	0.394	-0.335	0.335
η_4	MPa s	-0.394	0.394	-0.335	0.335

2.3.2 Pull–out tests

The individual plies slide with respect to each other during draping. This interlaminar behaviour is accounted for in the multi–layer material model. A constant viscous traction is assumed to model this phenomenon. This traction can be measured using fabric pull out tests. Four layers of fabric are placed in a tensile testing machine in an temperature controlled environment [48]. The middle layers are the pulled out of the other two, while measuring the load as a function of the crosshead velocity.

The inter–ply slip coefficient can be determined from this experiment, but also the effect of tooling on the composite can be determined. The tools are placed on both sides of the composite and pressed with a pre–set load on the composite surface. Again these parameters are determined by measuring the load response as a functions of the crosshead velocity.

Here, a resin rich layer is assumed of 0.03 mm between the composite plies and the ply-tool interface, similarly to McEntee and Ó Brádaigh [43]. Using this thickness and assuming isotropic Newtonian viscous behaviour the constant interface parameter can be determined. The results, using the viscosity data of PPS at 300°C [42] and the viscosity at 350°C of Moldflow [41], are listed in table 2.2.

Table 2.2: Inter–ply material data

property		300°C	350°C
β	m/(MPa s)	0.3	0.462

2.4 Conclusions

An extension to the fabric reinforced fluid model was developed. It incorporates a bi–axial fabric, with elastic fibres and an elastic shear response, in a Newtonian viscous like matrix material. Additionally, a multi–layer extension was developed, incorporating a constant slip law between the individual layers.

The intra–ply material parameters were successfully fitted using the picture frame experiment. These material properties are temperature dependent.

2.5 Recommendations

Several recommendations for the drape material model are suggested.

The bi–axial fabric behaviour is shown to be of major importance by [9]. It is recommended to extend the current model in order to incorporate this phenomenon. However, Spencer's conditions of inextensibility in the fibre directions should not be harmed or an extension to Spencer's model must also be made.

The interface behaviour between the plies in the multi–layer material model is assumed viscous. Probably the behaviour is not purely viscous since yarn contact is also observed in figure 2.5. Interlaminar shear experiments should be performed in order to validate the interlaminar slip model.

Chapter 3

Finite Element drape modelling

Current drape predictions are based on single layer fabric models or an assembly of single layer fabric models. In some production processes the fabric layers are formed sequentially onto the mould. Consequently, interlaminar shear between the individual fabric layers is small, allowing the sequential modelling of each single fabric layer.

However, the interaction between the layers in the sheet is important when draping multi–layered composites. Finite Element (FE) simulations with multiple elements through–the–thickness of the sheet can take this interaction between the layers into account. The drawback of using stacked multiple sheet elements is the increase of the complexity of the FE model. As a result, the computational time with increasing layers in the drape simulation will grow significantly.

The aim here is to find a computationally more efficient drape model, which incorporates the inter–ply and intra–ply shear behaviour of multi–layered fabric reinforced composites. The need for multiple elements through–the–thickness of the laminate becomes redundant by accounting for the interlaminar shear within the multi–layer material model. Then, the same element can be used to model draping with a single layer material model and a multi–layer material model. The number of Degrees Of Freedom (DOF's) in an implicit FE simulation with a multi–layer material model will therefore be equal to the number DOF's of a single layer model. Hence, the computation time for solving the non–linear system of equations will be comparable.

Constitutive models for the drape behaviour of fabric reinforced composite materials were derived in chapter 2. Here, the models are implemented into an implicit FE code. The FE method is briefly introduced in the first section, followed by the implementation of the single layer material model and finally the multi–layer material model implementation is focussed on.

3.1 Updated Lagrangian implicit Finite Element method

A domain is discretised into a finite number of small sub–domains in FE method in order to simulate the forming process. This collection of domains is called a mesh. Evaluating the weak form of equilibrium (see A.4) at the nodes in the mesh in discrete time increments approximates the solution of the whole domain. Normally, the solution for the weak form of equilibrium is non–linear. A solution for the forming simulation is found by incrementally solving all timesteps. This section is to a large extent based on

the work of Belytschko *et al.* [6], Meinders [45], Stoker [70] and Van den Boogaard [74].

3.1.1 Updated Lagrangian method

A framework is required to evaluate the field and state variables at the discrete timesteps in the simulation. The field and state variables are expressed in the frame of the Updated Lagrangian method.

The Updated Lagrangian method is neither a Lagrangian nor an Eulerian description of motion (see appendix A). It is basically a referential framework. The field and state variables are described in the reference coordinate $\boldsymbol{X}_{ref}$ at the beginning of a timestep. The current field and state variables are evaluated using the material description and the timestep Δt. Then, the current field and state variables are mapped onto the spatial coordinate $\boldsymbol{x}_{ref}$ in the reference configuration. This mapping needs to be a one–to–one mapping. Mapping is applied at each timestep, effectively updating the field and state variables.

In standard Updated Lagrangian way, the initial field and state variables at time (i) are updated as:

$$\boldsymbol{x}^{(i+1)} = \boldsymbol{x}^{(i)} + \Delta\boldsymbol{u} \approx \boldsymbol{x}^{(i)} + \boldsymbol{v}\Delta t \tag{3.1a}$$

$$\underline{\varepsilon}^{(i+1)} = \underline{\varepsilon}^{(i)} + \Delta\underline{\varepsilon} \approx \underline{\varepsilon}^{(i)} + \dot{\underline{\varepsilon}}\Delta t \tag{3.1b}$$

$$\underline{\sigma}^{(i+1)} = \underline{\sigma}^{(i)} + \Delta\underline{\sigma} \approx \underline{\sigma}^{(i)} + \dot{\underline{\sigma}}\Delta t \tag{3.1c}$$

resulting in the current field and state variables at time $(i+1)$. Here, $\boldsymbol{x}$ is the position vector of the nodes, $\Delta\boldsymbol{u}$ is the nodal displacement increment vector and $\Delta\underline{\varepsilon}$ is the strain increment. The $\cdot$ represents the time derivative of the state variable. The strain increment is related to the nodal displacement increment vector as:

$$\Delta\underline{\varepsilon} = \tfrac{1}{2}(\Delta\boldsymbol{u}\overleftarrow{\nabla}_g + \vec{\nabla}_g\Delta\boldsymbol{u}) \tag{3.2}$$

where $\overleftarrow{\nabla}$ and $\vec{\nabla}$ represent the post– and pre–gradient operator. The suffix g denotes the geometry of the element at which the strain is evaluated. Here, the so called midpoint rule is used, *i.e.* the strain is evaluated halfway the old and the new configuration. The stress $\underline{\sigma}$ is defined by constitutive model (see section 2.2) and the strain state and is updated with the stress increment $\Delta\underline{\sigma}$.

3.1.2 Implicit Finite Element method

Equilibrium between the internal forces $\boldsymbol{F}_{int}$ and the external forces $\boldsymbol{F}_{ext}$ must be fulfilled in the implicit FE method. Integrating the iteratively updated stresses over the element areas results in the internal forces of the FE mesh. The behaviour of the FE system is non–linear, since the stress–strain relation is non–linear and geometric non–linear deformations occur during forming. Hence, the system is solved by an iterative Newton–Raphson procedure.

The objective of the Newton–Raphson procedure is to obtain a solution vector at the end of the timestep at which the internal and external forces are in equilibrium. Two stages are distinguished in the iterative Newton–Raphson procedure in order to find equilibrium. These two stages are often referred to as predictor and corrector stage.

The internal forces, determined after the update of the internal stresses, are obtained in the corrector stage for every iteration. However, a solution vector is required to

determine these internal stresses. Hence, the procedure requires a linearisation in the current iteration to estimate this solution vector. The linearisation stage is referred to as predictor stage. The estimated solution vector is subsequently used in the corrector stage to calculate the internal forces. The error between the internal and the externally applied forces is used as an accuracy measure. The solution vector is acceptable if the error meets the user defined accuracy. The predictor–corrector scheme is repeated if the error is too large, reducing the error in the solution.

3.2 Single layer material model implementation

Linear triangular membrane elements with one integration point were used to implement the intra–ply material model. The incremental strains $\Delta\underline{\varepsilon}$ are obtained from the nodal displacements using equation (3.2). The rate of deformation is assumed to be piecewise constant per time step, or:

$$\underline{D} = \frac{1}{\Delta t}\Delta\underline{\varepsilon}. \tag{3.3}$$

3.2.1 Fibre direction update

The fibre directions are represented in the triangular coordinates ξ_1 and ξ_2 of the element. It proved a convenient way to describe the fibre distortions in the updated Lagrange discretisation. In the $\boldsymbol{\xi}$ coordinates, the fibre directions $\boldsymbol{a}$ and $\boldsymbol{b}$ remain constant, so in global coordinates these automatically conform to the elements distortions, as shown in figure 3.1. The triangular coordinates are defined in the $x'y'z'$–coordinates in the plane of the element. Normalising $\boldsymbol{a}$ and $\boldsymbol{b}$ results in $\boldsymbol{a}^*$ and $\boldsymbol{b}^*$. A numerical example of the fibre direction update is presented in appendix B.1.

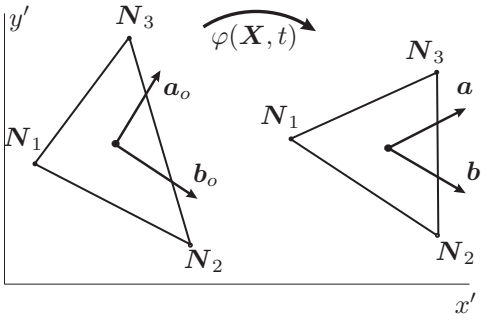

Figure 3.1: Fibre directions in natural coordinates of a deforming element.

3.2.2 Stress update

The stress requires updating in the implicit Updated Lagrangian formulation. The stress in the plane stress situation, see equation (2.25),is given as a function of the stretch, the material shear angle and the rate–of–deformation. Only the elastic components of the stress require updating.

Here, the total strain ε_a in the direction of fibre family a is defined as:

$$\varepsilon_a = (\lambda_a - 1). \tag{3.4}$$

The stress $\underline{\sigma}_a$ of the fibre family a is calculated using equation (2.8). The stress increment $\Delta\underline{\sigma}_a$ is obtained from:

$$\Delta\underline{\sigma}_a = V_{f_a} E_a \Delta\varepsilon_a \boldsymbol{a}^* \boldsymbol{a}^*. \tag{3.5}$$

An analogous relation holds for the stress increment in the direction of the fibre family b. The total stress in the fibre directions is then updated with this stress increment.

The fabric shear response $\underline{\sigma}_f$ from equation (2.14) is obtained directly from the enclosed fibre angle of the weave and the directions of the fibre families. It is therefore not an incremental stress and does not require updating.

The incremental viscous response $\underline{\tau}$ is obtained by substituting the rate of deformation tensor from equation (3.3), resulting in an formulation using the strain and time increment.

As a results, the total stress in the updated formulation reads:

$$\begin{aligned}
\sigma_{11} = {} & V_{f_a}(\sigma_a + E_a\Delta\varepsilon_a a_1^{*2}) + V_{f_b}(\sigma_b + E_b\Delta\varepsilon_b b_1^{*2}) + \tfrac{1}{2}V_f\, m\,(e^{n\theta} - e^{-n\theta})\, a_1^* b_1^* + \\
& 2V_m \frac{\Delta\varepsilon_{11}^*}{\Delta t}(\eta + 2\eta_1 a_1^{*2} + 2\eta_2 b_1^{*2} + 2(\eta_3 + \eta_4) a_1^* b_1^*) + \\
& 4V_m \frac{\Delta\varepsilon_{12}^*}{\Delta t}(\eta_1 a_1^* a_2^* + \eta_2 b_1^* b_2^* + \eta_3 a_1^* b_2^* + \eta_4 a_2^* b_1^*) - 2V_m\eta\frac{\Delta\varepsilon_{33}^*}{\Delta t} \\
\sigma_{12} = {} & V_{f_a}(\sigma_a + E_a\Delta\varepsilon_a a_1^* a_2^*) + V_{f_b}(\sigma_b + E_b\Delta\varepsilon_b b_1^* b_2^*) + \tfrac{1}{4}V_f\, m\,(e^{n\theta} - e^{-n\theta})(a_1^* b_2^* + a_2^* b_1^*) + \\
& 2V_m\eta \frac{\Delta\varepsilon_{11}^*}{\Delta t}(\eta_1 a_1^* a_2^* + \eta_2 b_1^* b_2^* + \eta_3 a_2^* b_1^* + \eta_4 a_1^* b_2^*) + \\
& 2V_m \frac{\Delta\varepsilon_{22}^*}{\Delta t}(\eta_1 a_1^* a_2^* + \eta_2 b_1^* b_2^* + \eta_3 a_1^* b_2^* + \eta_4 a_2^* b_1^*) + \\
& 2V_m \frac{\Delta\varepsilon_{12}^*}{\Delta t}\left(\tfrac{1}{2}\eta + \eta_1(a_1^{*2} + a_2^{*2}) + \eta_2(b_1^{*2} + b_2^{*2}) + \eta_3(a_1^* b_1^* + a_2^* b_2^*) + \eta_4(a_1^* b_1^* + a_2^* b_2^*)\right) \\
\sigma_{22} = {} & V_{f_a}(\sigma_a + E_a\Delta\varepsilon_a a_2^{*2}) + V_{f_b}(\sigma_b + E_b\Delta\varepsilon_b b_2^{*2}) + \tfrac{1}{2}V_f\, m\,(e^{n\theta} - e^{-n\theta})\, a_2^* b_2^* + \\
& 2V_m \frac{\Delta\varepsilon_{22}^*}{\Delta t}(\eta + 2\eta_1 a_2^{*2} + 2\eta_2 b_2^{*2} + 2(\eta_3 + \eta_4) a_2^* b_2^*) + \\
& 4V_m \frac{\Delta\varepsilon_{12}^*}{\Delta t}(\eta_1 a_1^* a_2^* + \eta_2 b_1^* b_2^* + \eta_3 a_2^* b_1^* + \eta_4 a_1^* b_2^*) - 2V_m\eta\frac{\Delta\varepsilon_{33}^*}{\Delta t}
\end{aligned} \tag{3.6}$$

3.2.3 Material tensor

A consistent Newton–Raphson scheme results in second order convergence of the error in the solution vector. Meinders [45] derived a consistent linearisation of the corrector stage in his work. Basically, the linearisation consists of two parts: a geometric and a material part. The geometric part of the linearisation is accounted for in [45]. Here, the material part of the linearisation will be focussed on. It involves the determination of the material tensor. The material tensor $\underline{\underline{M}}$ is the linearisation of the stress–strain curve, or:

$$\underline{\underline{M}} = \frac{\partial\underline{\sigma}}{\partial\underline{\varepsilon}}. \tag{3.7}$$

$\underline{\underline{M}}$ for the single layer material model reads:

$$\underline{\underline{M}} = \underline{\underline{M}}_a + \underline{\underline{M}}_b + \underline{\underline{M}}_f + \underline{\underline{M}}_v, \tag{3.8}$$

where $\underline{\underline{M}}_{a,b}$ are the contributions of the fibre families a and b respectively, $\underline{\underline{M}}_f$ the contribution of the shear–locking and $\underline{\underline{M}}_v$ the contribution of the extra viscous stress.

The contribution of the fibres is modelled linearly elastic so the modulus of the fibres and their direction determines the contribution to the material matrix. The contribution of fibre family a reads:

$$\underline{\underline{M}}_a = V_{f_a}\, \underline{T}_a{}^{\mathrm{T}} \cdot \underline{\underline{M}}_a^* \cdot \underline{T}_a, \tag{3.9}$$

where $\underline{T}_a$ describes the in–plane rotation in the direction of fibre family a and $\underline{\underline{M}}_a^*$ contains only one nonzero element, the modulus of fibre family a. Following the same method, the material stiffness contribution of fibre family b reads:

$$\underline{\underline{M}}_b = V_{f_b}\, \underline{T}_b{}^{\mathrm{T}} \cdot \underline{\underline{M}}_b^* \cdot \underline{T}_b, \tag{3.10}$$

Similarly, the fabric material tensor $\underline{\underline{M}}_f$ is determined by the fibre orientation and the non–linear elastic response. The resin contribution to the material tensor $\underline{\underline{M}}_v$ is determined by the viscosities, $\underline{D}$ and the fibre directions. A detailed description of the material tensor contributions is given in appendix B.2.

3.3 Multi–layer material model implementation

The multi–layer material model is implemented in the same linear triangular membrane elements as the single layer material model. However, the multi–layer material model involves an energy minimisation approach of the composite laminate for each element in the implicit updated Lagrangian FE scheme. Power contributions are formulated for each of the fabric layers and the interface layers within the laminate. A minimisation technique is used to find the individual incremental ply deformations, based on the average incremental deformation of an element. These ply deformations result in fibre reorientation per ply. The incremental stress per ply is determined from the individual ply deformation, accounting for the fibre reorientation. The incremental stress response of the element is determined by weighted averaging of the individual ply stresses. Updating of the initial stress with the stress increment results in the total stress at the end of the timestep.

The deformations of the individual layers are not equal to the average element deformations after the implicit updated Lagrangian step, resulting in material flow over the element boundaries. A forward Euler scheme is implemented to account for this flow.

The steps, involved in the implementation of the multi–layer material model, are treated in the next sections. First, the individual ply deformations, following from the energy minimisation approach, are described. Then, the update of the fibre stresses and the linearisation of the material are elaborated. Finally, the convective step is explained.

3.3.1 Ply deformations

The plies in the multi–layer model each have independent fibre orientations $\boldsymbol{a}^i$ and $\boldsymbol{b}^i$, where i is the ply index. The plies are allowed to deform individually for a given average incremental element deformation. As a result, the velocity, strain, rotation and the rate of deformation will generally also be non–uniform over the laminate thickness.

Solving of the individual ply deformations is explained in a few steps. First, the ply kinematics, required to find the individual ply deformations are defined. Then, power

contributions are derived for the plies and the interface between the plies. Finally, the individual ply deformations are solved by minimising the power in the element.

Ply kinematics and deformation

A bi–linear displacement field in the plane of the element is defined for each laminate ply under the assumption of plane stress as:

$$\begin{aligned} u_x^i &= c_1^i + c_2^i x + c_3^i y \\ u_y^i &= d_1^i + d_2^i x + d_3^i y \end{aligned}, \tag{3.11}$$

where u_x^i and u_y^i describe the displacement fields in x– and y–direction respectively, with respect to the initial element configuration at the start of the time increment. $c_{1,2,3}^i$ and $d_{1,2,3}^i$ are constants, determining the displacement fields of the plies and the suffix i is the layer index.

The linearised incremental strain per ply is defined as:

$$\Delta\underline{\varepsilon}^i = \tfrac{1}{2}(\boldsymbol{u}^i \overleftarrow{\nabla} + \vec{\nabla}\boldsymbol{u}^i), \tag{3.12}$$

and the incremental rotation as:

$$\Delta\underline{\omega}^i = \tfrac{1}{2}(\boldsymbol{u}^i \overleftarrow{\nabla} - \vec{\nabla}\boldsymbol{u}^i). \tag{3.13}$$

Differentiating with respect to time leads to:

$$\begin{aligned} v_x^i &= \frac{\partial}{\partial t}\left(c_1^i + c_2^i x + c_3^i y\right) \\ v_y^i &= \frac{\partial}{\partial t}\left(d_1^i + d_2^i x + d_3^i y\right) \end{aligned}, \tag{3.14}$$

where v_x^i and v_y^i are the velocities in x– and y–direction respectively. By definition, the rate of deformation tensor $\underline{D}^i$ is (see appendix A):

$$\underline{D}^i = \tfrac{1}{2}(\boldsymbol{v}^i \overleftarrow{\nabla} + \vec{\nabla}\boldsymbol{v}^i). \tag{3.15}$$

Note that the incremental strain $\Delta\underline{\varepsilon}^i$, incremental rotation $\Delta\underline{\omega}^i$ and rate of deformation $\underline{D}^i$ are piecewise constant for each ply during a timestep.

Power contributions

Several components in the multi–layer drape material model add to the power in the composite. These are the power contribution by the individual plies, the power contribution by the interface and stresses acting on the sides of the individual plies.

Power contribution by the plies

The stress $\underline{\sigma}^i$ per ply is obtained by substituting equations (3.12) and (3.15) and the ply fibre directions into equation (2.25). With this stress, the power contribution P_{ly}^i per ply is derived as:

$$P_{ly}^i = \int_{\Omega^i} \underline{D}^i : \underline{\sigma}^i d\Omega^i, \tag{3.16}$$

where Ω^i is the volume of ply i.

Power contribution by the interfaces

Since the individual plies in the laminate can have different velocities, the interfaces between these plies must deform correspondingly. The slip law, defined in equation (2.27), accounts for the sliding of the individual plies. Using the velocity difference $\boldsymbol{v}_{rel}^{j}$ from equation (2.26) and a constant slip traction $\boldsymbol{\gamma}^{j}$, the slip power P_{int}^{j} can be elaborated to:

$$P_{int}^{j} = \int_{\Phi^j} \boldsymbol{\gamma}^{j} \cdot \boldsymbol{v}_{rel}^{j} \, d\Phi^{j} = \int_{\Phi^j} \frac{1}{\beta_j} \boldsymbol{v}_{rel}^{j} \cdot \boldsymbol{v}_{rel}^{j} \, d\Phi^{j}, \tag{3.17}$$

with Φ^j the surface area and β_j the constant friction factor of interface layer j.

Power contribution by the stresses acting on the sides

The power contributions from ply deformation and slip between plies are contributions from within one element. Adjacent elements can also influence the deformations of the plies within the element. Mesh deformations vary locally in the forming simulation. Hence, the stress in the adjacent elements will not be equal. As a result, the stress in the ply of the adjacent element will also differ from the stress in the current element since the plies in the composite are allowed to deform individually. These ply stresses act on the sides of the plies.

A side traction is defined to account for the fibre stresses in the adjacent elements. The side traction $\boldsymbol{t}^{i,k}$ on side k of the i–th ply reads:

$$\boldsymbol{t}^{i,k} = (\underline{\sigma}_a^{i,k} + \underline{\sigma}_b^{i,k}) \cdot \boldsymbol{n}^{k}, \tag{3.18}$$

where $\boldsymbol{n}^{k}$ the normal on side k of the element. A representation of these side tractions in the local $x'y'z'$–coordinates is shown in figure 3.2.

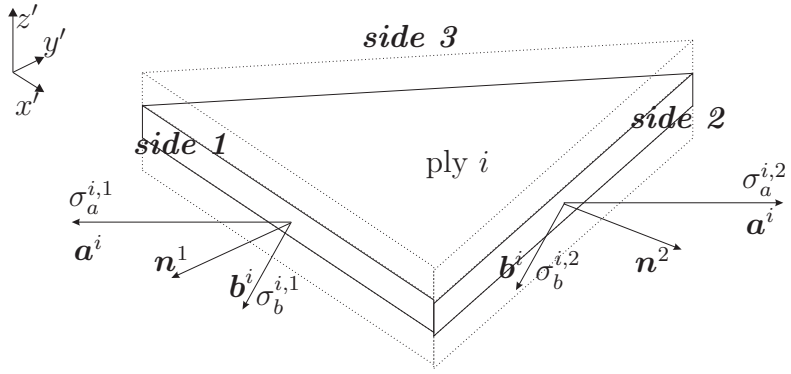

Figure 3.2: Fibre stresses action on the sides of ply i in the plane of the element.

The resulting power contribution $P_{tr}^{i,k}$ per side k of the each ply i reads:

$$P_{tr}^{i,k} = \int_{\Gamma^k} \boldsymbol{t}^{i,k} \cdot \boldsymbol{v}_{s}^{i,k} d\Gamma^{k}, \tag{3.19}$$

where $\boldsymbol{v}_{s}^{i,k}$ are the velocities at the edges of the plies i at side k. The stress contributions by the fibre families are only evaluated in the FE implementation, the other components such as shear–locking and viscosity contributions are neglected.

Solving the ply deformations

The individual ply deformations are obtained by minimising the total power within the element. The power contribution of the individual plies, interfaces and stresses acting on the side edges of the plies are added to the relation of power as:

$$P = \sum_{i=1}^{n} P_{ly}^{i} + \sum_{j=1}^{n-1} P_{int}^{j} + \sum_{i=1}^{n} \sum_{k=1}^{s} P_{tr}^{i,k}, \tag{3.20}$$

where P represents the power in the laminate, n indicates the number of plies and s the number of sides of the element.

The deformation and velocity per ply is found by minimising the total power. Minimising P for $c_{1,2,3}^{i}$ and $d_{1,2,3}^{i}$ results in:

$$\frac{\partial P}{\partial \boldsymbol{q}} = 0, \quad \text{where } \boldsymbol{q} = c_l^i, d_l^i \quad \text{with } l = 1, 2, 3. \tag{3.21}$$

With equation (3.21) and the constraints:

$$\Delta\underline{\overline{\varepsilon}} = \frac{1}{h}\sum_{i=1}^{n} h^i \Delta\underline{\varepsilon}^i, \quad \Delta\underline{\overline{\omega}} = \frac{1}{h}\sum_{i=1}^{n} h^i \Delta\underline{\omega}^i, \quad \underline{\overline{D}} = \frac{1}{h}\sum_{i=1}^{n} h^i \underline{D}^i, \quad \overline{\boldsymbol{v}}_{ip} = \frac{1}{h}\sum_{i=1}^{n} h^i \boldsymbol{v}_{ip}^i, \tag{3.22}$$

a linear system with the unknowns $c_{1,2,3}^{i}$ and $d_{1,2,3}^{i}$ is formed. The incremental strain, rate of deformation, incremental rotation and velocity at the integration point are denoted as $\Delta\underline{\overline{\varepsilon}}$, $\underline{\overline{D}}$, $\Delta\underline{\overline{\omega}}$ and $\overline{\boldsymbol{v}}_{ip}$ respectively. These averaged values are derived from the nodal displacement increments in the FE representation, the element configuration and the timestep. This system can be solved straightforwardly, eventually resulting in the individual ply deformations.

3.3.2 Fibre direction update

The fibre directions per ply are expressed in the element coordinates in the multi–layer material model at the beginning of the timestep, similarly to the single layer material model (section 3.2). The energy minimisation approach results in individual ply deformations and the fibre reorientation conform these deformations. These fibre directions need to be updated.

The individual ply deformations are expressed in terms of the constants $c_{1,2,3}^{i}$ and $d_{1,2,3}^{i}$. Internal nodes per ply are constructed by substituting these solved constants into equation (3.11). These internal nodes through–the–thickness are constructed at the centre of the individual plies in the multi–layer material model. A two–dimensional example is shown in figure 3.3.

The laminate plies deform from the initial into the current configuration in figure 3.3. The external nodes, the nodes of the FE mesh, are shown in black and named N_1 and N_2. These external nodes define the shape of the deformed element. The internal nodes are shown in grey and are called I_j^i, where the subscript j indicates the node number and the superscript i indicates the ply. The fibre reorientation from the initial into the current state conform to the internal nodal coordinates for each ply, similarly to the fibre direction update in the single layer material model from section 3.2.1.

A projection scheme is used to obtain the fibre directions per ply in the average element configuration at the end of the timestep. A schematic representation of the

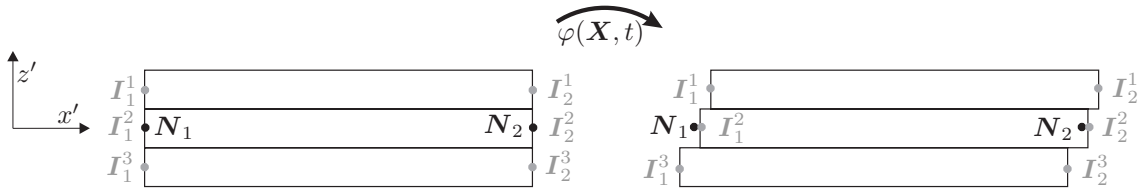

Figure 3.3: Through–the–thickness view at the internal nodes of the multi–layer material model.

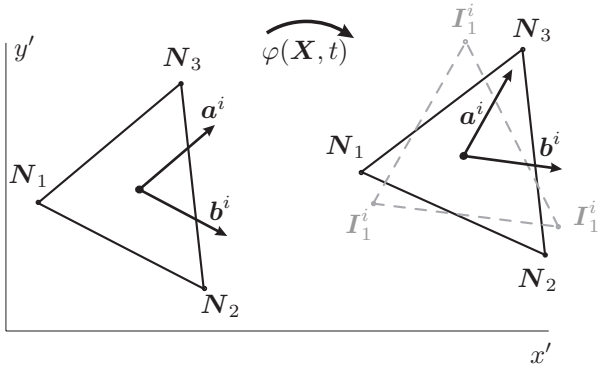

Figure 3.4: Fibre reorientation in ply i after the energy minimisation approach. The fibre directions are projected onto the average element configuration.

updating process is depicted in figure 3.4.
The element deforms from the initial configuration at time t into the current configuration at time $(t + \Delta t)$ in figure 3.4. Only the average element configuration and one ply is shown in this figure. The grey dotted triangle represents the deformation of ply i while the average element is presented with a black line. The fibre directions $\boldsymbol{a}$ and $\boldsymbol{b}$ are projected from the individual ply configuration onto the average element configuration. Normalising the vectors $\boldsymbol{a}^i$ and $\boldsymbol{b}^i$ leads to the vectors $\boldsymbol{a}^{*,i}$ and $\boldsymbol{b}^{*,i}$.

3.3.3 Stress update

The stress update in the multi–layer material model is slightly more complex than the single layer material model stress update. The individual ply deformations are solved by the energy minimisation approach from section 3.3.1. The fibre reorientation per ply, resulting from these ply deformations are determined in section 3.3.2. The stress increment $\Delta\underline{\sigma}^i$ per ply, corresponding to the ply deformation, is determined by substituting $\Delta\underline{\varepsilon}^i$, $\underline{D}^i$, $\boldsymbol{a}^{*,i}$ and $\boldsymbol{b}^{*,i}$ into equation (2.25).

The incremental average stress $\Delta\overline{\underline{\sigma}}$ is determined by weighted averaging of the ply stresses over the height of the laminate, it reads:

$$\Delta\overline{\underline{\sigma}} = \frac{1}{h}\sum_{i=1}^{n} h^i\,\Delta\underline{\sigma}^i, \tag{3.23}$$

where h is the thickness and the superscript i indicates the ply. The total stress response at the end of the timestep is found by substituting $\Delta\overline{\underline{\sigma}}$ into equation 3.1.

3.3.4 Material tensor

The fibre directions $\boldsymbol{a}^{*,i}$ and $\boldsymbol{b}^{*,i}$ are used in the rotation tensors per ply to determine the material tensor contributions per ply $\underline{\underline{M}}^i$. The material tensor is constructed by weighted averaging of the individual plies, similarly to the stress update. An iso–strain approach is used, assuming that all plies undergo the same deformation. The material tensor reads:

$$\overline{\underline{\underline{M}}} = \frac{1}{h} \sum_{i=1}^{n} h^i \, \underline{\underline{M}}^i, \tag{3.24}$$

where $\overline{\underline{\underline{M}}}$ is the averaged material tensor, h is the thickness and the superscript i indicates the ply.

The material tensor overestimates the material stiffness properties somewhat, since an iso–strain assumption was made. The interface layer will allow the plies to deform individually, leading to an lower stress response in the corrector than estimated by the predictor. The predictor–corrector scheme is therefore not fully consistent, resulting in lower than second order convergence.

3.3.5 Convection of the state variables

The implicit Lagrangian step results in ply flow outside the average configuration of the element, as depicted in figures 2.4, 3.3 and 3.4. An explicit forward Eulerian step follows the updated Lagrangian step, accounting for this material flow. The whole scheme is often referred to as Arbitrary Lagrangian Eulerian (ALE) method.

Convection

An ALE scheme by Stoker [70] accounts for the convective flow in two–dimensional triangular elements. The scheme is based on an interpolation approach, following the work of van Leer [75]. Here, an extension of this scheme is made towards triangular plate elements, in order to account for the convective flow in the multi–layer material model.

Membrane elements have one in–plane integration point, resulting in a constant distribution of the state variables across the element. Therefore, a first order accurate scheme was implemented, using this constant distribution of the state variables. A one–dimensional example of the convective problem is sketched in figure 3.5.

The magnitude of the state variable in the elements is shown vertically. Nodes 2 and 3 move with velocity v_c^2, v_c^3 respectively to the left hand side, resulting in material flow across the element boundaries. The convection scheme accounts for the change in magnitude of the state in the elements. The convective velocity in this example is found by:

$$v_c = v - v_g, \tag{3.25}$$

where v is the material velocity and v_g the mesh velocity. The material flow equals zero in this example.

The convective problem of a state variable ϑ is written as:

$$\vartheta' = \vartheta_{ref} + \Delta\vartheta_r, \tag{3.26}$$

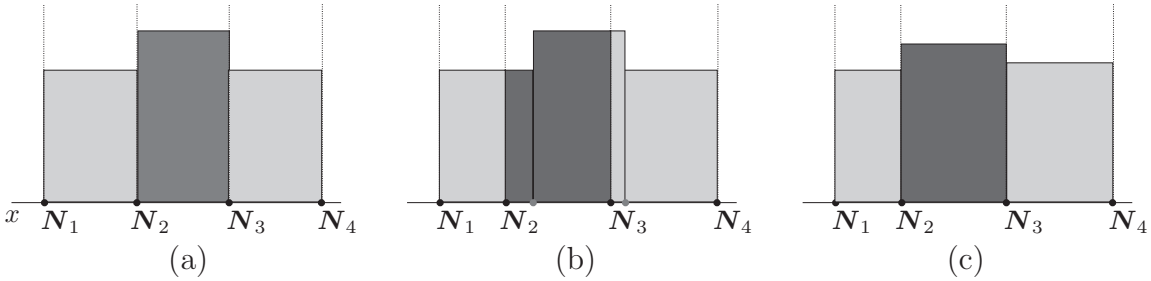

Figure 3.5: One–dimensional example of the convective problem. Two moving nodes in the mesh, N_2 and N_3 respectively, result in a convective flow in the elements; (a) The initial state; (b) The discontinuous distribution in the elements after shifting nodes 2 and 3; (c) The new distribution of the state variables.

where ϑ' is the state variable in the convected situation, the subscript ref indicates the reference situation and r represents the referential frame in $\boldsymbol{\chi}$ coordinates (see appendix A). The convected increment $\Delta\vartheta_r$ is:

$$\Delta\vartheta_r = \int_{t_0}^{t_1} \frac{\partial_g \vartheta}{\partial t} dt = \int_{t_0}^{t_1} (\dot{\vartheta} - \boldsymbol{v}_c \cdot \vec{\nabla}\vartheta) dt, \tag{3.27}$$

where

$$\vartheta(\boldsymbol{x}, t_0) = \vartheta_{ref}, \tag{3.28}$$

and t_0, t_1 are the beginning and the end of the timestep respectively. In order to maintain the boundary conditions at the boundary Γ of the domain, the following condition is imposed on all free boundaries:

$$\boldsymbol{v}_c \cdot \boldsymbol{n} = 0, \tag{3.29}$$

where $\boldsymbol{n}$ is the normal vector on the domain.

The kinematics for the ALE method are based on a referential description of motion (see appendix A). Here, the referential coordinate $\boldsymbol{\chi}$ equals the referential coordinate $\boldsymbol{X}_{ref}$ at the end of the implicit updated Lagrangian step.

The convective velocity $\boldsymbol{v}_c$ is required to solve equation (3.26). However, deriving $\boldsymbol{v}_c$ is not straightforward, since the individual ply deformations and velocities differ from the average composite deformation and velocity.

Convective velocity

The reference situation is normally used in a forward Euler convection scheme. Here, the reference situation for each ply is solved from the local energy minimization approach per element. The constants $c^i_{1,2,3}$ and $d^i_{1,2,3}$ per element define the internal nodes I^i_j for this element. Ply deformations in the adjacent elements in the FE mesh are solved using the same energy approach. As a result, it is unlikely that the internal nodes of the adjacent elements will coincide with the internal nodes of the current element (for the same element side). An example of this discrepancy in internal node positions in presented in figure 3.6.

The convective flow or flux of each ply through the element must remain equal to preserve

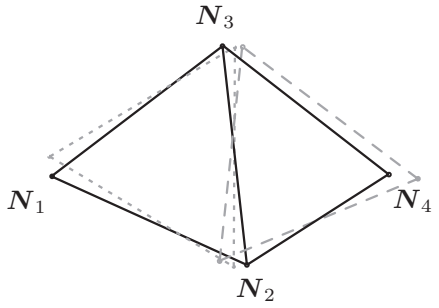

Figure 3.6: Deformations for the same ply in adjacent elements. The plies are depicted in the dotted grey lines. The average element configurations are presented in black lines.

conservatism, *i.e.* the same amount of material that flows in the element must also flow out of the element. An irregular mesh with overlapping plies in elements complicates conservatism and needs accounting for.

The average velocity over the side of the ply equals the velocity of the midpoint of the side of the ply since the velocity distribution is linear in the ply. The velocity at the midpoints of the sides of the plies follow from equation (3.14). The difference velocity $\boldsymbol{v}_{dif}^{i,k}$ between the midpoint of the side of ply i and the midpoint of the side of the average element for side k is:

$$\boldsymbol{v}_{dif}^{i,k} = \boldsymbol{v}_{mid}^{i,k} - \boldsymbol{v}_{mid}^{avg,k}, \tag{3.30}$$

where $\boldsymbol{v}_{mid}^{avg,k}$ is the velocity of the midpoint of a side for the average element. $\boldsymbol{v}_{mid}^{i,k}$ is the velocity at the midpoint of the ply side, or the material flow. The convective velocity for the ply i at the side k of the element is found using the normal direction $\boldsymbol{n}^k$ of the side of the average element as:

$$\boldsymbol{v}_{n}^{i,k} = \boldsymbol{n}^k \cdot \boldsymbol{v}_{dif}^{i,k}. \tag{3.31}$$

In figure 3.7 the fluxes in the multi–layer material model are shown in the shaded areas.

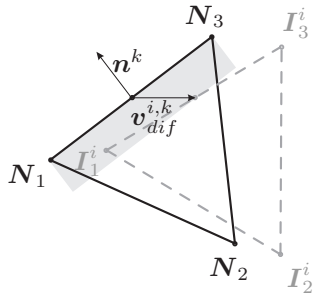

Figure 3.7: Fluxes and side velocity for ply i with respect to the average element.

Analogous, for the adjacent element, the convective velocity over the same side of the same ply in that element is determined. To obtain a conservative scheme the average

flow over each side of each ply in the element is considered:

$$\boldsymbol{v}_c^{i,k} = \tfrac{1}{2}(\boldsymbol{v}_n^{i,k,[e]} + \boldsymbol{v}_n^{i,l,[a]}), \tag{3.32}$$

where the suffix $[e]$ represents the current element and $[a]$ indicates the adjacent element. k and l indicate the shared side of the adjacent elements.

State variables

The state variables are stored in the integration point of the triangular membrane element. Not all state variables require convection. Here, only the fibre directions and fibre stresses are considered. The fibre stresses and directions determine the majority of the elastic response in the material model.

A commonly used test to verify the effectiveness of a convection scheme is the Molenkamp [78] test. An example of the Molenkamp test for the convection of the fibre directions is shown in appendix C.1.

3.4 Simulation control and boundary conditions

Next to the material model, additional information must be available for the FE model in order to perform simulations. First, the method to control the simulation is explained, then tool interaction and processing conditions are treated.

3.4.1 Simulation Control

The drape simulation is displacement controlled by moving the rubber mould towards the steel mould in small steps. For each displacement step, the system is solved using a predictor–corrector scheme (see section 3.1). Two convergence criteria are used in the predictor–corrector scheme: a load unbalance criterion and a displacement unbalance criterion [24].

The simulation stops when the rubber mould touches the steel mould. Both the rubber and steel mould are then in full contact with the composite plate. In reality, the pressing cycle does not stop at this point. The closed moulds are firmly pressed together under load control to consolidate the laminate. However, it is assumed that this part of the pressing cycle does not affect the fibre reorientation and it is therefore not simulated here.

3.4.2 Boundary conditions

Tooling must be included in the FE simulation in order to simulate the forming process of the composite. Contact between the composite plate and the mould surfaces is modelled by adding contact induced forces on the nodes of the FE mesh (Kloosterman [34]).

A penalty approach is used in the normal directions of the plate, allowing some penetration of the rigid tools in the composite plate. The normal traction $\boldsymbol{t}_n$ depends on the penalty parameter p_n and the penetration d in the normal direction $\boldsymbol{n}$ of the plate in the tool as:

$$\boldsymbol{t}_n = p_n \, d \, \boldsymbol{n}. \tag{3.33}$$

Viscous sliding friction was used with a constant friction factor in the tangential direction of the contact surface. The velocity difference is determined by:

$$\boldsymbol{v}_{rel} = \beta_c \, \boldsymbol{\tau}_{slip}, \tag{3.34}$$

where β_c is the constant friction factor for the tool–composite contact, $\boldsymbol{\tau}_{slip}$ the shear stress at the interface in the tangential direction. As a result, the constant friction factor is:

$$\beta_c = \frac{h_c}{\eta_c}, \tag{3.35}$$

where h_c and η_c are respectively the height and the viscosity of the interface layer between tool and composite.

3.5 Drape experiments

Drape experiments were performed at Stork Fokker AESP in Hoogeveen using the Rubber Press Forming (RPF) process. The product shape was a double dome geometry consisting of two intersecting hemispheres with different radii (see figure 3.8) [35]. The

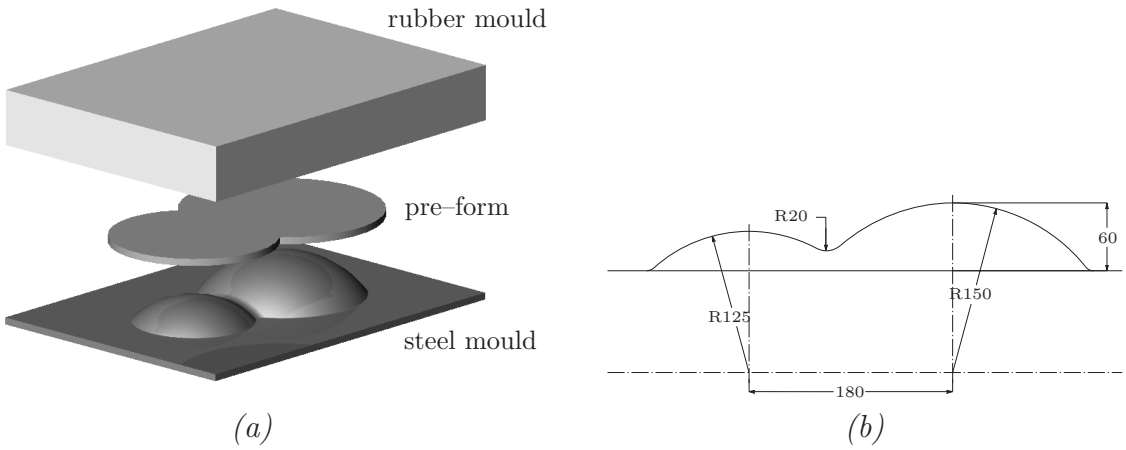

Figure 3.8: (a) Schematic view of the Double Dome rubber press tools and pre–form. (b) The dimensions of the lower steel mould in mm.

rubber tool is shown at the top of the figure, it is negatively shaped and moves downward towards the lower steel tool during production. The pre–form is held by a pre–form holder which also moves downward upon closing of the press. The pre–form holder is not sketched in the figure. The dimensions of the product are presented in figure 3.8.

Eight harness satin weave glass fibre reinforced PPS (Ten Cate Cetex © SS303) material was used to produce twelve laminates of 4 layers. Three laminates with a $[0°/90°|90°/0°]_s$ lay–up, three with a $[45°/\text{-}45°|\text{-}45°/45°]_s$ lay–up and three with a quasi-isotropic (QI) $[0°/90°|45°/\text{-}45°]_s$ lay–up were manufactured. Pre–forms were cut from these flat laminates prior to the RPF process.

The pre–forms were heated up to 360°C in an infrared oven during 220 seconds and immediately pressed in the RPF process. The press speed was set at 500 mm/s in the transport phase (the pressureless movement of the rubber tool) up to 50 mm above the

bottom position of the press where it switched to a pressure controlled movement. The press velocity in the pressure controlled stage is approximately 50 mm/s (see figure 3.11). The experimental results are shown in figure 3.9.

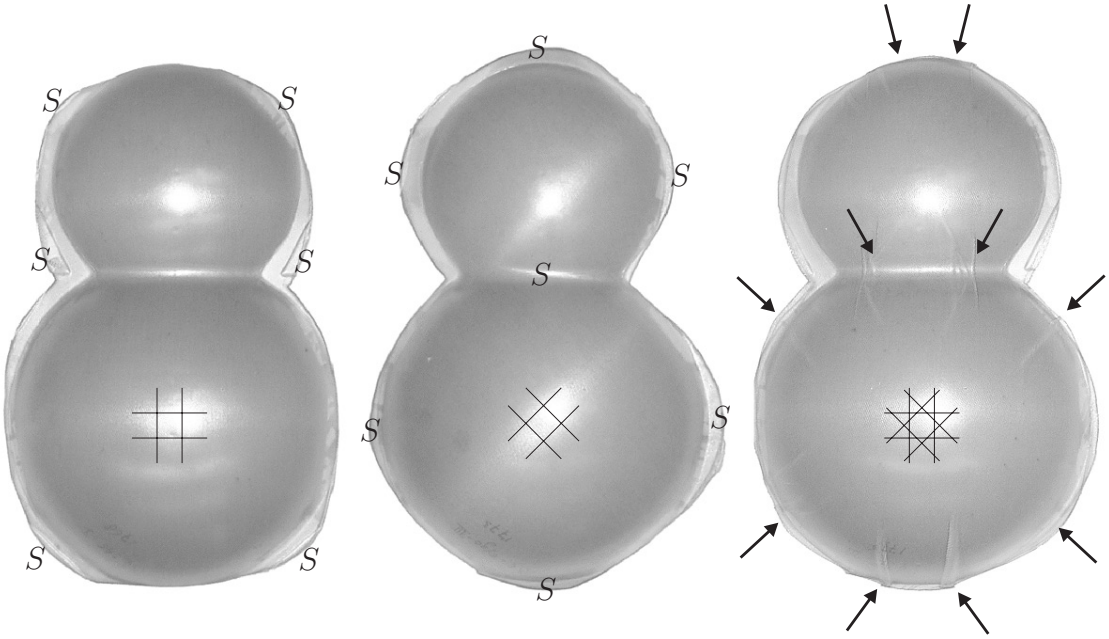

Figure 3.9: Drape results for the glass fibre reinforced PPS laminates; $[0°/90°|90°/0°]_s$, $[45°/\text{-}45°|\text{-}45°/45°]_s$ *and* $[0°/90°|45°/\text{-}45°]_s$ *lay–up. The initial fibre directions are indicated with lines at the centre of the large hemisphere.*

It is obvious from the experiments that the main fabric (shear) deformation occurs for both the [0°/90°] and the [45°/-45°] lay-ups in the bias directions of the weave (marked with an *S* in figure 3.9). However, the QI lay-ups behave in a completely different way. This laminate wrinkles (black arrows in figure 3.9) and shows far less shear deformation than the other two laminates.

3.6 Drape simulations

The simulated results for the double dome geometry are presented here. Draping is simulated with a geometrical draping method [7] and the FE draping method described in sections 3.2 and 3.3. First the results of the geometrical draping method are shown, followed by the results of the FE simulations.

3.6.1 Geometrical draping

The highest point strategy [7] was applied for the geometrical drape simulation. The initial point in the simulation was the top of the large hemisphere. The initial fibre directions were equal to the fibre orientations in the experiments. The results for the simulations are shown in figure 3.10, using a distance between the pivoting points of 3 mm.

The [0°/90°] and/or [45°/-45°] layers were draped sequentially to obtain the results for the QI laminates, since geometrical draping methods drape one layer at the time

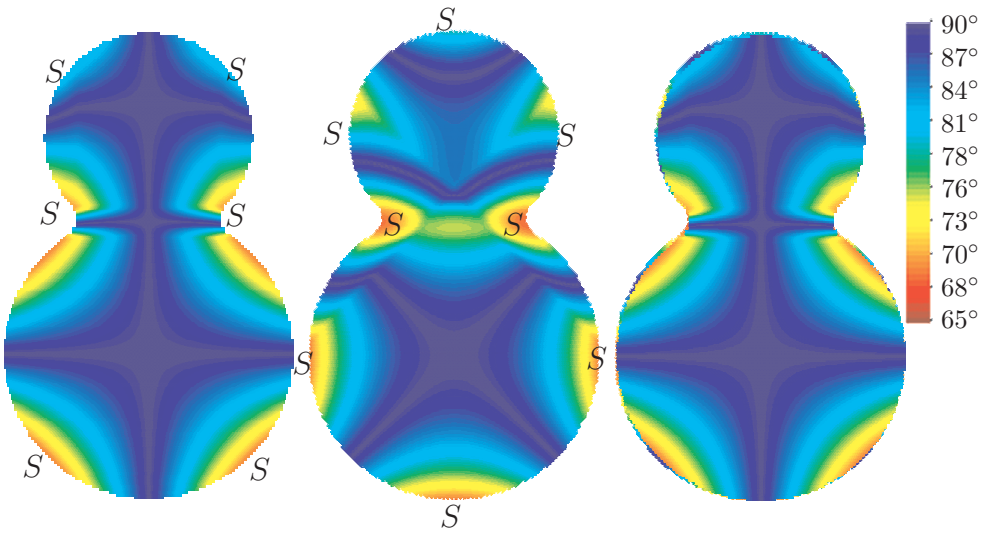

Figure 3.10: Drape results of the geometrical drape method, the angle $90 - |\theta|$ *is depicted as a function of the product shape. The results for a* $[0°/90°|90°/0°]_s$*, a* $[45°/-45°|-45°/45°]_s$ *and a QI lay–up are shown.*

only. Therefore no interaction between the individual plies in the laminate is taken into account. The results for the QI lay–up are hence simply a superposition of the cross–ply results. The CPU time used for this simulation was 15 seconds on a PC with an AMD XP2000 processor and 512 MB RAM.

3.6.2 Finite Element draping

Several geometries were simulated with the FE method. However, some drape predictions were not experimental validated. Drape simulations of an hemispherical product and wing leading edge stiffener are presented in appendix D. Here, the FE drape results of the double geometry are presented.

Draping the double dome was simulated using an unstructured mesh of 7948 membrane elements. The average length of the element sides is 6 mm with this mesh. For the predictor–corrector scheme a load and displacement unbalance criterion of 2% was used. Convergence was reached if both criterions were met.

The properties of the isotropic E–glass fibres, required for the representation of the yarns in the fabric, was obtained from literature [54]. The modulus of 72.4 GPa was used in both fibre directions. The material parameters m, n, η, η_1, η_2, η_3 and η_4 were fitted on the results from the picture frame experiments and are listed in table 2.1. The temperature during the isothermal forming simulation was assumed at 300℃. The effect of the fabric shear response was excluded from the simulations by setting the parameter m to 0 in some simulations.

The fibre volume fraction in the pre–forms was determined at 50%. It is assumed that the fibre volume fraction does not change during the forming stage. The distribution of the fibre families a and b was equal. The initial fibre directions were the same as in the experiments and the slip coefficient β for contact between the individual composite plies and the ply–tooling interface is listed in table 2.2. The experimentally determined thickness of the complete composite was 0.92 mm.

The velocity of the press is not constant during forming. The velocity is high at the beginning of the press cycle and then gradually reduces. The experimentally determined press velocity and the modelled velocity are shown in figure 3.11. The vertical position of the press is measured from the bottom of the lower tool. The velocity of the upper mould is negative since it moves down towards the lower mould. The simulated velocity of the upper mould is fitted onto the experimentally determined velocity. The velocity of the mould is controlled by reducing the displacement steps during the simulation, while the timesteps remain constant.

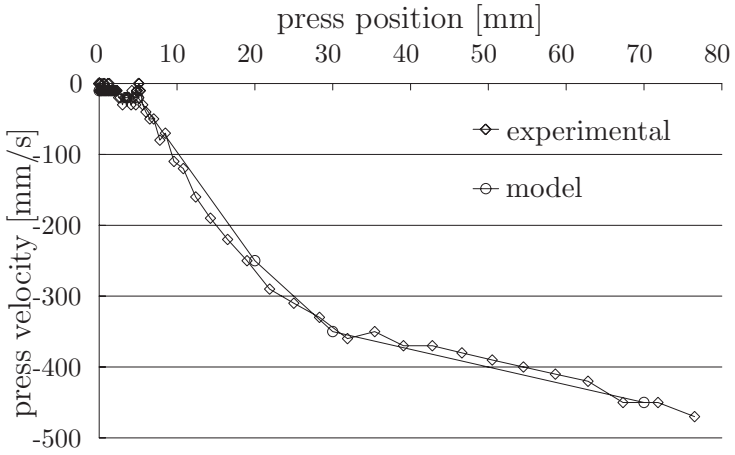

Figure 3.11: Press velocity versus press displacement.

The rubber mould and steel mould were both modelled using approximately 40000 triangular elements. The pre–form holder was not modelled, the pre–form was pressed down by the rubber mould. The results for the FE simulation are shown in figure 3.12.

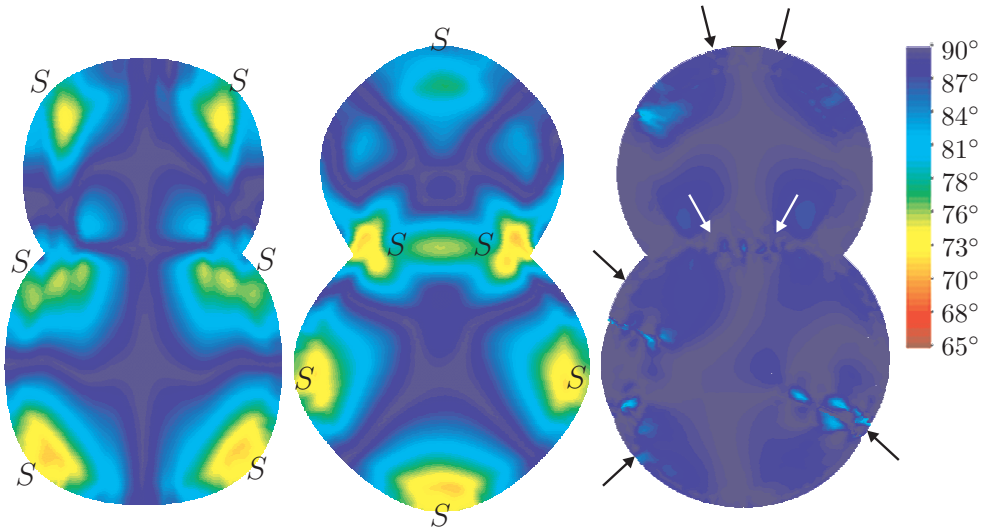

Figure 3.12: Drape results for FE draping method, the angle $90 - |\theta|$ is depicted as a function of the product shape.The results for three laminates are shown; a $[0°/90°|90°/0°]_s$, $[45°/\text{-}45°|\text{-}45°/45°]_s$ and QI lay–up.

In figure 3.12, the zones with the highest shear deformation are marked with an *S*.

Wrinkles are indicated with black arrows. The $[0°/90°|90°/0°]_s$ and $[45°/\text{-}45°|\text{-}45°/45°]_s$ lay-ups were simulated with the single layer material model (section 3.2). The QI lay–up was modelled using the multi–layer material model (section 3.3). The results are quite similar to the experimental results, the main shear deformation is predicted at the same positions. Wrinkles were found with the multi–layer drape simulation at similar positions as in the experiments.

The CPU time used for the single layer FE simulation was 35 minutes on a PC with an AMD XP2000 processor with 512 MB RAM. The simulation with the multi–layer material was computationally more intensive, it used 45 minutes.

3.7 Discussion

The discussion on the results of draping is split into three parts, the global product behaviour, the verification of the fibre redistribution and the fibre stresses induced by draping.

3.7.1 Global drape behaviour

The experiments clearly indicate that draping in the RPF process depends heavily on the lay–up of the fabric material. Draping $[0°/90°|90°/0°]_s$ and $[45°/\text{-}45°|\text{-}45°/45°]_s$ lay-ups resulted in smooth products. Wrinkles occurred in products draped with a QI lay–up, as the different deformabilities of the separate layers are restricted by the interlaminar transverse shear stiffness of the laminate.

At first glance, the results of both the geometrical and the FE drape methods look similar to the experimental drape results for the $[0°/90°|90°/0°]_s$ and $[45°/\text{-}45°|\text{-}45°/45°]_s$ products. Both methods predict large shear deformations of the fabric material in the bias directions (denoted with an in S in figures 3.10 and 3.12). The results at the smaller hemisphere however are quite different for the geometrical and FE simulations.

Excluding the fabric shear response resulted in slightly larger shear deformations of the composite. The effect of the fabric shear response is small since the material shear angle remains relatively small in the simulation. Pressing products that are more doubly curved will result in a more pronounced effect of the fabric shear response.

The geometrical and the FE drape simulations predict completely different results for the QI lay–up. The geometrical drape simulation can not predict the wrinkles observed in these experiments since it does not take the interlaminar transverse shear stiffness into account. Simulating draping by modelling the forming behaviour of individual layers sequentially is clearly no solution for draping multi–layered pre–forms with different reinforcement directions in each ply. The multi–layer FE simulation incorporates the through–thickness laminar shear phenomenon and accounts for the interaction between the laminate layers. Shear deformations in one ply are restrained by the fibres in the other ply since the fibre directions of the individual plies are rotated over 45° in the QI lay–up. Wrinkles during forming result from this interaction.

Membrane elements are not the preferable type of elements in order to predict wrinkling. Elements that account for bending, such as the Discrete Kirchhoff Triangle [13], are preferable for this purpose.

3.7.2 Verification of the fibre redistribution

The enclosed fibre angle was measured in the area between the two hemispheres (the ridge) and at the longitudinal axis of the product to evaluate the prediction of both drape methods qualitatively. The results for the ridge are depicted in figures 3.13 and 3.14, the results for the longitudinal axis are shown in figure 3.15. The dotted lines in figures 3.13, 3.14 and 3.15 represents the edge of the product. The line at $y = 0$ indicates the symmetry line of the product. The error bars on the experimental values are based on the standard deviation of the measurement and the accuracy of the angle measurement system.

The results of the FE simulations including the shear response are indicated with *FE-Lock* in figures 3.13, 3.14 and 3.15. The results without fabric shear response are indicated with *FE-NoLock* in figures 3.13, 3.14 and 3.15. First the results for the $[0°/90°|90°/0°]_s$ lay–up are discussed, then the results for the $[45°/\text{-}45°|\text{-}45°/45°]_s$ lay–up and finally the results for the QI lay–up are evaluated.

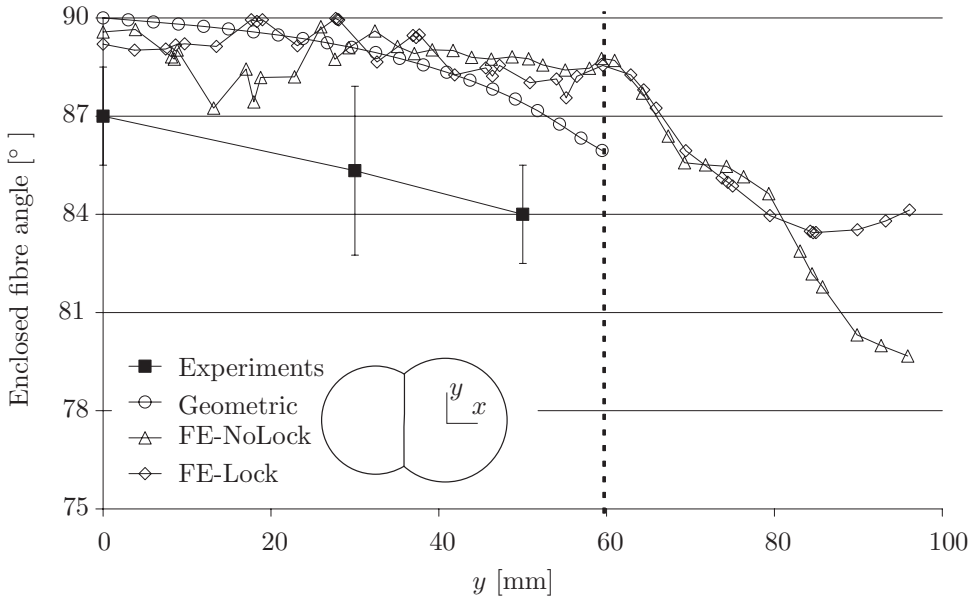

Figure 3.13: Enclosed fibre angle for the $[0°/90°|90°/0°]_s$ *lay–up at the ridge.*

Both the geometrical and the FE draping methods predict the correct trend for the $[0°/90°|90°/0°]_s$ lay–up. The predicted enclosed fibre angles of both methods approximate the experimental values. The experiments show a small deviation of 3° from a 90° enclosed fibre angle at the centreline. This 3° deviation is possibly caused by a misalignment of the fibres in the pre–forms or by a misalignment of the pre–form during forming. Both the geometrical and the FE draping method do not predict this deviation since both methods used initially orthogonal weaves in their simulation, with the orientation of the warp fibres parallel to the symmetry axis of the product.

Including the fabric shear response in the FE simulations results in a smaller deviation of the enclosed fibre angle across the ridge for the $[0°/90°|90°/0°]_s$ lay–up compared to the FE simulation without the shear response.

The FE simulations for the $[45°/\text{-}45°|\text{-}45°/45°]_s$ lay–up approximate the experimental results better further from the centreline of the product, while the geometrical draping

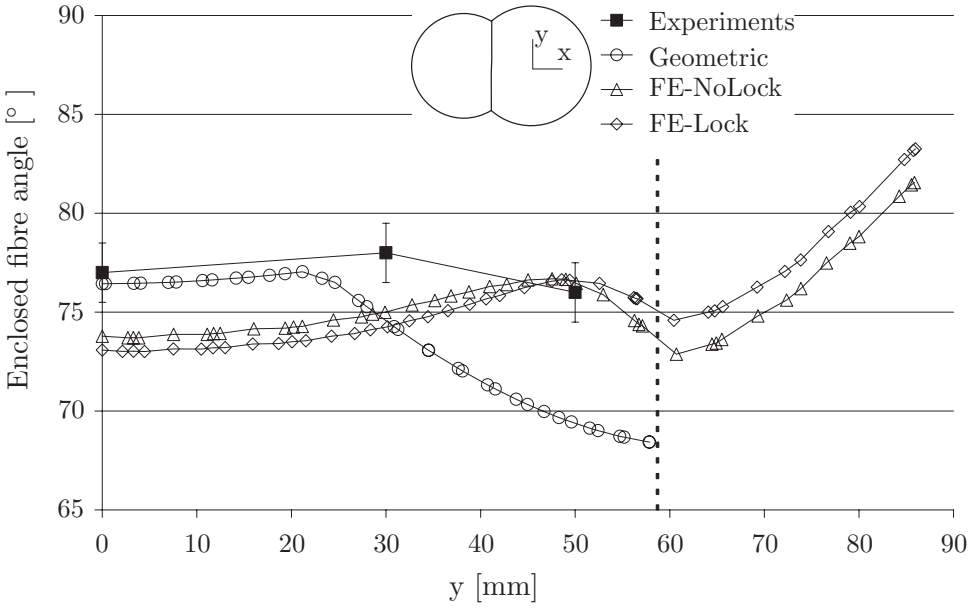

Figure 3.14: Enclosed fibre angle for the $[45°/-45°|-45°/45°]_s$ *lay–up at the ridge.*

method predicts better closer to the centreline for the $[45°/-45°|-45°/45°]_s$ lay–up. The error in the experimental values is significantly smaller for this lay–up, indicating a more reproducible result. Including the fabric shear response in the FE simulations only results in minor changes of the fibre redistribution.

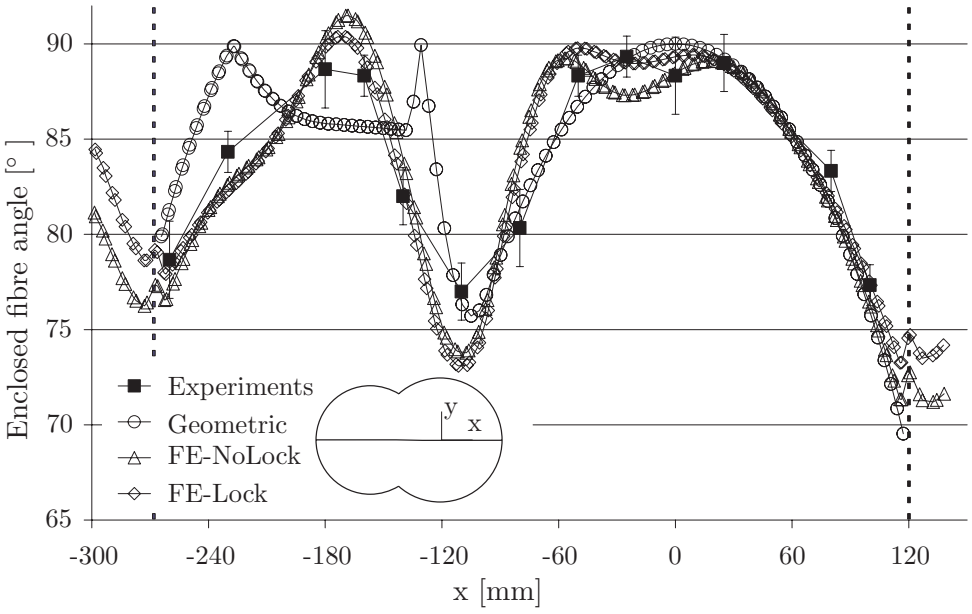

Figure 3.15: Enclosed fibre angle for the $[45°/-45°|-45°/45°]_s$ *lay–up at the longitudinal axis.*

The enclosed fibre angle is presented for the $[45°/-45°|-45°/45°]_s$ lay–up at the longitudinal axis of the product in figure 3.15. The experimentally determined enclosed fibre angles are approximately 88° at the top of the large hemisphere. The angle decreases

when moving away from the centre of the large hemisphere. However, on the side of the smaller hemisphere, the enclosed fibre angle remains 88° up to approximately -50 mm, suddenly decreasing to 76° in the ridge at -110 mm. The enclosed fibre angle then increases again towards the centre of the smaller hemisphere, where it reaches 88° at -180 mm. The enclosed angle decreases again towards the outside of the smaller hemisphere.

Both methods predict the enclosed fibre angle very well at the outside of the large hemisphere (right hand side of figure). The accuracy of the predicted angles deteriorates when moving towards the smaller hemisphere of the product. The composite is in contact with the steel mould in more than one zone during the forming stage. The resulting bridging causes less accurate predictions of the geometrical draping method.

The geometrical drape simulation shows a smooth change in the angle between the fibre families at the larger hemisphere, but some abrupt changes in the enclosed fibre angle are predicted on the smaller hemisphere at approximately -130 mm and -230 mm. The highest point strategy, applied to predict the resulting fibre angles, causes these abrupt changes. Both FE simulations predict a smoother distribution of the enclosed fibre angle on the product, following the trend of the experiment nicely, also on the smaller hemisphere.

3.7.3 Stresses induced by draping

Stresses are induced in the product during draping. These stresses will depend on, for example, the lay–up of the composite, the material properties, the product shape, the forming velocity and the size of the FE mesh. The mesh size was varied in order to investigate the dependency of the fibre stresses on the mesh–size. The fibre stresses in the first fibre direction (0° direction) resulting from a simulation with a $[0°/90°|90°/0°]_s$ lay–up are depicted in figure 3.16.

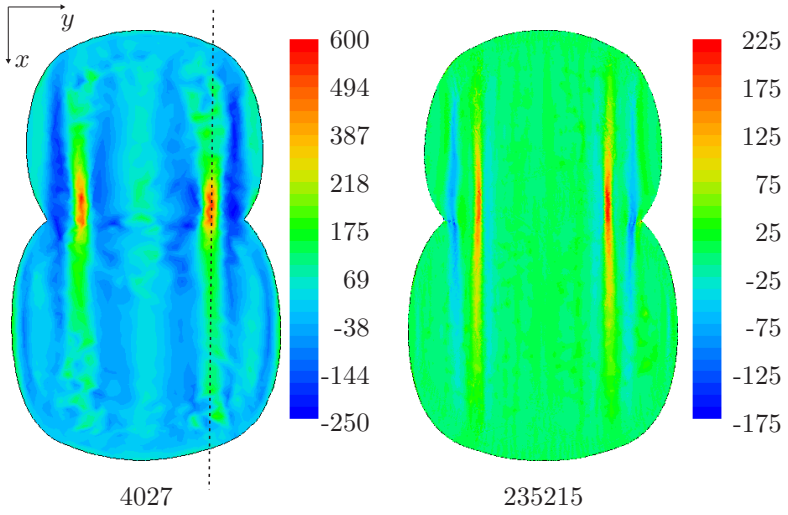

Figure 3.16: The predicted fibre stresses (MPa) in the longitudinal direction of the double dome product using a $[0°/90°|90°/0°]_s$ *lay–up in the FE method. Two meshes are depicted: a course mesh of 4027 elements and a fine mesh of 235215 elements. The average element size is 8 mm and 1 mm respectively.*

The fibre stresses in the fibre family in the longitudinal direction of the double dome geometry are fairly high. The maximum tensile stresses occur in the ridge of the double dome geometry. The maximum compressive stresses occur in the area next to the zone with these high tensile stresses. Both the course and the fine mesh predict a similar stress distribution.

The maximum fibre tensile stresses are approximately 600 MPa and the maximum compressive stress is around -250 MPa for the course mesh. A mesh sensitivity analysis shows a significant reduction of these stresses with increasing mesh size, as depicted in figure 3.17.

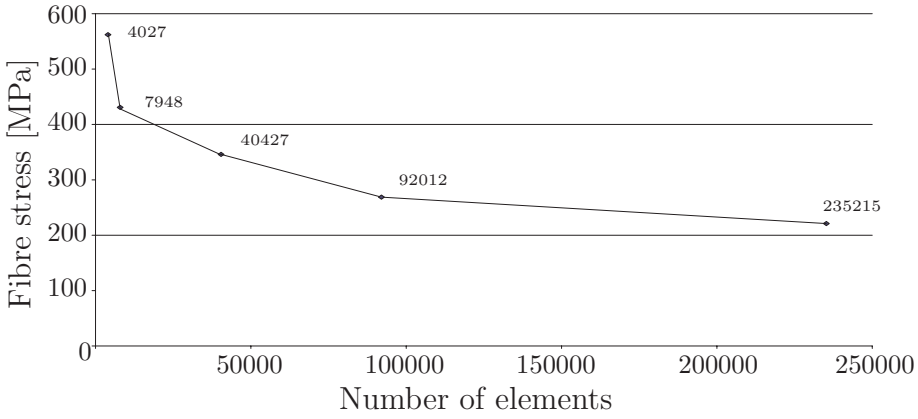

Figure 3.17: Stress convergence with increasing mesh size. Maximum fibre tensile stresses in 0° direction for the $[0°/90°|90°/0°]_s$ *lay–up.*

The cause for these high fibre stresses can be explained from one–dimensional equilibrium, or:

$$\frac{\partial \sigma_{xx}}{\partial x} + \frac{\partial \sigma_{yx}}{\partial y} = 0. \tag{3.36}$$

The shear stress σ_{yx} and the stress σ_{xx} along the dotted line in figure 3.16 are plotted as a function of the x–coordinate in figure 3.18.

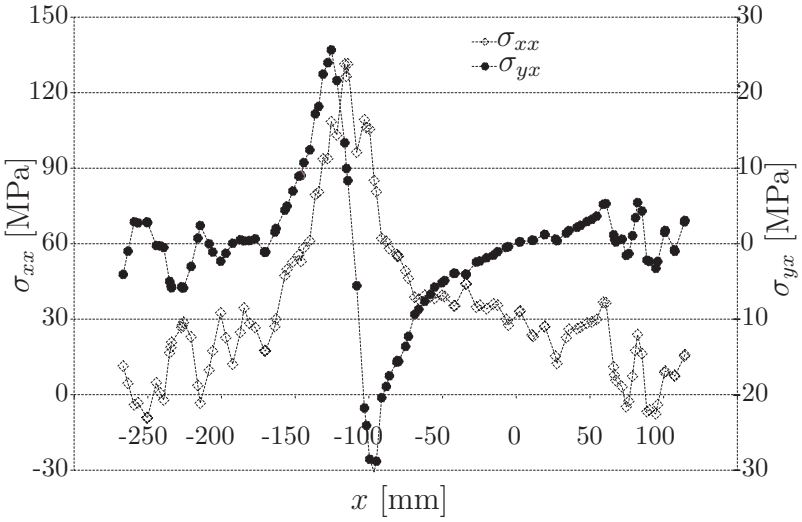

Figure 3.18: σ_{xx} *and* σ_{yx} *versus* x*.*

Both σ_{yx} and σ_{xx} have steep gradients around $x = -120$ mm. The enclosed fibre angle changes significantly at this position, see figure 3.12. Very large shear deformations occur in the area with the maximum σ_{xx}. The elements in this area, the ridge of the double dome, are too course to account for the correct deformation behaviour, resulting in an overestimation of the stress gradients.

The high fibre stresses are caused by the strain in the fibres. However, the contribution of the fibre stresses to the complete stress response is related to the volume fraction of the fibres (see (2.8)). The stress in these fibres thus account for only a quarter of the total stress response in this drape simulation since $V_{f_a} = \frac{1}{4}$. So, even a slight overestimation in the strain in this direction results in a significant increase in the fibre stress.

Cherouat and Billoët [16] showed that fibre straightening occurs when extending a fabric in the fibre direction. Fibre straightening or slip of fibres through the fabric is not accounted for in the current model, the results for the fibre stresses are likely to be an overestimation. The stresses inside the product were not experimentally determined. Strain measurement in the fibre directions can provide the required information to validate these fibre stresses.

3.7.4 Multi–layer model versus multiple membrane elements through–the–thickness

A simulation with multiple membrane elements through–the–thickness is performed in order to verify the multi–layer material model with for an QI lay–up. The mesh of the multi–layer model used 7914 elements. The mesh of the model with multiple membrane elements through–the–thickness consisted of two layers of 7914 elements on top of each other. The laminate lay–up is [0⁰/90°|45⁰/-45°]. The material, contact between the individual layers and the tooling was modelled with the same parameters as the multi–layer model.

The simulation time with the model using 2 element layers through–the–thickness of the sheet was 6.5 hours. The multi–layer material model is approximately 7 times faster in predicting the draping of the double dome geometry. However, this simulation time is when modelling the composite with only 2 instead of 4 layers of material through–the–thickness. Using 4 element layers through–the–thickness of the sheet would increase the computational times even more since the DOF's in the simulation increase linearly with the number of element layers. Reducing the element size in the mesh affects the computational times in a similar manner.

The results of the two models are compared in two stages. First, the global drape behaviour and the enclosed fibre angles are compared and finally the fibre stresses will be discussed.

The global drape predictions of the two models are quite similar, as shown in figure 3.19.
Both models wrinkle in the same areas as the experimental QI lay–up. The multi–layer material model wrinkles slightly more. The fibre reorientation for both models is similar as well. Both predict less fibre reorientation in the 0⁰/90° and 45⁰/-45° layers than $[0^0/90^\circ|90^0/0^\circ]_s$ lay–up and $[45^0/-45^\circ|-45^0/45^\circ]_s$ lay–up models did.

The predicted fibre stresses with the multi–layer material model and the model with multiple membrane elements through–the–thickness are different. The stress patterns in

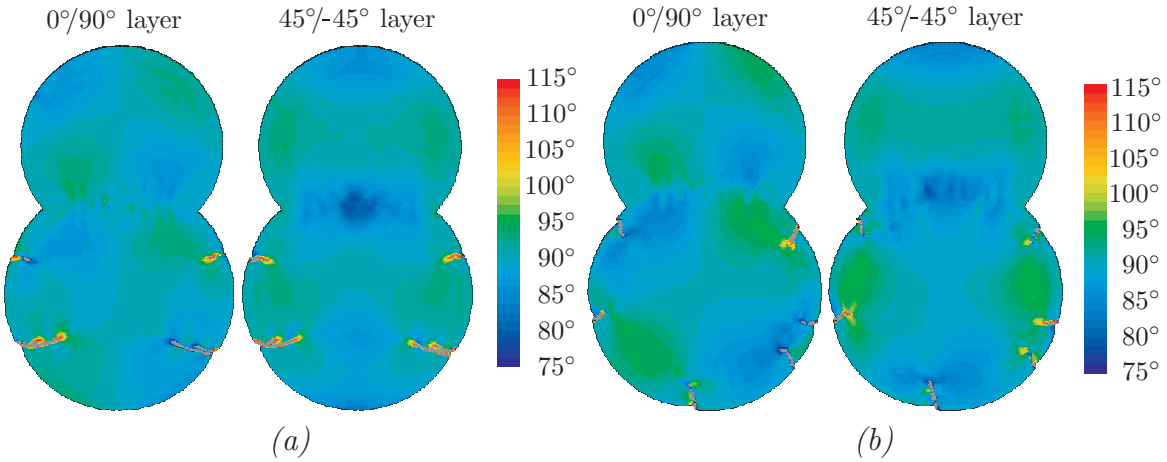

Figure 3.19: Enclosed fibre angle predictions for QI lay–up; (a) Multiple stacked membrane elements (b) Multi–layer drape model.

both models are similar, but the magnitude of the stresses is not. The multi–layer model predicts approximately 1.5 times higher stresses than the model with multiple elements through–the–thickness, as depicted in figure 3.20.

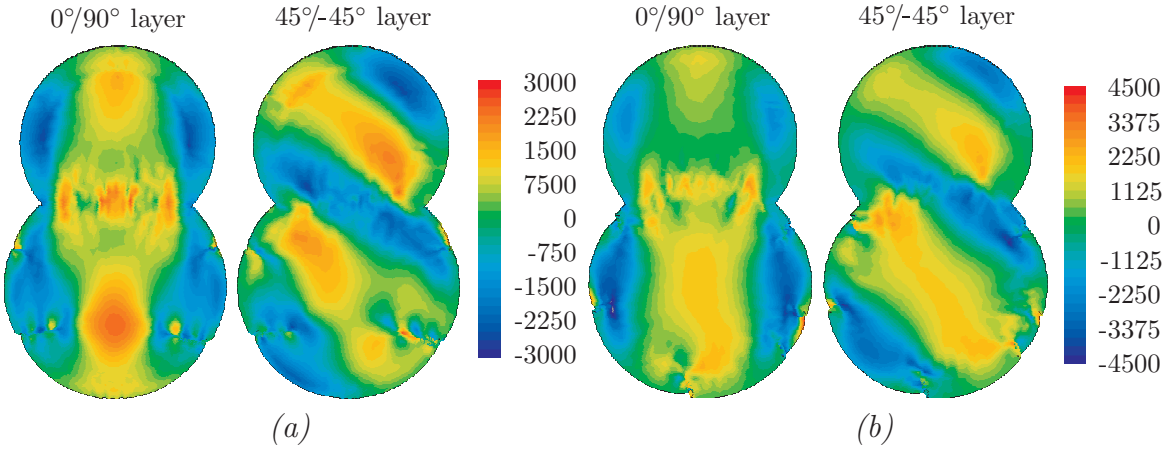

Figure 3.20: Fibre stresses (MPa) in first fibre direction; (a) Multiple stacked membrane elements (b) Multi–layer drape model.

The difference in stresses can be explained by the number of interfaces in the models. The multi–layer material model has three contact areas between the individual fabric layers. The model with multiple membrane elements through–the–thickness of the sheet only has one. The effect of the interface is thus less in this model, resulting in better a deformable material and lower stresses in the fabric layers.

However, the fibre stresses are unrealistically high in both models. Again, these fibre stresses reduce with mesh refinement in the multi–layer material model. The fibre stresses did not reduce to a value below the yield stress of glass. A possible explanation for the overestimation of the fibre stresses is that the individual layers are not fully in contact during forming. An overestimation of the shear interaction results from this. Cheruet *et al.* [17] showed that porosities occur during the forming stage of thermoplastic composites. However, the occurrence of these porosities was not validated during the forming of the double dome geometry.

3.8 Conclusions

A multi–layer extension to the fabric reinforced fluid model was implemented in an implicit FE model. Drape simulations of the Rubber Press Forming process were performed with the FE model, geometrical draping method and using multiple membrane elements through–the–thickness of the composite plate.

The results were compared with experiments. Experiments on a double dome geometry show a clear dependency of the drape behaviour on the laminate lay–up. Quasi Isotropic lay–ups drape significantly worse than $[0°/90°|90°/0°]_s$ and $[45°/\text{-}45°|\text{-}45°/45°]_s$ lay–ups. The QI lay–ups lead to wrinkling, the other lay-ups not.

At the ridge of the double dome geometry, the geometrical draping method and the FE simulations both predict the enclosed fibre angles equally well. However, the FE simulations predict the experimental trend better on the longitudinal axis of the $[45°/\text{-}45°|\text{-}45°/45°]_s$ product, especially at the smaller hemisphere. The geometrical drape method is less accurate on the smaller hemisphere since multiple contact zones occur during draping.

Sequential drape predictions are definitely no solution for draping multi–layered composites, due to the clear dependency of the drape behaviour on the lay–up of the composite. Neglecting the interlaminar shear between the composite layers during draping causes the model to overestimate the drape–ability.

The multi–layer material model provides a computationally attractive tool to model draping of multi–layered composites. The results were compared with the experiments and with a model using multiple elements through–the–thickness of the composite sheet. The two models and the experiments confirm the clear dependency between the drape behaviour and the laminate lay–up.

The fibre stresses from draping are evaluated in the single layer and multi–layer material model. The predicted stresses were quite high and possibly an upper bound result for the fibre stresses. The stresses reduce significantly when more elements are used in the simulation. A validation of these stress predictions is not possible since they were not measured in the experiments.

3.9 Recommendations

Several recommendations for the drape implementation are suggested.

The model predictions of the fibre stresses in the multi–layer material model are considered too high. This is possibly caused by an assumption in material model. Viscous friction is assumed for the contact behaviour of the interfaces between the tooling and the composite and between the individual composite layers. The interface behaviour is not likely to be completely viscous as discussed in chapter 2. Porosities between the individual layers can also occurs during the forming, resulting in an overestimation of the contact area between the interfaces. Additionally, the fibres are modelled linearly elastic, allowing no fibre straightening, and no fibre slip is assumed. An overestimation of the fibre stresses can results from these model assumptions. More research in this area should give more insight in this problem.

Bending needs to be incorporated in the material model in order to accurately predict wrinkling. The multi–layer material model requires extension to incorporate the height of the plies in the laminate. Also, an extension from membrane elements to, for example,

Discrete Kirchhoff Triangle elements is required.

A high number of elements is required in order to reduce the fibre stresses in the model predictions. Elements with higher order displacement fields should be able to incorporate the shear deformations better. It is therefore recommended to use these higher order elements in order to predict draping with FE models.

Chapter 4

Woven fabric composite properties

The previous two chapters considered the forming stage in the production of composite products. An initially flat laminate with orthogonal fabric layers was formed onto a mould, leading to fibre reorientation. The forming, or draping, of the woven fabric composites was modelled, resulting in a prediction of the fibre re–arrangement. This re–arrangement causes the angle between the warp and fill fibre family to vary, *i.e.* the fabric weave looses its orthogonality.

The stiffness properties and thermal expansion coefficients of composites strongly depend on the fibre orientation. A widely applied modelling technique for predicting these thermo–elastic properties of laminates built from unidirectional plies is the Classical Laminate Theory (CLT). The CLT is applied to flat plies in laminates where the fibre distribution and arrangement is homogeneous at the ply level. Weaves do not have a homogeneous fibre distribution, their fibres are concentrated in yarns. Additionally, the yarns are undulated in the weave. Therefore, the CLT cannot be applied directly to find the thermo–elastic properties of composites built from woven fabric reinforced composite materials.

Here, a model is presented that accounts for the structure of the weave and the fibre re–arrangement resulting from forming. It extends the CLT to account for the inhomogeneous fibre distribution in the weave and the undulation of the yarns. The model predicts the stiffness properties and thermal expansion coefficients of flat laminates builtup from non–orthogonal woven fabric plies. These thermo–elastic properties are required in order to model the shrinkage and warpage of the composite product, see chapter 5. The model is verified with tensile tests and thermal expansion measurements on non–orthogonal weaves. Two types of fabric weaves were verified, a plain weave and a 8H satin weave.

4.1 Review on thermo–elastic modelling

Several models have been developed to predict the in–plane thermo–elastic properties of various fabric weaves. In the early nineties, Ishikawa and Chou [18, 19] developed three one–dimensional models for various types of orthogonal woven fabric composites: the mosaic model, the crimp model, and the bridging model. At the same time, the two–dimensional model of Naik and Shembekar [49, 50] described the full geometry of plain weave fabric laminates. The model predicts the in–plane elastic properties, based on the Classical Laminate Theory [56] and assuming a mixed parallel–series arrangement

of infinitesimal pieces. Based on this model, Falzon and Herzberg [25] considered the effect of the laminate configuration on the strength and stiffness properties in 1996. Vandeurzen and Verpoest [76,77] developed a Microsoft Excel© application, TEXCOMP, that describes the three–dimensional geometry of various fabric weaves. Based on this geometry, they developed a model that predicts the three–dimensional elastic properties of fabric composites. At the end of the nineties, Akkerman and De Vries [1] developed a two–dimensional model for orthogonal fabric weaves. In 2000, Lamers *et al.* [36] extended this model predicting the thermo–elastic properties of non–orthogonal, or skewed, weaves. The model presented here is a refinement of this work by adapting the yarn shape, resulting in better predictions of the weave properties. Recently, Hofstee *et al.* [28] presented a similar CLT based model to predict the thermo–elastic properties of thermo–formed skewed plain weaves.

4.2 Methodology

The weave is built from yarns, which consist of several thousands of fibres. The yarns cross over and under each other in weave patterns, introducing a waviness, or undulation, in the yarns. Undulated yarns are not orientated in the plane of the composite, and thus contribute less to the planar stiffness of the composite than yarns which remain in the plane. A geometrical model describes the weave pattern and the resulting waviness.

The fibres and the resin are not homogeneously distributed in the weave. The fibres are concentrated in the yarns and the matrix material is located in and around the yarns, bonding the fibres and transferring load. As a result, the fibre volume fraction is inhomogeneously distributed in the weave. It is generally accepted that the fibre volume fraction significantly affects the properties of the composite material. It is thus important to distinguish the geometry of the yarns in the composite in order to find the thermo–elastic properties of the composite.

A so called *top–down–bottom–up* method is employed to predict the thermo–elastic properties of a fabric reinforced composite (see figure 4.1). The method consists of two parts: the geometrical sub–division of the composite, or geometrical analysis, and the subsequent rebuilding of the weave with its thermo–elastic properties, or thermo–elastic analysis. The geometrical analysis is performed first, then the thermo–elastic analysis. Four structural levels are distinguished in the *top–down–bottom–up* method: the macro, the meso, the mini and the micro level.

The macro level considers the complete laminate. The geometrical analysis distinguishes the individual plies in the composite. It accounts for the lay–up of the composite. This part of the analysis is treated in section 4.3.1. The thermo–elastic analysis at the macro level (section 4.4.4) utilises a CLT based homogenisation technique to determine the composite properties.

The meso level accounts for the weave architecture of the individual plies (section 4.3.2). Repetitive Volume Elements (RVE) are determined in the weave at this level. These RVE's are built from basic elements, the building block of any bi–axial weave. The thermo–elastic properties of the individual fabric layers are determined in section 4.4.3.

The mini level considers the basic elements of the weave. These building blocks distinguish the areas of resin and yarns and account for the undulation of the yarns. The geometrical description of the basic elements is covered in section 4.3.3. The thermo–

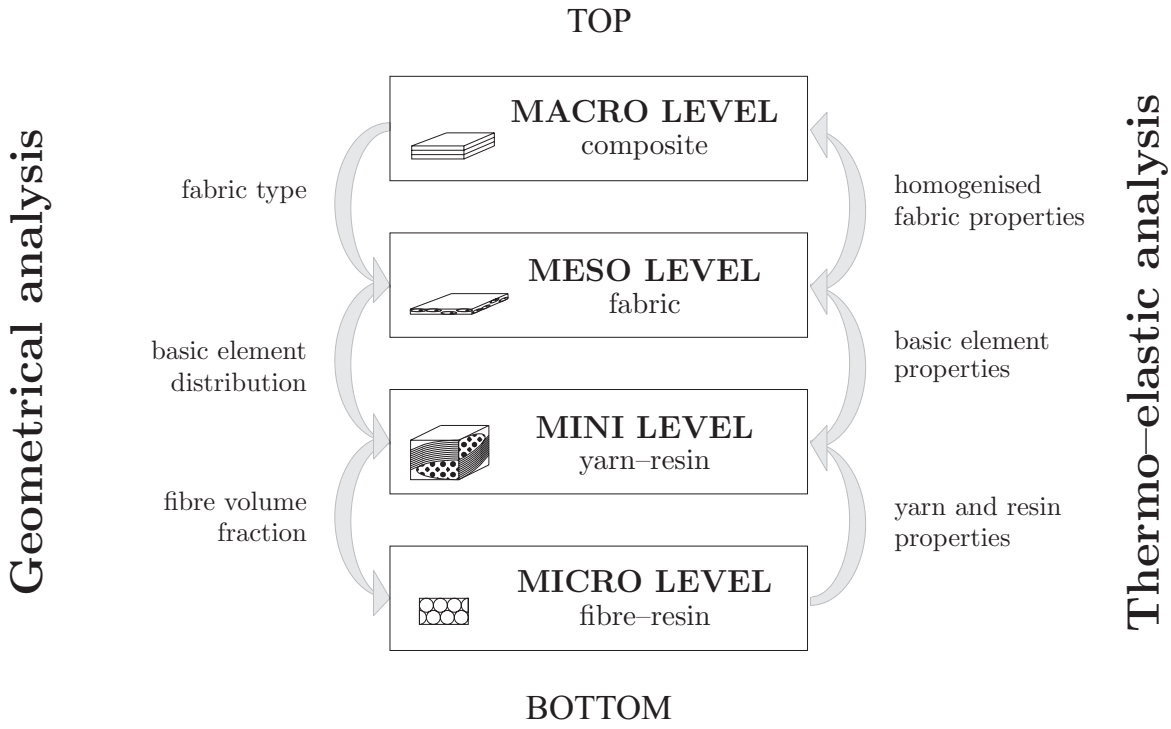

Figure 4.1: Top–down–bottom–up–method to predict the thermo–elastic properties of composites.

elastic counterpart is treated in section 4.4.2.

Micromechanics are applied to obtain the homogenised properties of the yarns, combining the properties of fibres and resin at the micro level. The micro level geometrical analysis is considered in section 4.3.4 while the thermo–elastic analysis is covered in section 4.4.1.

4.3 Geometrical analysis

The geometrical analysis, the *top-down* part of figure 4.1, considers the geometrical structure of the composite. The four levels, the macro, the meso, the mini and the micro level are treated in the following sections.

4.3.1 Macro level geometrical modelling

The composite is builtup from a number of plies. The lay–up, or stacking sequence, of these plies determines the structure of the composite. Symmetrical or non–symmetrical stacking sequences are distinguished at this level. The thickness, structure and orientation of the individual fabric layers are determined. Nesting of the individual plies is not taken into account; the fabric composite is considered as a flat ply with constant thickness.

4.3.2 Meso level geometrical modelling

The meso level considers the fabric ply and accounts for the weave architecture. The two yarn families, the warp and the fill yarns, are arranged into a specific order that identifies the weave pattern. RVE's can be distinguished at the meso level since the weave pattern is repetitive. These RVE's are the smallest regions that still can represent the weave, and are found in any two–dimensional weave.

The size of the RVE is determined by a specific number of warp and fill yarns for each weave pattern. Examples of a plain weave RVE and a satin RVE are depicted in figure 4.2.

The objective is to find building blocks within these RVE's. These building blocks, or basic elements (see section 4.3.3), model the weaves structure in order to distinguish areas of warp yarn, fill yarn and resin and account for the undulation in the yarns. Three RVE's for a plain weave are presented on the top part of figure 4.2. The plain weave RVE is 2 by 2 yarns and has four yarn crossings. Similarly, an RVE for an 8H satin weave is shown on the bottom half of the figure. It is 8 by 8 yarns.

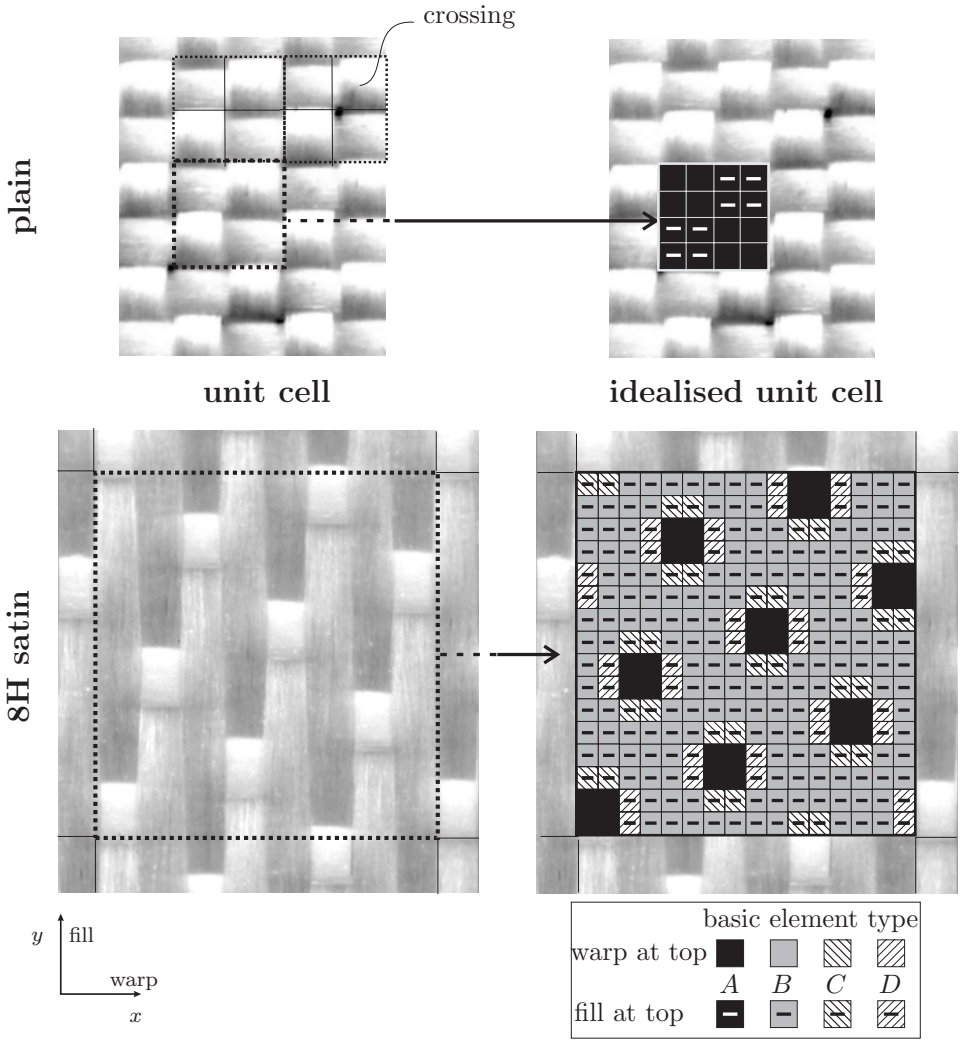

Figure 4.2: Repetitive Volume Element representation of a plain weave and an 8H satin glass weave by basic elements.

Focusing on the plain weave RVE, it is observed that the fill yarn passes under and over the warp yarn respectively. The warp yarn passes over and under the fill yarn. Both yarn families are constantly undulated. Four yarn crossings occur in one plain weave RVE. Basic elements are used to represent these yarn crossings. Each crossing is represented by four basic elements.

The crossings in the plain weave can be modelled by one type of basic element, taking symmetry and anti–symmetry rules into account, as shown in figure 4.2. Both the warp and the fill yarn are undulated in this basic element. The name of the basic element type is A and is shown in black. Some of the A type basic elements have a minus sign in figure 4.2, indicating that the fill yarns are on top. The plain weave RVE is modelled by 16 basic elements.

An example of an 8H satin RVE, marked with the dotted line, with most fill yarns on top is depicted in figure 4.2. Each fill yarn passes over seven warp yarns and then under one warp yarn in an 8H satin weave. Each warp yarn passes over seven fill and then under one fill yarn. The 8H satin RVE contains 64 crossings. Both the warp yarn and fill yarn are straight in most of these crossings.

The 8H satin RVE is composed of 256 basic elements. Four different types of basic elements can be distinguished: A, B, C and D. Both the warp and the fill yarn are undulated in basic element A. Both the warp yarn and fill yarn are straight in basic element B. Basic elements C has a straight warp yarn and undulated fill yarn and basic element D has a straight fill yarn and an undulated warp yarn.

Each RVE of any bi–axially woven fabric can be described with these four different types of basic elements. The four basic element types and their yarn shape are listed in table 4.1.

Table 4.1: Basic elements and their yarn shape

Basic element	**A**	**B**	**C**	**D**
Warp shape	undulated	straight	straight	undulated
Fill shape	undulated	straight	undulated	straight

The structure of the basic elements is modelled at the mini level in the next section.

4.3.3 Mini level geometrical modelling

Regions of warp yarns, fill yarns and pure resin can be distinguished in the fabric composite. The basic elements represent the geometry of the fabric, as shown in section 4.3.2. The regions of warp yarn, fill yarn and resin are bounded by the yarn surfaces. These yarn surfaces are represented by geometrical shape functions for each of these basic elements, similar to the work of Naik and Shembekar [49, 50].

The yarn shape functions are defined by the yarn cross–sectional shape functions and the yarn mid–line functions. First the cross–sectional shape functions of the yarns are described, then the mid–line yarn functions. Finally, the description of the yarn surfaces is presented.

Yarn cross–sectional shape

The cross–section of the yarns are approximated with an ellipsoidal shape, possibly with a straight mid–section. The yarn cross–section is assumed to be constant along the yarn axis. The thickness or height of the yarn is assumed to be half of the thickness of the dry fabric, *i.e.* both fibre families have the same height in the current implementation. The longitudinal axis of the warp yarn is in the direction of the x–axis and the fill yarn is perpendicular to the warp yarn. A schematic representation of warp yarn cross–sectional shape in the yz–plane is given in figure 4.3.

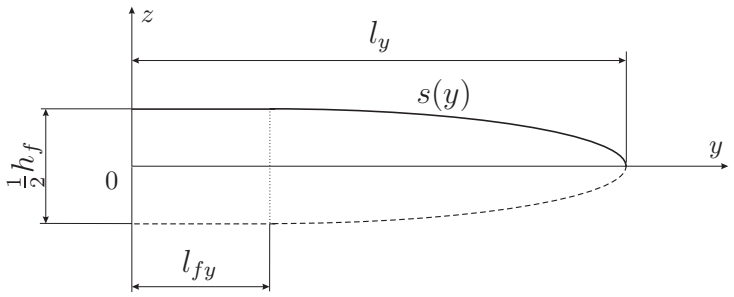

Figure 4.3: Cross–sectional shape of the warp yarn in the yz–plane.

In figure 4.3, the length of the yarn is denoted with l_y, the height with $\frac{1}{2}h_f$ and the yarn's straight part with l_{fy}. The function $s(y)$ describes the contour of the right–top quarter of the yarn's cross–section. It consists of a straight part and a undulated part.

The length of the straight part is defined using an undulation factor. The undulation factor U_y relates the length of the straight part in the yarn's cross–section to the length l_y by:

$$l_{fy} = (1 - U_y) l_y. \tag{4.1}$$

The mathematical representations of $s(y)$, while accounting for the undulation, reads:

$$s(y) = \begin{cases} \frac{1}{4}h_f & \text{if} \quad 0 \leq y < l_{fy} \\ \frac{1}{4}h_f \sqrt{\left(1 - \frac{(y - l_{fy})^2}{{l_y}^2 {U_y}^2}\right)} & \text{if} \quad l_y \geq y \geq l_{fy} \end{cases} \tag{4.2}$$

The entire contour of the warp yarn's cross–section is determined by combining the symmetric and anti–symmetric parts of $s(y)$. Similarly, a cross–section can be defined for the fill yarns in the xz–plane. It reads:

$$s(x) = \begin{cases} \frac{1}{4}h_f & \text{if} \quad 0 \leq x < l_{fx} \\ \frac{1}{4}h_f \sqrt{\left(1 - \frac{(x - l_{fx})^2}{{l_x}^2 {U_x}^2}\right)} & \text{if} \quad l_x \geq x \geq l_{fx} \end{cases}, \tag{4.3}$$

where U_x is the undulation factor, l_x is the length in the cross–section of the fill yarn and l_{fx} is the length of the straight part in the cross–section of the fill yarn.

Yarn mid–line shape

The yarn families pass under and over each other in the fabric, resulting in undulation of the yarn families in their longitudinal direction. The height coordinate of the centre

of the cross–section from the yarn thus changes in its longitudinal direction, as shown in figure 4.4.

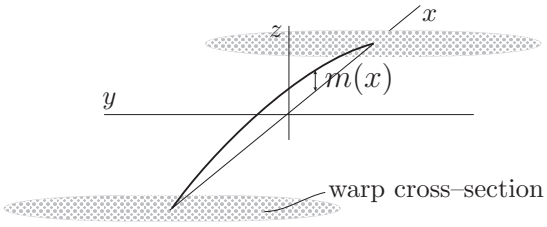

Figure 4.4: The warp yarn mid–line path. The fill yarn is not sketched for the propose of clarity.

Yarn contact is assumed at the crossings of the two fibre families. The shape of the mid–line path thus follows the cross–section of the other fibre family since the yarns do not penetrate or separate. Three parts define the mid–line path: I the straight part where the yarns are in contact; II the undulated part where the yarns are in contact; III a straight part where the yarns are not in contact. A schematic representation of the mid–line path function $m(x)$ of the warp yarn is presented in figure 4.5.

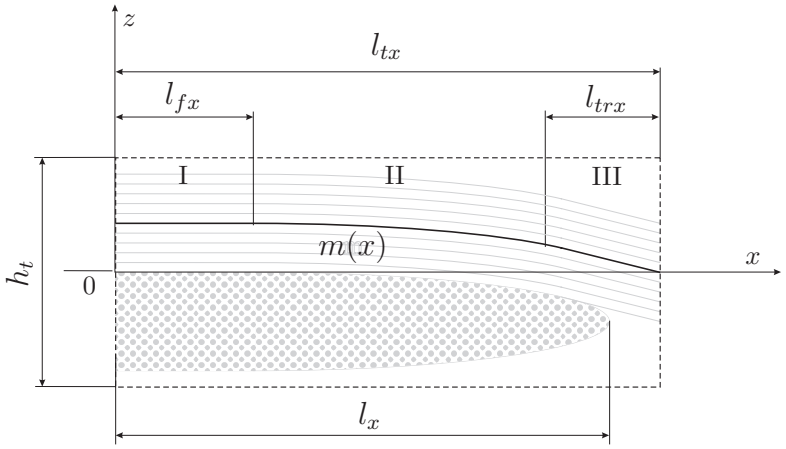

Figure 4.5: Mid–line path of the warp yarn in the xz–plane. The zones define the yarn mid–line.

In figure 4.5, h_t is the total thickness of the ply, l_{tx} is the length of the basic element in the x–direction and l_{trx} is the length of the straight part if the yarns are not in contact. The three parts of the mid–line function $m(x)$ are described by:

$$m(x) = \begin{cases} m_I(x) = \frac{1}{4}h_f & \text{if} \quad 0 \le x < l_{fx} \\ m_{II}(x) = \frac{1}{4}h_f\sqrt{\left(1 - \frac{(x - l_{fx})^2}{{l_x}^2{U_x}^2}\right)} & \text{if} \quad (l_{tx} - l_{trx}) > x \ge l_{fx} \\ m_{III}(x) = \frac{1}{4}h_f\frac{x - l_{tx}}{\sqrt{(l_{tx} - l_{fx})^2 - (l_f - l_{fx})^2}} & \text{if} \quad l_{tx} \ge x \ge (l_{tx} - l_{trx}) \end{cases} \tag{4.4}$$

The subfunction $m_{III}(x)$ in zone III, the straight part where the yarns are not in contact, is derived by solving the length of the straight part l_{trx}. The mid–line function $m(x)$ is

required to be smooth and continuous over the full length, so the length l_{trx} is determined by applying a second order continuity condition at $x = l_{tx} - l_{trx}$:

$$m_{II}(x = l_{tx} - l_{trx}) = m_{III}(x = l_{tx} - l_{trx}); \tag{4.5}$$

$$\left.\frac{\partial m_{II}(x)}{\partial x}\right|_{x=l_{tx}-l_{trx}} = \left.\frac{\partial m_{III}(x)}{\partial x}\right|_{x=l_{tx}-l_{trx}}. \tag{4.6}$$

The length l_{trx} follows from solving (4.6), it reads:

$$l_{trx} = \frac{(l_{tx} - l_{lfx})^2 - (l_{fx} - l_{lfx})^2}{l_{tx} - l_{lfx}}. \tag{4.7}$$

The length l_{tx} of the basic element in the x–direction follows from the number of yarns per unit of length in the weave. The length is defined by :

$$l_{tx} = \frac{1}{2c_x}, \tag{4.8}$$

where c_x is the number of fill yarn per unit of length, or fill count. Again, the complete mid–line of the yarn can be described by combining symmetric and anti–symmetric variants of $m(x)$. Similarly, the mid–line function $m(y)$ of the fill yarn in the yz–plane is derived, it reads:

$$m(y) = \begin{cases} m_I(y) = \frac{1}{4}h_f & \text{if} \quad 0 \le y < l_{fy} \\ m_I(y) = \frac{1}{4}h_f\sqrt{\left(1 - \frac{(y - l_{fy})^2}{{l_y}^2{U_y}^2}\right)} & \text{if} \quad (l_{ty} - l_{try}) > y \ge l_{fy} \\ m_I(y) = \frac{1}{4}h_f\frac{y - l_{ty}}{\sqrt{(l_{ty} - l_{fy})^2 - (l_f - l_{fy})^2}} & \text{if} \quad l_{ty} \ge y \ge (l_{ty} - l_{try}) \end{cases}, \tag{4.9}$$

where l_{ty} is the length of the basic element in the y–direction and l_{try} is the length of the straight part if the yarns are not in contact. The length l_{try} is derived similarly to the length l_{trx}. It reads:

$$l_{try} = \frac{(l_{ty} - l_{lfy})^2 - (l_{fy} - l_{lfy})^2}{l_{ty} - l_{lfy}}. \tag{4.10}$$

The length of the basic element in the y-direction is calculated from:

$$l_{ty} = \frac{1}{2c_y}, \tag{4.11}$$

where c_y is the warp count.

The basic elements A, B, C and D have straight and/or undulated yarns, as shown in table 4.1. The mid–line path functions of each of the basic elements define wether the yarn is undulated or straight. Setting $U_{x,y}$ to zero results in straight yarn paths in basic elements B, C and D.

Yarn surface functions

The yarn surface functions define the interfaces between regions of pure resin and yarns in the basic elements. The height position of the yarn surface h is created by a summation

of the yarn mid–plane function m and the cross–sectional yarn shape functions s. The yarn mid–plane functions and the yarn shape functions are defined in perpendicular planes. The warp yarns are defined in the x–direction, the fill yarns are defined in the y–direction. The surfaces of the two fibre families are defined by:

$$\begin{aligned} h_T^{We}(x,y) &= m^e(x) + s(y) \\ h_B^{We}(x,y) &= m^e(x) - s(y) \\ h_T^{Fe}(x,y) &= -m^e(y) + s(x) \\ h_B^{Fe}(x,y) &= -m^e(y) - s(x) \end{aligned}, \tag{4.12}$$

where $h_T^{We}(x,y)$ and $h_B^{We}(x,y)$ define the warp top and bottom and $h_T^{Fe}(x,y)$ and $h_B^{Fe}(x,y)$ define the fill top and bottom interface for basic element e. Six surfaces define all interfaces when also defining the top and bottom plane. Combining symmetric and anti–symmetric basic elements describes the RVE. The graphical representation of the basic elements using the geometrical shape functions is displayed in figure 4.6.

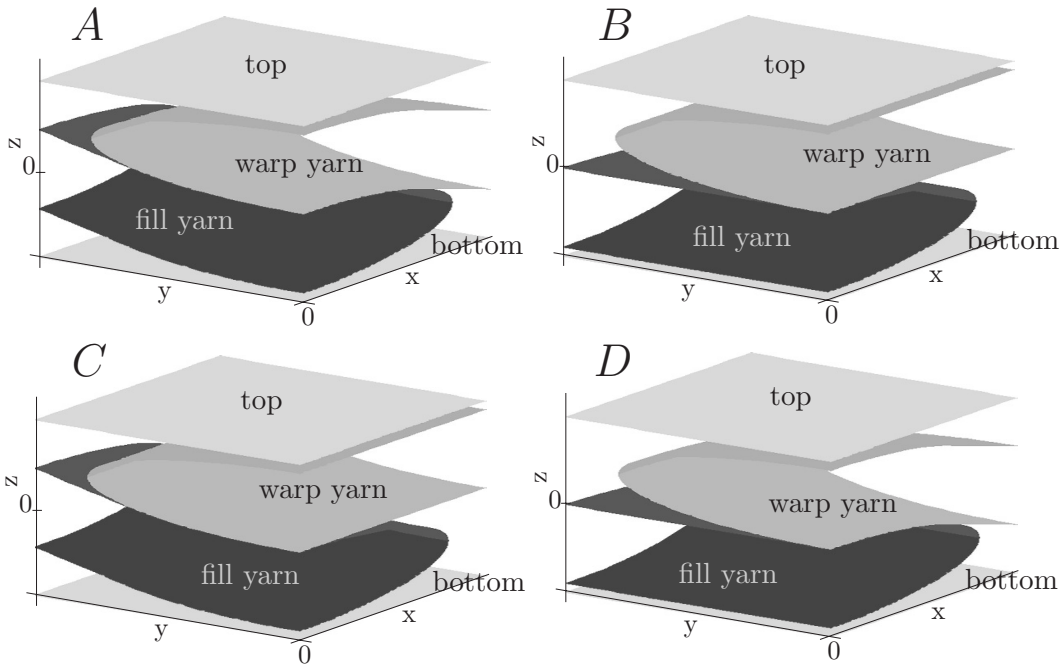

Figure 4.6: Basic elements A, B, C and D.

The yarn height is constant in the xy–plane with the given shape functions (4.12). Therefore, the thickness in the undulated part differs from the thickness in the straight part of the yarn, as depicted in figure 4.7.
The yarn thickness is constant over its length. However, this second order deviation has no major effect on the resulting properties when the undulation angles remain smaller than 20° [25].

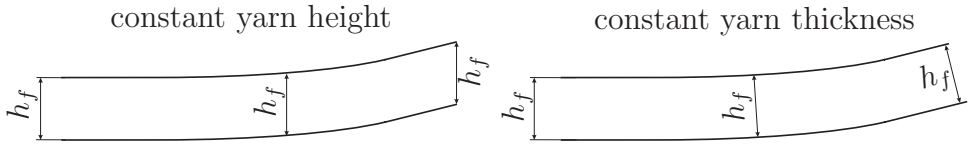

Figure 4.7: Yarn modelled with constant yarn height and constant yarn thickness.

Ply thickness

The undulation of the yarns depends on the thickness of the composite ply. The thickness of each fabric ply is determined by:

$$h_t = \frac{\rho_w}{V_f^C \rho_f}, \tag{4.13}$$

where V_f^C the composite fibre volume fraction and ρ_f the fibre density. ρ_w is the areal density of the weave, which is usually supplied by the manufacturer.

Yarn fibre volume fraction

The yarn fibre volume fraction is required to determine the thermo–elastic properties of the yarns. The size of the warp yarn, fill yarn and matrix regions determines the average fibre volume fraction in the yarn regions. Micromechanical models are used to predict the material properties in the principal directions of the yarn (see section 4.4.1).

The shape functions define the regions with pure matrix material and regions with impregnated yarns (figure 4.6). The fibre volume fraction in the fibre bundles can be determined from geometrical considerations. The yarn fibre volume fraction, V_f^Y, can be related to the overall fibre volume fraction of the composite, by:

$$V_f^Y = \frac{\Omega^O}{\Omega^Y} V_f^C, \tag{4.14}$$

with Ω^O as the overall or total volume of the basic element and Ω^Y as the yarn volume. The superscript Y represents either the warp or fill yarn.

Shear transformation

The fabric is neither orthogonal nor uniformly deformed in many applications. Shear deformations of the weave beyond 30° are not uncommon during the production of composite products, as shown in chapter 2. The thermo–elastic properties need to be defined as a function of the skew angle for the prediction of shrinkage and warpage. Skewed means a shear deformation of the weave in this context, where the cross–over points in the weave act as pivoting points. The skew angle equals the material shear angle θ in equation 2.13. The deformation is not pure shear since the thickness of the weave increases during shearing.

A transformation of the geometry is applied to incorporate the skew deformation, transforming the orthogonal axes into skewed axes, as depicted in figure 4.8, or mathematically described by:

$$\left\{ \begin{array}{c} x' \\ y' \end{array} \right\} = \left[\begin{array}{cc} 1 & 0 \\ \cos 2\phi & \sin 2\phi \end{array} \right] \cdot \left\{ \begin{array}{c} x \\ y \end{array} \right\} \tag{4.15}$$

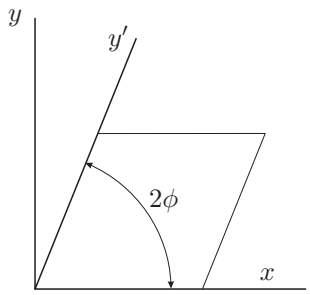

Figure 4.8: Shear transformation.

where x' and y' are the transformed axes and 2ϕ the enclosed fibre angle. The area of the RVE decreases with increasing skew angle as a result of this in–plane transformation. It was observed in the picture frame experiments (chapter 2) that the composite thickness increases during shear deformation, while the volume remained constant. The thickness of the fabric in deformed axes is related to the initial thickness by:

$$h(x', y') = \frac{h(x, y)}{\cos(2\phi_o - 2\phi)}, \tag{4.16}$$

where $h(x, y)$ is the thickness of the ply corresponding to the initial fabric angle $2\phi_o$.

4.3.4 Micro level geometrical modelling

The micro level geometrical modelling considers the microstructure of the yarns. Each yarn usually contains of several thousand fibres and resin. The fibres in the yarns are arranged along the yarn axis. Packing models idealise the arrangement of the fibres in the yarns. Generally two fibre idealisation models are considered: the square and the hexagonal packing. The square and hexagonal packing structures are depicted in figure 4.9.

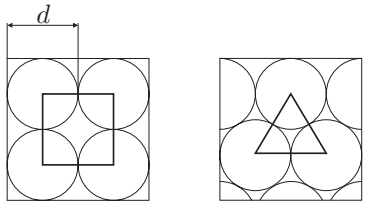

Figure 4.9: Square and hexagonal packing of fibres.

The packing structure also determines the theoretical maximum fibre volume fraction when assuming circular fibre cross–sections. When the fibres have a diameter d the maximum volume fraction for the square packing is:

$$V_f = \frac{\frac{1}{4}\pi d^2}{d^2} = \frac{\pi}{4} \approx 0.785. \tag{4.17}$$

The maximum fibre volume fraction for the hexagonal packing is:

$$V_f = \frac{\frac{1}{8}\pi d^2}{\frac{1}{4}\sqrt{3}d^2} = \frac{\pi}{2\sqrt{3}} \approx 0.907. \tag{4.18}$$

The maximum fibre volume fraction in the square packing is 13% lower than the maximum fibre volume fraction in the hexagonal packing.

4.4 Thermo–elastic analysis

The mechanical analysis, the *bottom–up* part in figure 4.1, considers the thermo–elastic properties of the composite. The four levels: micro, mini, meso and macro level are treated in the following sections.

4.4.1 Micro level thermo–elastic modelling

Mechanical modelling at the micro level considers the thermo–elastic properties of the yarns and the resin. The resin is assumed isotropic, and its thermo–elastic properties are therefore straightforward to derive. The properties of the yarns are derived by micromechanical modelling.

Micromechanical models predict the elastic properties and the thermal expansion coefficients of UD materials. The micromechanical models account for anisotropy in the constituents, the composition and the internal microstructure (fibre size, shape, and packing geometry) to predict the macroscopic properties of the UD material.

Two types of predictions will be examined: models that predict the elastic properties and models that predict the linear thermal expansion coefficients. An extensive survey on these model was published by Whitney and McCullough [80]. However, splitting the models into two types does not imply that the models are based on a different theoretical approach. The predictions from, for example, the rule–of–mixtures models for elastic properties are based on exactly the same approach as the rule–of–mixtures models for the prediction of the linear thermal expansion coefficients.

Elastic properties models

The use of the simple iso–stress and iso–strain models as the rule–of–mixtures models [80] is widely applied, although they are known to underestimate the transverse properties of the composite. More advanced non–uniform stress or strain field energy based models such as the Composite Cylinder Assemblage (CCA) model by Hashin [26] or the Chamis models [14] are also used by several authors. The use of semi–empirical models, such as the Puck model [51] or Halpin–Tsai models [80], is also widely spread.

A micromechanical model was selected based on a UD composite study. An E–glass/epoxy composite with a fibre volume fraction of 55% was selected in order to perform this study. The material parameters of the constituents was obtained from literature [12, 54]. The measured values of the elastic and thermal properties of the composite are also obtained in the literature [22]. The best fitting models for the UD material were the rule–of–mixtures model in the longitudinal fibre direction and the Composite Cylinder Assemblage (CCA) model in the transverse to the fibre direction. The results of the two models are combined to predict the UD properties in the longitudinal and transverse direction.

Coefficient of thermal expansion models

Similarly to the elastic properties models, many models to predict the thermal expansion are available in literature. Again, the simple iso–stress and iso–strain based rule–of–mixtures [80] models can be applied to find the linear thermal expansion coefficients of UD materials. Other models such as the Schapery model [62], the models proposed by Rosen and Hashin [61], the Chamberlain model [10], or the Schneider model [63] can also be found in literature.

The micromechanical models are selected based on a similar study as the elastic properties models in section 4.4.1. The rule–of–mixtures model fitted the literature data [22] best in the longitudinal fibre direction. The Schapery model approximated the transverse thermal expansion coefficients best. Two models are combined to predict the thermal expansion coefficients in the longitudinal and transverse direction.

4.4.2 Mini level thermo–elastic modelling

The thermo–elastic properties of the basic elements are calculated using the geometrical representation of the weave from section 4.3.3. The properties of the basic elements are subsequently used to determine the RVE thermo–elastic properties. First, the elastic properties of the basic elements are derived, then the thermal behaviour of the basic elements are determined.

Elastic properties

It is assumed that the CLT [56] is applicable to each of the basic elements. The CLT is based on the Kirchhoff plate theory, which assumes plane stress and zero transverse shear. The strain profile through–the–thickness $\{\varepsilon(z)\}$ of thin plates is given by:

$$\{\varepsilon(z)\} = \{\varepsilon^o\} + z\{\kappa\}, \tag{4.19}$$

where $\{\varepsilon^o\}$ and $\{\kappa\}$ are the mid–plane strain and curvature of the plate and z the height coordinate. The stress profile $\{\sigma(z)\}$ follows automatically by multiplying equation (4.19) with the elastic in–plane stiffness matrix $[Q(z)]$:

$$\{\sigma(z)\} = [Q(z)] \cdot \{\varepsilon(z)\}. \tag{4.20}$$

The load and moment vector N_i and M_i result from the integration of the stress profile from equation 4.20 through–the–thickness, as:

$$\begin{aligned}
\{N\} &= \int_{h_B}^{h_T} \{\sigma(z)\}\, dz = \int_{h_B}^{h_T} [Q(z)] \cdot \{\varepsilon(z)\}\, dz \\
&= \int_{h_B}^{h_T} [Q(z)] \cdot (\{\varepsilon^o\} + z\{\kappa\})\, dz \\
\{M\} &= \int_{h_B}^{h_T} \{\sigma(z)\}\, z\, dz = \int_{h_B}^{h_T} [Q(z)] \cdot \{\varepsilon(z)\}\, z\, dz \\
&= \int_{h_B}^{h_T} [Q(z)] \cdot (z\{\varepsilon^o\} + z^2\{\kappa\})\, dz
\end{aligned}, \tag{4.21}$$

where h_B is the bottom and h_T is the top coordinate of the ply. Writing equation 4.21 in matrix form results in:

$$\left\{ \begin{array}{c} N \\ M \end{array} \right\} = \int_{h_B}^{h_T} \left[\begin{array}{cc} Q(z) & Q(z)\,z \\ Q(z)\,z & Q(z)\,z^2 \end{array} \right] \cdot \left\{ \begin{array}{c} \varepsilon^o \\ \kappa \end{array} \right\} dz \tag{4.22}$$

As a result, the constitutive equation for the CLT based mechanical properties for a ply is:

$$\left\{ \begin{array}{c} N_i \\ M_i \end{array} \right\} = \left[\begin{array}{cc} A_{ij} & B_{ij} \\ B_{ij} & D_{ij} \end{array} \right] \left\{ \begin{array}{c} \varepsilon_j^o \\ \kappa_j \end{array} \right\}, \qquad \text{where } i,j = 1,2 \text{ or } 6 \tag{4.23}$$

with

$$(A_{ij}, B_{ij}, D_{ij}) = \int_{h_B}^{h_T} Q_{ij}(z)\,(1, z, z^2)\,dz \tag{4.24}$$

in which h_B is the bottom coordinate, and h_T is the top coordinate of the ply.

$[Q(z)]$ is piecewise constant through–the–thickness for laminates builtup from unidirectional (UD) plies. Additionally, for UD plies, $[Q(z)]$ is independent of the in–plane coordinates x and y and the height coordinates of each ply remains constant. The integral from equation (4.24) can be solved straightforwardly.

Here, the boundaries for integration in equation (4.24) are determined by the yarn surface functions in the basic element. Additionally, the yarns are undulated. The homogenised properties of the warp yarn, fill yarn and resin were derived in section 4.4.1. As a result, $[Q(z)]$ is piecewise constant in the thickness direction for any position (x, y) in the basic element.

The warp yarns, fill yarns and resin each have an in–plane stiffness matrix. The resin is isotropically; the resin in–plane stiffness matrix $[Q^R]$ is constant over the basic element. The warp yarn and fill yarn are rotated in the plane and undulated in the basic element.

The in–plane stiffness matrix of the yarn $[Q^Y]$, where the suffix Y stands for warp or fill respectively, is defined in xyz–coordinates and obtained from an in–plane rotation of the $[\tilde{Q}^Y]$ stiffness matrix by [56]:

$$[Q^Y] = [T]^{-1} \cdot [\tilde{Q}^Y] \cdot [R] \cdot [T] \cdot [R]^{-1}, \tag{4.25}$$

where $[\tilde{Q}^Y]$ is defined in the ply 123–coordinates, which lie in the yarn directions. $[R]$ is the Reuter matrix and $[T]$ is the in–plane rotation matrix:

$$[T] = \left[\begin{array}{ccc} \cos^2\zeta & \sin^2\zeta & 2\sin\zeta\cos\zeta \\ \sin^2\zeta & \cos^2\zeta & -2\sin\zeta\cos\zeta \\ -\sin\zeta\cos\zeta & \sin\zeta\cos\zeta & \cos^2\zeta - \sin^2\zeta \end{array} \right], \tag{4.26}$$

where the angle ζ is defined by the in–plane orientation of the yarn to the xyz–coordinates. $[\tilde{Q}^Y]$ is derived from the in–plane elastic constants of each ply with undulated yarns as:

$$[\tilde{Q}^Y] = \left[\begin{array}{ccc} Q_{11} & Q_{12} & 0 \\ Q_{21} & Q_{22} & 0 \\ 0 & 0 & Q_{66} \end{array} \right] = \left[\begin{array}{ccc} \frac{E_1}{1-\nu_{12}\nu_{21}} & \frac{\nu_{12}E_2}{1-\nu_{12}\nu_{21}} & 0 \\ \frac{\nu_{21}E_1}{1-\nu_{12}\nu_{21}} & \frac{E_2}{1-\nu_{12}\nu_{21}} & 0 \\ 0 & 0 & G_{12} \end{array} \right], \tag{4.27}$$

Here, E is the modulus, G is the shear modulus and ν is the Poisson's ratio.

However, the yarns are undulated in the basic elements. The in–plane elastic contribution of the yarns are a function of the local yarn angle ϱ in each basic element e, which is the first derivative of the yarn mid–line functions:

$$\begin{aligned} \varrho(x)^e &= \arctan\left(\frac{\partial m(x)^e}{\partial x}\right) \\ \varrho(y)^e &= \arctan\left(\frac{\partial m(y)^e}{\partial y}\right) \end{aligned} . \tag{4.28}$$

The effective in–plane elastic constants of the warp and fill yarns can be described using the undulation angles $\varrho(x)^e$ and $\varrho(y)^e$ of these yarns as [25]:

$$\begin{aligned} E_1(\varrho) &= \left[\frac{\cos^4\varrho}{E_l} + (\frac{1}{G_{lt}} - \frac{2\nu_{lt}}{E_l})\cos^2\varrho\sin^2\varrho + \frac{\sin^4\varrho}{E_t}\right]^{-1} \\ E_2(\varrho) &= E_t \\ \nu_{12}(\varrho) &= E_1(\varrho)\left[\frac{\cos^2\varrho\,\nu_{lt}}{E_l} + \frac{\sin^2\varrho\,\nu_{tt}}{E_t}\right] \\ G_{12}(\varrho) &= \left[\frac{\cos^2\varrho}{G_{lt}} + \frac{\sin^2\varrho}{G_{tt}}\right]^{-1} \end{aligned} , \tag{4.29}$$

Here, the suffix l and t represent longitudinal and transverse direction respectively.

Accounting for the boundaries of the shape functions, substituting these into equation (4.24), and subsequent integration for each of the areas, results in:

$$\begin{aligned} A^e_{ij}(x,y) &= Q^R_{ij}\left[h_T^{We}(x,y) - h_T(x,y) + h_B(x,y) - h_B^{Fe}(x,y)\right] + \\ &\quad Q^W_{ij}(\varrho(x)^e)\left[h_B^{We}(x,y) - h_T^{We}(x,y)\right] + \\ &\quad Q^F_{ij}(\varrho(y)^e)\left[h_B^{Fe}(x,y) - h_T^{Fe}(x,y)\right] \qquad (4.30a) \\ B^e_{ij}(x,y) &= \tfrac{1}{2}Q^R_{ij}\left[h_T^{We}(x,y)^2 - h_T(x,y)^2 + h_B(x,y)^2 - h_B^{Fe}(x,y)^2\right] + \\ &\quad \tfrac{1}{2}Q^W_{ij}(\varrho(x)^e)\left[h_B^{We}(x,y)^2 - h_T^{We}(x,y)^2\right] + \\ &\quad \tfrac{1}{2}Q^F_{ij}(\varrho(y)^e)\left[h_B^{Fe}(x,y)^2 - h_T^{Fe}(x,y)^2\right] \qquad (4.30b) \\ D^e_{ij}(x,y) &= \tfrac{1}{3}Q^R_{ij}\left[h_T^{We}(x,y)^3 - h_T(x,y)^3 + h_B(x,y)^3 - h_B^{Fe}(x,y)^3\right] + \\ &\quad \tfrac{1}{3}Q^W_{ij}(\varrho(x)^e)\left[h_B^{We}(x,y)^3 - h_T^{We}(x,y)^3\right] + \\ &\quad \tfrac{1}{3}Q^F_{ij}(\varrho(y)^e)\left[h_B^{Fe}(x,y)^3 - h_T^{Fe}(x,y)^3\right], \qquad (4.30c) \end{aligned}$$

where the subscript R, W and F denote resin, warp and fill, respectively, and superscript e denotes the type of basic element (A, B, C or D). $[Q^R]$ is derived by substituting the resin modulus, Poisson's ratio and shear modulus into 4.27.

The average CLT stiffness matrices for each basic element can now be obtained using the two–dimensional woven fabric model [49, 50]. The model can predict an upper and lower boundary for the CLT stiffness matrices by assuming in–plane iso–strain or iso–stress conditions, respectively called the *Parallel-Parallel* (PP) and the *Series-Series* (SS). The upper boundary is predicted by:

$$\left(\overline{A}^{e,PP}_{ij}, \overline{B}^{e,PP}_{ij}, \overline{D}^{e,PP}_{ij}\right) = \frac{1}{l^W_t l^F_t}\int_0^{l^F_t}\int_0^{l^W_t}\left(A^e_{ij},\, B^e_{ij},\, D^e_{ij}\right)dxdy \tag{4.31}$$

The $[abhd]^{e,PP}$ compliance matrix can be obtained by substituting $[\overline{A}]^{e,PP}$, $[\overline{B}]^{e,PP}$ and $[\overline{D}]^{e,PP}$ in the CLT constitutive equation (4.23) and inverting the resulting $[ABD]^{e,PP}$ stiffness matrix. $[h]$ equals $[b]^T$ in the $[abhd]$ matrix. The lower boundary for the stiffness is obtained via the compliance matrix form:

$$\left(\overline{a}_{ij}^{e,SS}, \overline{b}_{ij}^{e,SS}, \overline{d}_{ij}^{e,SS}\right) = \frac{1}{l_t^W l_t^F} \int_0^{l_t^F} \int_0^{l_t^W} \left(a_{ij}^e,\, b_{ij}^e,\, d_{ij}^e\right) dxdy. \tag{4.32}$$

The $[ABD]^{e,SS}$ stiffness matrix is obtained by inverting $[abhd]^{e,SS}$. The integrals from equations 4.31 and 4.32 are evaluated numerically using Gauss–Legendre quadrature [3].

Thermal properties

The thermal properties of the basic elements are determined under the same assumptions as the mechanical properties of the basic elements. The equations for the thermal forces then become:

$$\left\{ \begin{array}{c} \tilde{N}_i^e \\ \tilde{M}_i^e \end{array} \right\} = -\Delta T \left\{ \begin{array}{c} \overline{N}_i^e \\ \overline{M}_i^e \end{array} \right\}, \tag{4.33}$$

in which

$$\overline{N}_i^e = \int_{h_B}^{h_T} q_i^e(x,y)\, dz, \qquad \overline{M}_i^e = \int_{h_B}^{h_T} q_i^e(x,y)\, z\, dz, \tag{4.34}$$

and

$$q(x,y)_i^e = Q_{ij}^e(x,y)\, \alpha_j(x,y). \tag{4.35}$$

Here, $\{\alpha(x,y)\}$ contains the thermal expansion coefficients with respect to the xyz–coordinate system of the warp or fill yarn or the matrix material. $\{\alpha(x,y)\}$ is obtained by in–plane rotation of $\{\alpha^{123}\}$, similarly to the rotation of the in–plane stiffness matrix, it reads:

$$\{\alpha(x,y)\} = [R] \cdot [T]^{-1} \cdot [R]^{-1} \{\alpha^{123}\}, \tag{4.36}$$

where

$$\begin{array}{l} \alpha_1^{123} = \alpha_l \cos^2 \varrho + \alpha_t \sin^2 \varrho \\ \alpha_2^{123} = \alpha_t \\ \alpha_{12}^{123} = 0 \end{array} \quad , \tag{4.37}$$

where α_l and α_t are the thermal expansion coefficients in the longitudinal and transverse direction of the yarn respectively. The thermal expansion coefficients of the warp and fill yarn depend on the fibre volume fraction and are determined using the rule–of–mixtures model and the model of Schapery [62].

The thermally induced forces and moments are determined by substituting Q_{ij} by q_i in part a and b of equation (4.30) respectively. When assuming no external force the resulting thermal strain and curvature for the basic elements are:

$$\left\{ \begin{array}{c} \tilde{\varepsilon}^{o,e} \\ \tilde{\kappa}^e \end{array} \right\} = -\Delta T \left[\begin{array}{cc} \overline{a}^e & \overline{b}^e \\ \overline{h}^e & \overline{d}^e \end{array} \right] \cdot \left\{ \begin{array}{c} \overline{N}^e \\ \overline{M}^e \end{array} \right\}. \tag{4.38}$$

A lower and upper boundary can also be predicted for the thermal strain and curvature. They are determined by substituting the $[abhd]$ compliance matrix following from an iso–strain or iso–stress configuration into equation (4.38). The in–plane thermal strain and curvature coefficients per °C $\{\overline{\varepsilon}^o\}^e$ and $\{\overline{\kappa}\}^e$ are:

$$\left\{ \begin{array}{c} \overline{\varepsilon}^{o,e} \\ \overline{\kappa}^e \end{array} \right\} = \left[\begin{array}{cc} \overline{a}^e & \overline{b}^e \\ \overline{h}^e & \overline{d}^e \end{array} \right] \cdot \left\{ \begin{array}{c} \overline{N}^e \\ \overline{M}^e \end{array} \right\}. \tag{4.39}$$

4.4.3 Meso level thermo–elastic modelling

The unit cell properties are determined in the meso level using the basic elements properties of section 4.4.2. Two approaches are distinguished here, the averaging approach and the Finite Element (FE) approach.

Averaging approach

The thermo–elastic properties of the weave are determined by volume averaging of the properties of all basic elements in the RVE. A lower and an upper bound of the basic element properties were obtained, using an iso–strain and iso–stress configuration respectively. Similar assumptions can be applied for the averaging approach, resulting in four possible combinations. Two combinations are based on an iso–strain assumption in the RVE, the other two assume an iso–stress in the RVE. However, the assumption of iso–stress leads to an severe underestimation of the stiffness properties of the fabric weave and is therefore not used in this analysis.

All basic elements have an equal volume. As a result, the average thermo–elastic properties of the RVE are determined by:

$$\begin{aligned} [A]^R &= \frac{1}{m_t}\left(m_a\overline{[A]}^a + m_b\overline{[A]}^b + m_c\overline{[A]}^c + m_d\overline{[A]}^d\right) \\ [B]^R &= \frac{1}{m_t}\left(m_a\overline{[B]}^a + m_b\overline{[B]}^b + m_c\overline{[B]}^c + m_d\overline{[B]}^d\right), \\ [D]^R &= \frac{1}{m_t}\left(m_a\overline{[D]}^a + m_b\overline{[D]}^b + m_c\overline{[D]}^c + m_d\overline{[D]}^d\right) \end{aligned} \tag{4.40}$$

where m represents the number of basic elements. The subscript t indicates total and a, b, c and d stand for the type of basic element. The RVE's lower and upper stiffness bound can be determined by averaging the basic element PP or SS configuration, respectively.

The thermal loading vector is derived similarly to the CLT stiffness matrices. The volume averaged thermal loading vectors read:

$$\begin{aligned} \{\tilde{N}\}^R &= \frac{1}{m_t}\left(m_a\{\tilde{N}\}^a + m_b\{\tilde{N}\}^b + m_c\{\tilde{N}\}^c + m_d\{\tilde{N}\}^d\right) \\ \{\tilde{M}\}^R &= \frac{1}{m_t}\left(m_a\{\tilde{M}\}^a + m_b\{\tilde{M}\}^b + m_c\{\tilde{M}\}^c + m_d\{\tilde{M}\}^d\right) \end{aligned}. \tag{4.41}$$

Finite Elements approach

An FE approach can be used, alternatively to the averaging approach, leading to closer bounds for the unit cell stiffness.

Equations (4.19) and (4.20) are substituted in the equation of virtual work, containing the volume integral of the element stiffnesses and displacements and the surface integral of the applied forces:

$$\delta\Pi = \int_A \int_h \{\delta\varepsilon^o + z\delta\kappa\}^T \cdot \{[Q] \cdot \{\varepsilon^o + z\kappa\}\} dz dA - \int_\Gamma \delta v \cdot t \, d\Gamma \equiv 0 \quad (\forall \delta\varepsilon, \delta\kappa), \quad (4.42)$$

Here, A is the area, h is the thickness, $\delta\varepsilon^o$ and $\delta\kappa$ are the virtual strains and curvatures, δv the virtual displacements and rotations, t the tractions and Γ is the boundary. The body forces are assumed to be zero. The FE representation then uses:

$$\begin{aligned} \{\delta\varepsilon^o\} &= [B_m] \cdot \{\delta u\}, \quad \{\varepsilon^o\} = [B_m] \cdot \{u\} \\ \{\delta\kappa\} &= [B_b] \cdot \{\delta\phi\}, \quad \{\kappa\} = [B_b] \cdot \{\varphi\} \end{aligned} \quad (4.43)$$

where B_m and B_b contain the first derivatives of the FE trial functions of, respectively, the element displacements, $\{u\}$, and rotations, $\{\varphi\}$. The virtual displacements and rotations are denoted by $\{\delta u\}$ and $\{\delta\varphi\}$, respectively. Thus, an FE formulation is found, symbolically written as:

$$\int_A \begin{bmatrix} B_m & 0 \\ 0 & B_b \end{bmatrix}^T \cdot \begin{bmatrix} A & B \\ B^T & D \end{bmatrix} \cdot \begin{bmatrix} B_m & 0 \\ 0 & B_b \end{bmatrix} dA \cdot \begin{Bmatrix} u \\ \varphi \end{Bmatrix} = \{F\}, \quad (4.44)$$

where $\{F\}$ contains the prescribed nodal forces.

The Discrete Kirchhoff Triangle (DKT) element with three in–plane integration points is used to solve the FE problem [5, 13]. Each basic element is represented by four finite elements. The thermo–elastic basic element properties, derived in section 4.4.2, are used in each of the FE elements. The plain weave RVE is described with 4×4 basic elements, resulting in a mesh of 64 elements. The 8H satin weave is computationally less attractive. The RVE of an 8H satin weave is described with 16×16 of these quadrilaterals, resulting in a mesh of 1024 elements. The FE mesh for a basic element is depicted in figure 4.10.

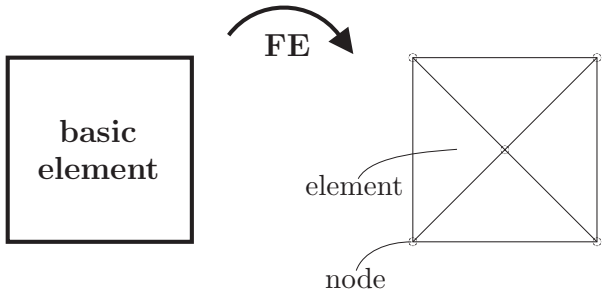

Figure 4.10: Representation of a basic element by four FE elements.

Elementary loading conditions are applied to the FE mesh, resulting in deformations of the FE mesh. Six loading and corresponding deformation sets are required to filter the mechanical properties of the RVE. The RVE is based on periodicity in the weave. Therefore, periodicity must also be preserved in the deformed RVE. Constraint equations on the sides of the RVE are used to guarantee the periodicity.

To this end, a linear relation is prescribed between the difference in nodal displacements and rotations of the opposite RVE sides and the nodal displacements and rotations of the RVE corner nodes. The actual constraint equations can be explained using figure 4.11.

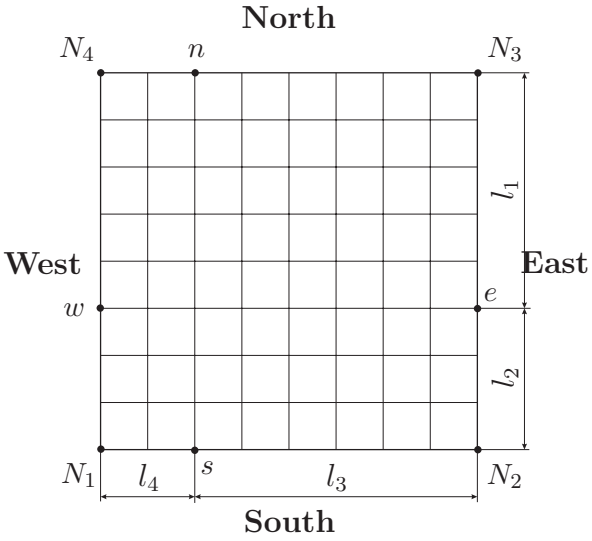

Figure 4.11: Constraints on the sides of the RVE.

All degrees of freedom U_e and U_w, *i.e.* all separate nodal displacements u and rotations φ, of two opposite nodes e and w at the east and west side respectively, of the RVE are constrained by:

$$\begin{aligned} U_e - U_w &= \frac{l_2}{l_1 + l_2}\Delta U_N - \frac{l_1}{l_1 + l_2}\Delta U_S \\ \Delta U_N &= U_4 - U_3 \\ \Delta U_S &= U_2 - U_1 \end{aligned} \tag{4.45}$$

in which the subscripts N, S, E and W refer to North, South, East and West, respectively. The subscript 1, 2, 3 and 4 indicate the corner nodes of the RVE. For the north and south side the constraints are similar:

$$\begin{aligned} U_n - U_s &= \frac{l_4}{l_3 + l_4}\Delta U_E - \frac{l_3}{l_3 + l_4}\Delta U_W \\ \Delta U_E &= U_3 - U_2 \\ \Delta U_W &= U_4 - U_1 \end{aligned} \tag{4.46}$$

The deformations within the RVE can deviate from the overall deformations. Six degrees of freedom must be suppressed in order to prevent rigid body displacements or rotations of the RVE. Now, any constant stress gradient field can be described by only applying loads on the corner nodes of the FE model.

Forces and moments are applied at the four corner nodes of the RVE to create six elementary load cases. The three in–plane loadcases are: tension in the global x–direction, tension in the y–direction and simple shear in the xy–direction. The three out–of–plane loading conditions are: bending in the global y–direction, bending in the global x–direction and pure twist in the global xy–direction.

The displacements and the reaction forces of the four corner nodes are used to determine the stress and strain state, which are related by the [*abhd*] compliance matrix. The components of this compliance matrix can be determined directly from the six elementary loadcases.

The thermal properties of the woven fabric composite are determined by pre–stressing the basic elements with the thermally induced element forces and moments from equation (4.33). The FE model (again subjected to the condition of periodicity) then gives the resulting nodal displacements and rotations of the four corner nodes. These, in turn, lead to the thermal expansion and bending coefficients of the corresponding continuum.

4.4.4 Macro level thermo–elastic modelling

The homogenised RVE properties of the fabric are determined in section 4.4.3. These CLT based properties are relative to the mid–plane of the ply. Stacking of the individual plies results in an offset of each ply to the mid–plane of the composite. This offset has to be accounted for since it affects the CLT properties. The following exercise is performed to derive expressions to account for the offset.

Deriving an expression for the offset

The contribution of the individual layers to the composite properties can be derived from the definitions of $[A]$, $[B]$ and $[D]$ in equation (4.24). Evaluating equation (4.24) as a ply with homogeneous properties result in:

$$\begin{aligned} [A] &= (h_T - h_B)[Q] \\ [B] &= \tfrac{1}{2}({h_T}^2 - {h_B}^2)[Q] \\ [D] &= \tfrac{1}{3}(h_T^{k\,3} - h_B^{k\,3})[Q] \end{aligned} \tag{4.47}$$

Adding an offset h_o to the height coordinates of the ply h_T and h_B, and substituting these limits in equation (4.24) followed by integration over the height coordinate results in:

$$\begin{aligned} [A]^o &= (h_T - h_B)[Q] = [A] \\ [B]^o &= h_o(h_T - h_B)[Q] + \tfrac{1}{2}({h_T}^2 - {h_B}^2)[Q] = h_o[A] + [B] \\ [D]^o &= {h_o}^2(h_T - h_B)[Q] + h_o({h_T}^2 - {h_B}^2)[Q] + \tfrac{1}{3}({h_T}^3 - {h_B}^3)[Q]' \\ &= {h_o}^2[A] + 2h_o[B] + [D] \end{aligned} \tag{4.48}$$

where $[A]^o$, $[B]^o$ and $[D]^o$ account for the offset h_o. Similarly, expressions for the loading vectors $\{N\}^o$ and $\{M\}^o$ can be derived. It involves the integration of $\{\sigma(z)\}$ over the height coordinate.

Macro level contribution of the plies

The distance between the centre of the composite and the centre of the individual fabric layer is denoted with h_o^k, where k is the ply index. The properties of the individual fabric layer are defined in the xy–coordinate system. However, the individual plies are orientated off–axis in the composite. Rotation of the plies by substituting $[A]^R$, $[B]^R$,

$[D]^R$ for $[Q]$ in equation 4.25 accounts for the ply orientation. The contribution of each individual layer to the composite properties is:

$$\begin{aligned}
[A]^C &= \sum_{k=1}^{m} [A]^{R,k} \\
[B]^C &= \sum_{k=1}^{m} \left(h_o^k [A]^{R,k} + [B]^{R,k} \right) \\
[D]^C &= \sum_{k=1}^{m} \left(h_o^{k^2} [A]^{R,k} + 2h_o^k [B]^{R,k} + [D]^{R,k} \right)
\end{aligned} \tag{4.49}$$

where the superscript C denotes composite, the superscript R indicates RVE and m is the number of fabric layers in the composite. The thermal properties of the composite are derived similarly to those of the individual layers. Rotation of $\{\tilde{N}\}^R$ and $\{\tilde{M}\}^R$ accounts for the ply orientation. The composite thermal loading vectors $\{\tilde{N}\}^C$ and $\{\tilde{M}\}^C$ are described as:

$$\begin{aligned}
\{\tilde{N}\}^C &= \sum_{k=1}^{m} \{\tilde{N}\}^{R,k} \\
\{\tilde{M}\}^C &= \sum_{k=1}^{m} \left(h_o^k \{\tilde{N}\}^{R,k} + \{\tilde{M}\}^{R,k} \right)
\end{aligned} \tag{4.50}$$

4.5 Woven fabric model verification

The thermo–elastic properties of fibre reinforced thermoplastic composites were measured in order to validate the model. Symmetric laminates were manufactured from glass fibre reinforced poly(phenylene sulphide) (PPS) 8H satin weave (Ten Cate Cetex© SS303). All specimens were made by compression moulding, using a Fontijne plate press. The fibre volume fraction in the orthogonal fabric composites was approximately 50%. It was determined prior to compression moulding from the mass fractions of the constituents. The manufacturing technique used for producing the skewed specimens resulted in an increase of the volume fraction with increasing skew angle.

4.5.1 Mechanical testing

Tensile tests were performed using a Zwick type 1445 machine with a 10 kN load cell. Four layered symmetrically builtup specimens with orthogonal weaves, skewed weaves and orthogonal weaves with a Quasi Isotropic (QI) lay–up were tested. The specimens were prepared according to the ASTM D3039–76 protocol [2]. The dimensions of the specimens were 25 mm wide and 250 mm long. The thickness of the specimens was approximately 0.9 mm but varied due the skew angle of the laminates.

The skewed weave specimens were manufactured by placing a dry weave into a shear frame, similar to the picture frame. The areal density of the skewed weave increases since the area of the skewed weave is smaller than the area of the orthogonal weave. A layer of resin foil was placed between the fabric layers. The skewed samples were subsequently moulded in the plate press. The skew angles of the fabric were set at 10°, 20° and 30°. The fibre volume fraction of the skewed specimens is higher than the fibre volume

fraction of the orthogonal specimens since the same foil is used for manufacturing. The fibre volume fraction is determined by the following relation:

$$V_{f_s} = \frac{V_f}{(1 - \sin 2\phi)V_f + \sin 2\phi} \tag{4.51}$$

The specimens with orthogonal weaves were tested in the 0°, 45° and 90° direction with respect to the major principal axis of the material. The specimens with skewed weaves were measured in their bias directions, as depicted in figure 4.12.

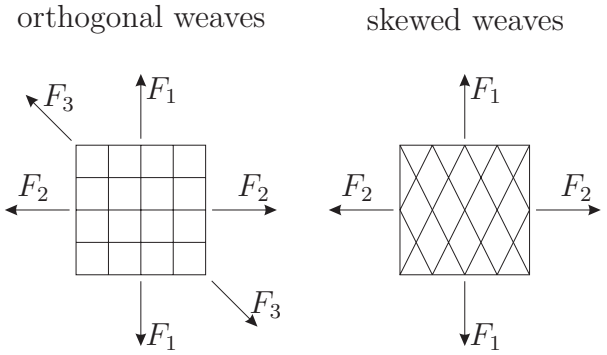

Figure 4.12: Loading directions for the orthogonal and skewed specimens.

The QI specimens were tested in one direction. The load was directly obtained from the tensile testing machine, while the strain was measured using a clip–on extensiometer. Five tests were performed per type of specimen. The velocity of the tensile testing rig was 1 mm/min. The tests were performed at room temperature. The results will be presented in section 4.6, showing a_{11}, the first component of the $[abhd]$ compliance matrix.

4.5.2 Thermal testing

The thermal expansion coefficients of the material were measured in a Thermal Mechanical Analysis (TMA) machine. Basically, the TMA consists of two parts: a high–precision temperature controlled oven, and an accurate displacement measurement device. The test set–up in the TMA is given in figure 4.13.

The specimen is placed between the probe and the support. Both the probe and the support are made from quarts, a material with a very low thermal expansion. The probe moves vertically and is connected to a Linear Variable Differential Transformer. The whole set–up is placed into a temperature controlled oven and the vertical displacement of the probe is measured as a function of the temperature. The probe loads the specimen with 0.1 N to ensure contact during the measurement. The linear thermal expansion is acquired from the temperature versus displacement curve when the initial thickness is measured.

The symmetrically builtup sixteen layer specimens with a dimension of $29.5 \times 9 \times 4$ mm^3 were placed vertically onto the support of the TMA. The samples were dried in a vacuum oven for 3 weeks at a temperature of 50 °C prior to testing to eliminate moisture–induced expansion. The thermal cycle, to which the specimen was subjected, is shown in figure 4.14.

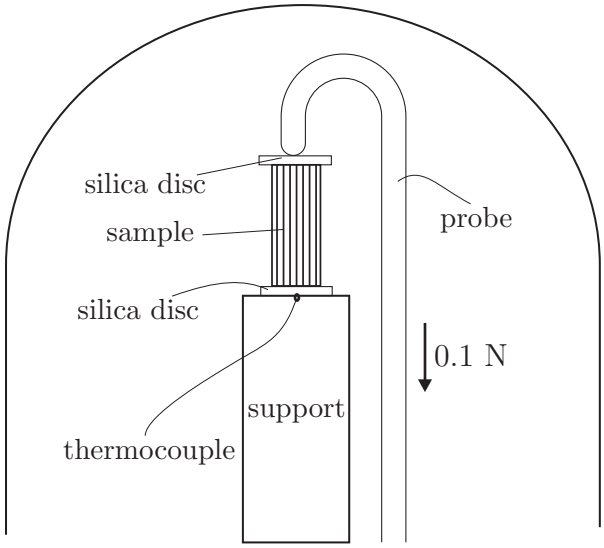

Figure 4.13: Set–up in TMA for measuring thermal expansion.

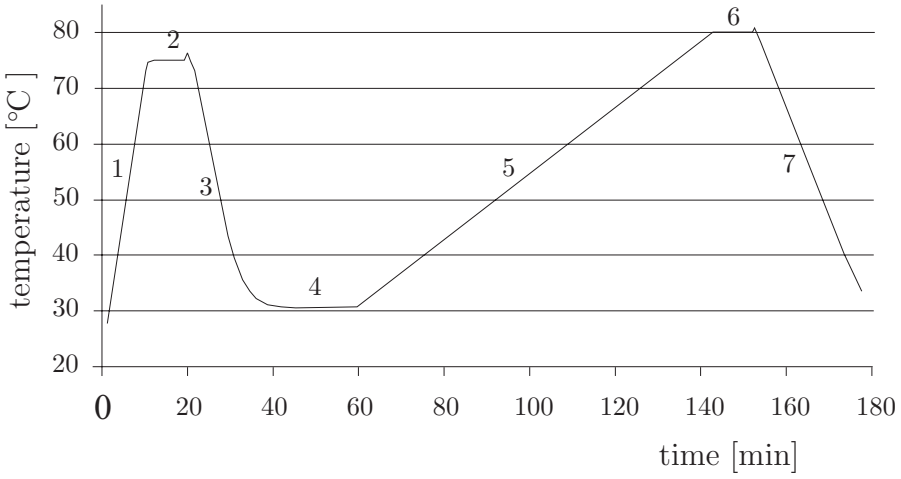

Figure 4.14: Thermal profile of TMA for measuring thermal expansion.

The TMA cycle program contains seven parts. The first three parts make up one dummy temperature cycle, resulting in less deviation between the individual experimental results. The ramp–up for measuring the thermal expansion was set slow enough to ensure a homogeneous temperature distribution within the specimen. The results of the thermal expansion measurements will be presented in section 4.6.

4.6 Results and discussion

Some input parameters are required for modelling the thermo–elastic properties of the weaves. The properties for the 8H satin and the plain weave are obtained from the datasheet from the manufacturer and listed in table 4.2.
The PPS resin material properties are supplied by the manufacturer [42]. The properties

Table 4.2: Properties of the modelled weaves

property		8H satin	Plain
warp count	1/m	2280	960
fill count	1/m	2200	1050
areal density	kg/m^2	0.3	0.3

of the isotropic E–glass fibres is obtained from literature [54]. An overview of the material input parameters is given in table 4.3.

Table 4.3: Properties of the constituents in the composite

property		E-glass	PPS
Young's modulus	GPa	72.4	3.7
Poisson's ratio	-	0.23	0.37
lin. thermal expansion	1/K	5E-6	51E-6
density	kg/m^3	2540	1350

The height of the fabric h_f, the width of the yarns l_{fx} and l_{fy} and the undulated lengths of the yarns U_x and U_y were determined with microscopy investigations of the weaves.

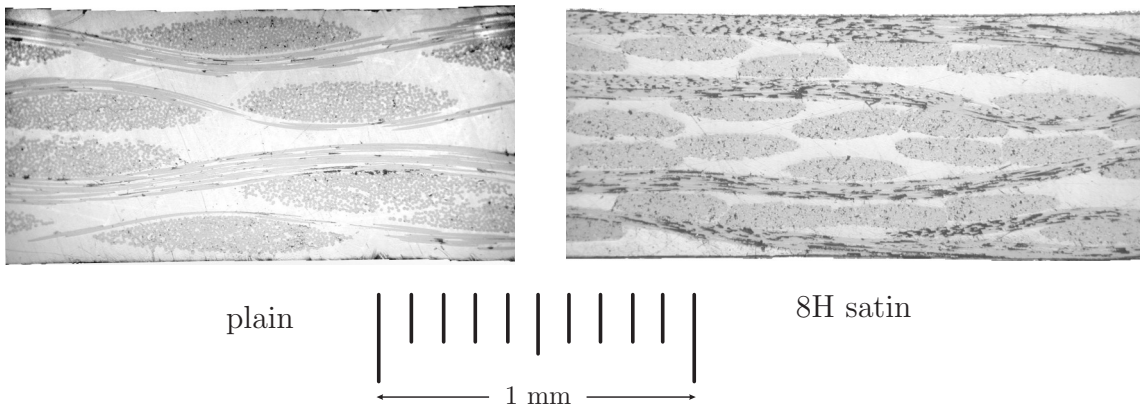

Figure 4.15: micrographs of the cross–section of a four layered orthogonal plain weave and 8H satin weave.

The yarn shape in the plain weave can be fitted with an ellipsoid shape. Most yarn shapes in the cross–section of the plain weave are similar, see figure 4.15. Little nesting occurred in this weave. However, the yarn shape in the 8H satin weave cross–section are quite dissimilar. Extreme differences in the shape of the yarn, yarn height and width are observed. Nesting of the individual plies is clearly visible in these micrographs.

Optical measurements of the yarns cross–section resulted in the additional parameters. The results are expressed in percentages of the total ply height h_t and total width of the yarns l_x, l_y. The experimental error in these additional parameters is significant.

Table 4.4: Additional parameters for the woven fabric model.

weave	h_f	l_{fx}	l_{fy}	U_x	U_y
plain	95	85	85	100	100
8H satin	97	90	90	60	60

4.6.1 Mechanical

The experimental results and the modelled results for the unskewed specimens are shown in figure 4.16. The results are presented in the a_{11} compliance form. A higher a_{11} value indicates a weaker material response.

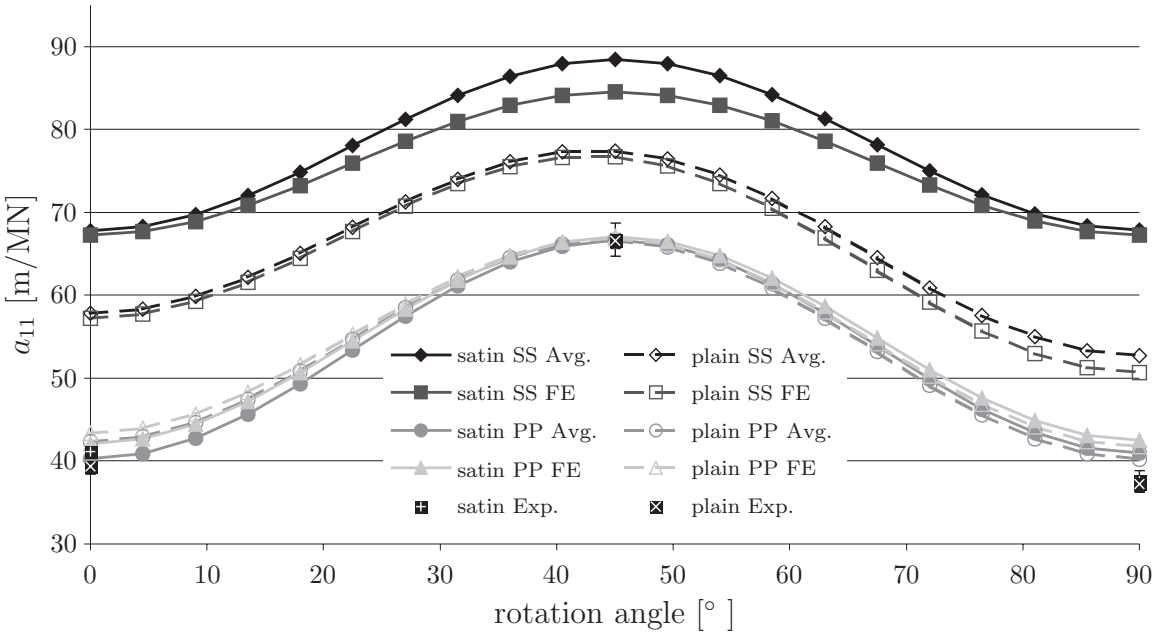

Figure 4.16: Modelled and experimental values for the a_{11} compliance property of 8H satin and plain weave composites. The enclosed fibre angle of the 4 layered orthogonal composites is denoted in the legend.

The laminate is rotated over an angle of 90 ° in the model, illustrating the effect of rotation on the a_{11} properties. Four types of models were used for each weave: the *SS* and *PP* configuration in the averaging approach and the *SS* and *PP* configuration in the FE approach. Tensile tests were performed in the fibre directions (0° and 90 °) and the bias direction (45 °).

The measured a_{11} values is not affected significantly by the weave type. In the fibre directions the *PP* configurations predict these values nicely. The *SS* configurations overestimate the a_{11} values significantly.

A small change in the measured, and modelled, values is determined at the 0° and 90° axis. Since both weaves are not completely regular, a small difference is observed in the 0° and 90° values. Equal results are expected if the weaves are completely regular.

The *PP* or the *SS* configuration predict different results for the plain weave. A difference of approximately 25% is observed between these configurations. The effect of the approach is small; the averaging approach and the FE approach predict nearly the

same values in case of the plain weave for the *PP* configuration or the *SS* configuration. This is caused by the homogeneity of the plain weave. Plain weaves consist of *A*–type basic elements only. The strain and stress fields in the FE approach are therefore nearly homogeneous, resulting in similar predictions as the averaging approach.

The results for the satin weave are affected significantly by the *PP* and the *SS* configuration. The difference in the results for the averaging approach is approximately 40% for this weave. The averaging and the FE approach slightly affect the predicted results for the satin 8H weave. The results from the *PP* and *SS* configuration for the averaging approach were further apart for this weave than for the plain weave. This is caused by the less homogeneous basic element distribution of the satin weave; it consists of all basic element types, resulting in a less homogeneous strain and stress field in the FE approach.

The effects of skew deformation on the thermo–elastic properties are shown by performing tensile tests in the bias directions. The results for the plain weave tests are depicted in figure 4.17.

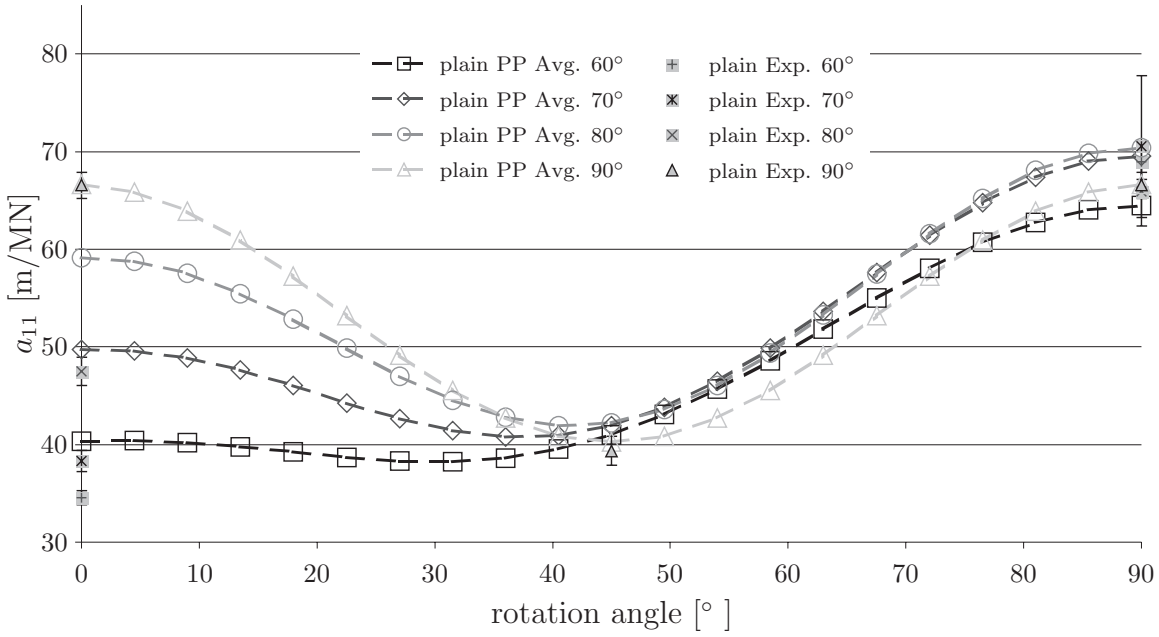

Figure 4.17: Modelled and experimental values for the a_{11} compliance property of plain weave composites. The enclosed fibre angle of the 4 layered skewed composites is denoted in the legend.

The measured a_{11} values and the predicted results for the *PP* configuration with the averaging approach are shown in figure 4.17. Again, a_{11} is presented as a function of the rotated angle of the complete laminate. The a_{11} properties of skewed plain weave are affected by the enclosed fibre angle of the weave. A smaller angle results in a significantly lower a_{11} value for the material, *i.e.* the material behaves stiffer. The model overestimates the measured values when the enclosed fibre angle is small. No explanation is found for the overestimation and further investigation of this topic is recommended.

The results for the QI-lay–up laminates are shown in figure 4.18. The model overestimates the experimental values. Again, the best predictions are obtained with

the *PP* configuration with the averaging approach. The experimental plain weave a_{11} property is smaller than those of the 8H satin weave.

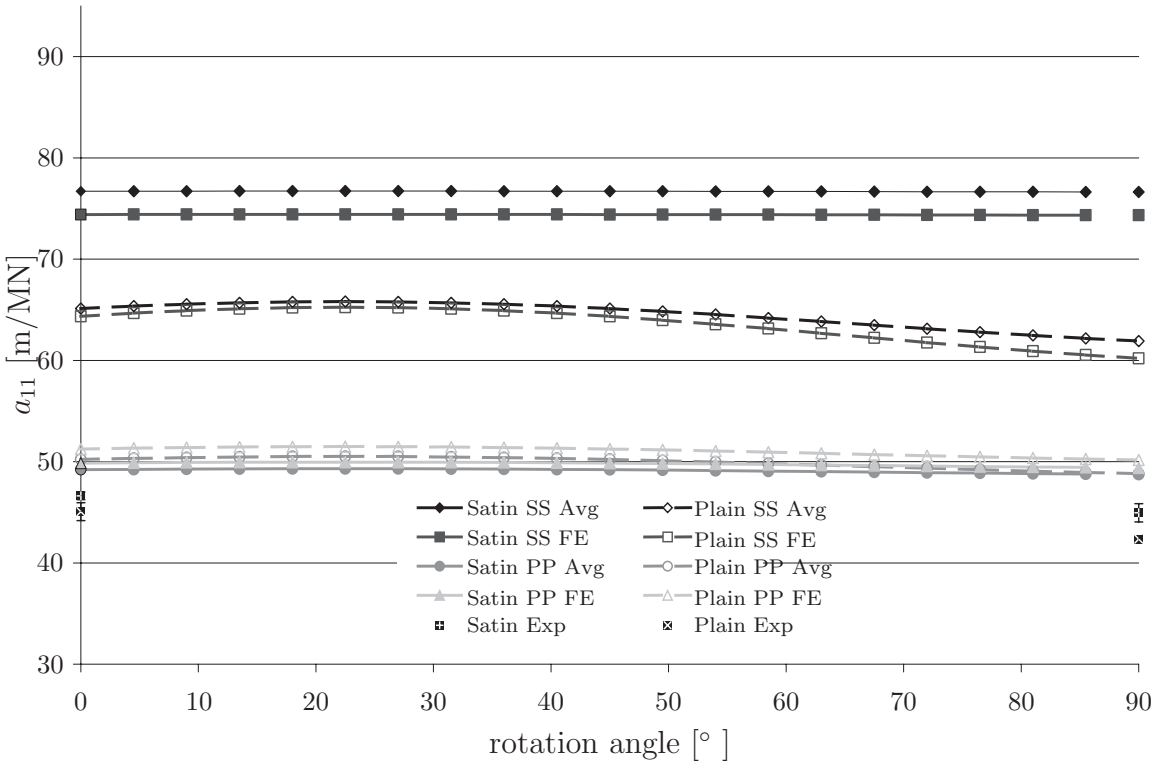

Figure 4.18: a_{11} property of 8H satin and plain weave 4 layered QI composites.

The averaging approach predicts the properties more quickly than the FE approach since it does not require to solve the nodal degrees of freedom of the FE mesh. The computing time of the FE approach grows with the size of the unit cell.

The resin material is assumed to be linearly elastic in this analysis. The resin material has however visco–elastic properties. The effect of visco–elasticity on the composite behaviour requires further investigation.

4.6.2 Thermal

The modelled values of the thermal expansion for the unskewed specimens are compared with the measured thermal expansion in figure 4.19. The thermal expansion was modelled for plain weaves using the averaging approach. A small difference between the measured, and modelled, values is found at the 0° and 90° axis for the in–plane thermal expansion. This difference is caused by the irregularity of the plain weave.

Good agreement between the experimental values and the modelled results is obtained for the orthogonal laminates in both the 0° and the 90° direction. The *SS* configuration overestimates the experimental values in both cases. The better predictions are obtained with the *PP* configuration.

The models predict the coefficients of thermal expansion for QI laminates less well. Both modelled values are outside the experimental error values. Again, the *PP* configuration predicts the experimental values significantly better.

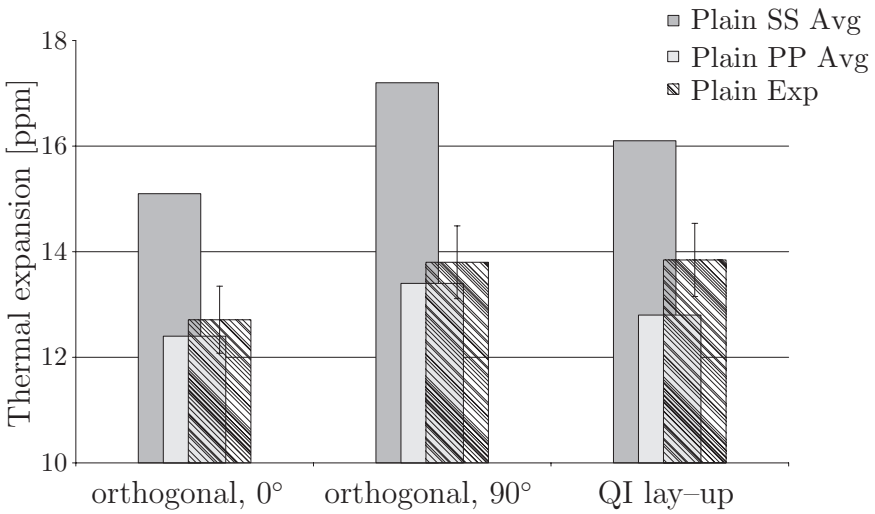

Figure 4.19: Thermal expansion for an orthogonal plain weave composites and a QI builtup composite.

The affect of skew deformation on the thermal expansion of plain weaves was not experimentally determined. The in–plane thermal expansion of the 8H satin weaves was also not measured. Experiments to validate the model for both weaves is recommended.

4.7 Conclusion

A model was presented to determine the in–plane thermo–elastic properties of woven fabric laminates. It provides a good correlation with the experimental results for a plain weave and an 8H satin weave when a uniform state of basic element strain is used (upper bound for the stiffness). In case a uniform state of basic element stress is assumed (lower bound for the stiffness), the laminate stiffness is underestimated.

The bounds for the iso–strain and iso–stress are quite far apart. The difference between the predictions of uniform strain and stress models can be reduced by using an finite element approach. However, applying this FE approach does not increase the accuracy of the model.

The model shows good agreement for the prediction of the thermal expansion of orthogonal weaves in the fibre direction. The thermal expansion of QI laminates is less well predicted but acceptable. As with the elastic properties, the iso–strain configuration predicts the experimental values best.

4.8 Recommendations

A few recommendations are suggested for the model to predict the thermo–elastic properties of laminates builtup from non–orthogonal weaves.

The presented model is only validated for in–plane tensile tests and thermal expansion measurements. However, the model presented here predicts the complete ABD stiffness matrix and the thermal expansion–curvature vector. This stiffness matrix includes bending stiffness, represented by the D–matrix and the tension bending coupling, which is accounted for by the B–matrix. Bending tests are recommended in order to validate

the predicted D–matrix by model. It is also recommended to extend the validation of the thermal expansion–curvature vector.

The RVE is idealised by a combination of basic elements. The yarn's cross–section, undulation and other geometrically derived properties are defined in these basic elements. Microscopic investigations revealed large differences between the individual yarn geometries. Nesting was also observed in these micrographs. It is recommended to investigate the effect of these differences.

The unidirectional properties of the yarns are predicted by micromechanical models. A large variety of micromechanical models is available in literature. The individual models predict differences up to 100%, especially in the transverse direction. The properties of the yarns, with a high volume fraction, are not experimentally determined and the micromechanical model is therefore not verified. Further work is this area is recommended.

Chapter 5

Thermo–elastic properties of doubly curved products

The thermo–elastic properties of the composite need to be included in the model to predict processing–induced shape distortions of the product. The distortions can be introduced by for example, thermal loading or stresses induced by forming. Obviously, the materials used and the lay–up of the composite affect the thermo–elastic properties. However, the thermo–elastic properties of the composite change locally, as a function of the fibre orientation, due to processing–induced fibre re–arrangement. This fibre orientation and resulting local composite properties need to be accounted for in the model.

Chapter 3 addressed the Finite Element (FE) modelling of the draping process of doubly curved products. The fibre reorientation of single layer and multi–layered composites was predicted incorporating the resulting fibre stresses.

In chapter 4, a method has been presented to predict the local composite properties of laminates builtup from non–orthogonal weaves. The method predicts the in–plane properties of flat laminates, based in a Classical Laminate Theory (CLT) approach.

The objective here is to model the shape distortions using a FE method with computationally effective plate elements. Combining the results from draping with the local thermo–elastic properties of fabric reinforced composites results in a prediction for the processing–induced distortions of double curved products.

Two examples demonstrate the shape distortions due to forming induced fibre reorientation. First, the shape distortions of the double dome geometry, presented in chapter 3, are presented. Secondly the shape distortions of a woven fabric reinforced thermoplastic composite hemisphere are modelled. The hemisphere is a frequently used shape for verification of drape modelling.

5.1 Review

Hsiao and Kikuchi [29] modelled the thermo–forming process of thermoplastic composites in 1999. They account for fibre reorientation during forming and the evolution of the microstructure of the fabric weave in the non–isothermal simulation, based on single layer fabric composites. The fibre reorientation was modelled with a power–law constitutive model [59]. The cooling stage was simulated with a CLT based elastic material model, accounting for the local fibre orientation and weave structure. The complex model model

was implemented in an implicit FE method. Finally, an inverse analysis was used to optimise the thickness of the composite.

In 2002, Sweeting *et al.* [71] modelled the shape distortions of curved circular flanged thermoset laminates due to thermo–forming. The shape distortions were predicted with an FE model using brick elements, incorporating spring–forward in the model. Two approaches were used, one accounting for the fibre redistribution due to draping and taking the resulting laminate properties into account and one modelling the resulting laminate as a planar isotropic material. The fibre redistribution was modelled with a kinematics drape modeller. Shape distortion were predicted by accounting for the chemical shrinkage due to curing and by the thermal contribution due to the curing temperature. Undulation of the yarns in the woven fabrics was not taken into account in the model. The results of both models were in reasonable agreement with the experiments since only small fibre re–arrangement occurred in the products.

Long *et al.* [38] predicted failure of multilayered composite materials based on CLT in 2002. The woven fabrics were modelled as unidirectional layers, taking no undulation into account. Fibre reorientation due to forming was predicted by a kinematics drape modeller. Non–crimp fabric reinforced thermosets and twill weaves reinforced thermoplastics were used in the experimental set–up. The cone shaped products were tested on compression until failure occurred. Assuming linear elastic ply behaviour was not sufficient to model pre–failure crack initiation.

Hofstee [28] coupled a kinematics drape modeller to a woven fabric analysis in 2002 on a pyramid shaped product. The mechanical properties of the weave are predicted, accounting for the geometrical changes in the weaves microstructure due to fibre orientation. Specimens were made from the side parts in the pyramid in order to validate the predicted mechanical properties of the non–orthogonal weaves.

Recapitulating, the currently available models to predict the mechanical properties or the thermal shrinkage and warpage account for the fibre reorientation during draping. However, they do not accurately account for the multi–layer drape behaviour of composite materials since they only are capable of draping layers sequentially. The models, predicting shape distortions, use brick or plate elements combined with an thermo–elastic models during the cooling analysis.

Here, the objective is to model the shape distortions using a FE method with computationally effective plate elements, where draping and subsequent cooling are combined into one software package. These simulations combine the results of the multi–layer drape material model with the local thermo–elastic properties of fabric reinforced composites.

5.2 Strategy

The simulation strategy is similar to the real production process. First draping is simulated, closing the mould, using the FE model described in chapter 3. Then, cooling is simulated using the CLT based model (chapter 4), while keeping the mould closed. The cooling stresses increase until the mould is opened and the product removed. A scheme of the entire simulation is presented in figure 5.1.

During these steps a transition from the drape simulations to the cooling and subsequent removing stage needs to be made. The drape simulation is based on a

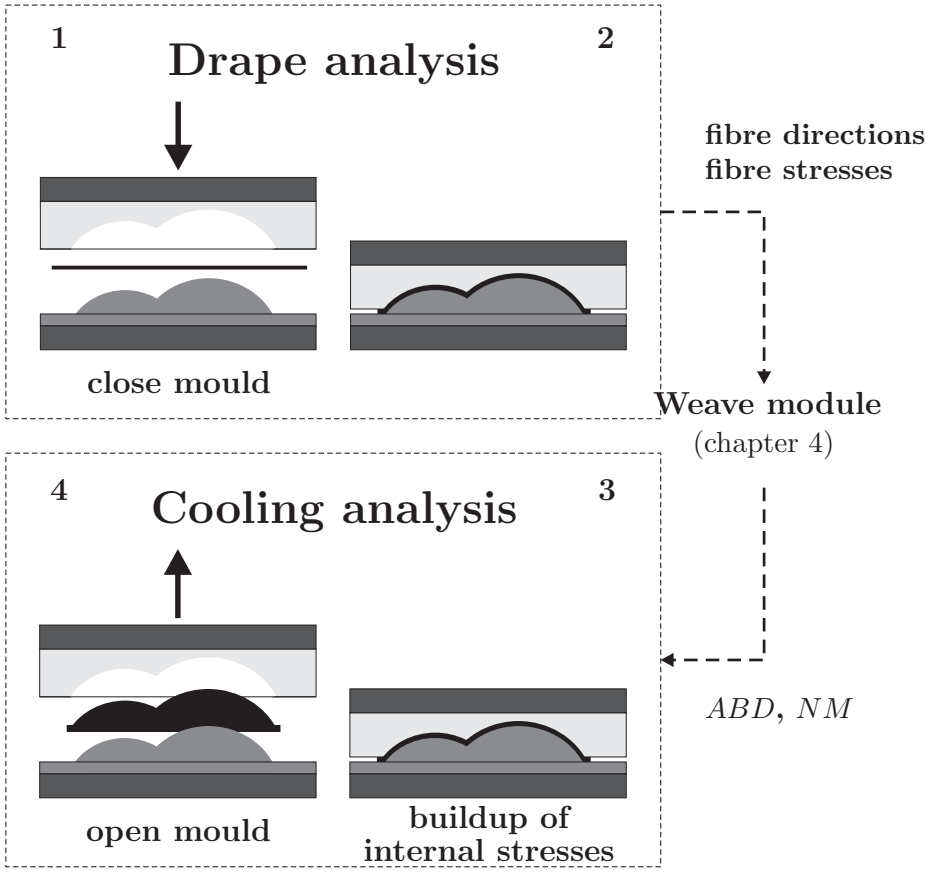

Figure 5.1: Two stage strategy to predict the thermo–elastic properties of composites products.

membrane theory and the cooling stage uses a CLT basis. The next section handles this problem.

5.2.1 From draping to cooling

The drape simulation predicts the fibre orientations and fibre stresses per layer in each element. This information is stored for all integration points of the elements, together with the other state variables. All state variables are updated incrementally during the simulation and stored for the next step.

Normally, the nodal information is stored for post processing purposes, when the FE simulation is stopped. Here, the element information is stored in a file, additional to the nodal information. The simulation can restart by reading the element and nodal data from this file.

Manipulating this restart–file can effectively change the type of simulation. The thermo–elastic module presented in chapter 4 computes the CLT based solution per element integration point. The module returns the ABD stiffness matrix and the thermal and mechanical load vector, accounting for the fibre orientation at the integration point. The state variables from the drape simulation are then replaced by the state variables required for a CLT based simulation.

The CLT based simulation uses Discrete Kirchhoff Triangle (DKT) elements in order

to account for bending. The mesh resulting from draping is used as a reference mesh for the cooling simulation. A second simulation is then started with the new state variables and DKT elements. The shape distortions during cooling are predicted with this simulation.

5.2.2 Thermo–elastic loading

Internal stresses build up in the composite during cooling while the moulds are closed. Stresses in plies are integrated through–the–thickness direction in the CLT formulation, resulting in a load and moment vector, $\{N\}$ and $\{M\}$ respectively. Two types of stress are distinguished during the cooling stage: drape–induced stresses and thermally induced stresses.

The fibre stresses due to draping can induce shape distortions and need accounting for. The stresses in the two fibre directions, σ_i^a and σ_i^b, are assumed homogeneous in the yarns. The stress induced forces and moments are determined by substituting Q_{ij} by σ_i^a and σ_i^b in part a and b of equation (4.30). The other drape–induced stresses, such as the fabric shear response, are neglected during the cooling stage.

The thermally induced load and moment vector are given in equation (4.33). The total load and moment vectors caused by to the drape stresses and the thermal stresses are:

$$\left\{ \begin{array}{c} N_i \\ M_i \end{array} \right\} = -\Delta T \left\{ \begin{array}{c} \overline{A}_i \\ \overline{B}_i \end{array} \right\} + \left\{ \begin{array}{c} N_i^s \\ M_i^s \end{array} \right\}, \tag{5.1}$$

where $\overline{A}_i$ and $\overline{B}_i$ are the thermally induced load and moment vector per °C and ΔT a temperature change. The matrix material solidifies during cooling. The temperature change is determined by the difference in the temperature at which the matrix material can sustain stresses and the room temperature. The thermal load and moment per °C are based on temperature independent coefficients of thermal expansion.

5.2.3 Finite Element implementation

The FE simulation is performed using DKT elements with three in–plane integration points, similarly to the elements used in section 4.4.3. The thermo–elastic loading vectors are introduced as internal loading vectors in the Updated Lagrangian simulation. The internal loading vectors end up in the righthand–side of the predictor–corrector scheme.

5.3 Shape distortions of products

The strategy proposed in the previous sections was applied to model the shape distortions of several products. The first product is the double dome geometry, presented in section 3.7. Secondly, the draping and subsequent cooling of a hemispherical product is simulated.

5.3.1 Double dome geometry

The shape distortions due to cooling of the double dome geometry in the Rubber Press Forming (RPF) process is simulated here. The drape results were presented and verified in section 3.7. Here, only the cooling of the draped product is focussed on.

The deformed mesh resulting from draping was used as a basis in the cooling stage. The material properties required for the cooling stage are presented in section 4.4. The semi–crystalline poly(phenylene sulphide) (PPS) polymer starts crystallising below 250 °C during cooling. The temperature at which the matrix material was able to sustain stresses was assumed to be 180°C.

The fibre stresses are incorporated or neglected in the model, in order to investigate the effect of these stresses on the resulting distortions. The shape distortions of the $[0°/90°|90°/0°]_s$ and $[45°/-45°|-45°/45°]_s$ lay–ups are presented in figure 5.2. First the results of the $[0°/90°|90°/0°]_s$ lay–up are discussed, then the results of the $[45°/-45°|-45°/45°]_s$ lay–up are focussed on.

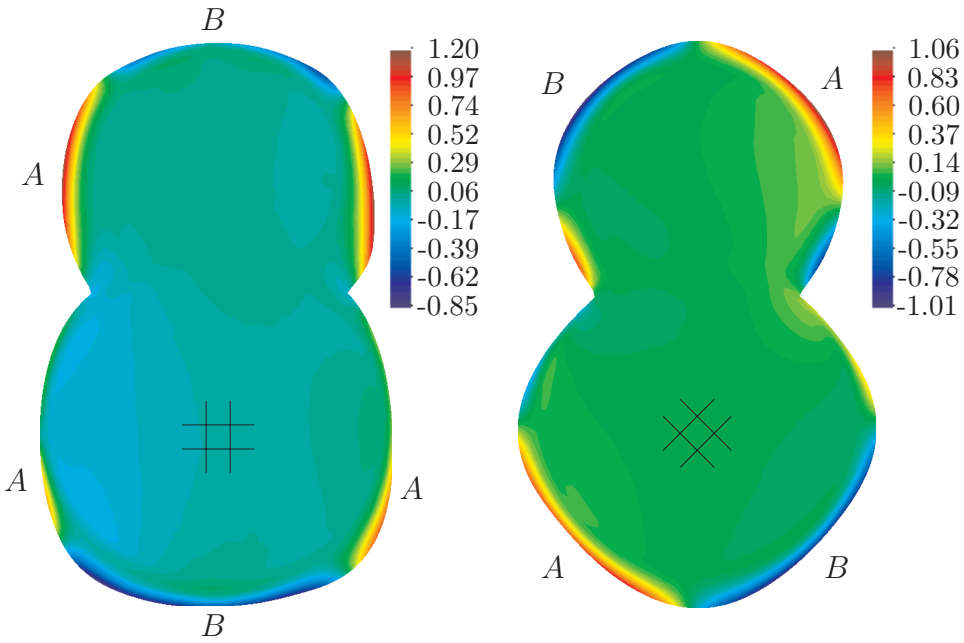

Figure 5.2: The out–of–plane displacements in mm of the double dome product after cooling, relative to the shape after draping. The results for a $[0°/90°|90°/0°]_s$ and $[45°/-45°|-45°/45°]_s$ lay–up are shown. The initial fibre directions, prior to draping, are indicated with black lines.

The distortions in the $[0°/90°|90°/0°]_s$ lay–up rubber pressed products are quite small, only in the order of 1–2 mm. Unfortunately, the distortions of the double dome geometry were not measured. The modelled distortions are therefore only qualitatively compared.

The cooling simulation of the double dome geometry predicted shrinkage and warpage of the product. The in–plane shrinkage was in the order of 0.75 mm in the longitudinal and 0.45 mm in the transverse direction of the product. Also some out–of–plane distortions were predicted by the simulations.

The small flanges at the outer edges of the product, indicated with A and B, bend upwards and downwards in the simulations respectively. The bias directions of the weave separate these areas. The maximum predicted out–of–plane distortions of the product, in the order of 1 mm, are predicted in these flanges. The out–of–plane distortions in the flanges indicated with an A were indeed observed in the double dome products.

Most of the fibre reorientation occurred in the bias direction of the weave for the $[0°/90°|90°/0°]_s$ lay–up. The enclosed fibre angle reduced to approximately 65° in the bias direction at the outer edges of the product. The difference in the thermo–elastic properties resulting from this reorientation is in the order of 40%, see chapter 4. This mismatch in properties can cause internal stresses in the products, resulting in out–of–plane distortions of the flanges.

Incorporating the fibre stresses resulting from draping into the cooling simulation did not lead to a significant change of the distortions. A maximum difference of 0.03 mm was determined at the flange *A*.

The experimentally observed distortions in the $[45°/\text{-}45°|\text{-}45°/45°]_s$ lay–up rubber pressed products are more significant. The products are twisted, resulting in out–of–plane distortions of 7 mm.

As with the $[0°/90°|90°/0°]_s$ lay–up, the cooling simulation of the double dome geometry predicted shrinkage and warpage of the $[45°/\text{-}45°|\text{-}45°/45°]_s$ lay–up product. The in–plane shrinkage was in the order of 0.7 mm in the longitudinal and 0.48 mm in the transverse direction of the product.

The flanges, indicated with *A* and *B*, bent upwards and downwards in the simulations respectively. Again, the bias directions of the weave separate these areas. The maximum and minimum predicted out–of–plane displacement was 1.06 mm and -1.01 mm respectively. The areas *A* and *B* occur in a pattern that resembles twist. However, only deformations in the flanges are predicted, not the twist observed in the experiments. Possibly, the twist in the experiments occurs due to a mis–alignment in the fibre directions prior to forming. Incorporating the fibre stresses into the simulation did not lead to a significant change in the predicted distortions, as with the $[0°/90°|90°/0°]_s$.

Modelling the shape distortions of the double dome geometry with a Quasi Isotropic (QI) lay–up was unsuccessful. The extreme wrinkles resulting from the drape modelling caused the implicit FE simulation not to converge. However, these extreme wrinkles are unacceptable in the application of the product, *i.e.* the product would be rejected for service. Therefore, not being able to model with such extreme wrinkling is not seen as a concern.

The time used for modelling the cooling distortions of the double dome product was 9 minutes on an Athlon XP2000+ PC.

5.3.2 Hemispherical product

Draping and subsequent cooling of plain weave glass fibre reinforced PPS laminates on a hemispherical shape is simulated in the RPF process. The initially square blank of 360×360 mm^2 is formed over a hemisphere with a radius of 80 mm. A structured mesh of 1600 triangular elements is used to model a quarter of the square blank using two lines of symmetry. A detailed description of the moulds is given in appendix D.

The press velocity during draping was set at 500 mm/s, further input parameters for the drape simulations can be found in section 3.6. Shear–locking of the weave was neglected by setting the parameter m to zero. The initial fibre directions of the plain weave [0 ° / 90 °] composite were parallel to the sides of the blank. The temperature at which the matrix material was able to sustain stresses was assumed to be 180℃. The additional parameters for the plain weave are listed in table 4.2.

The deformed mesh after cooling is shown in figure 5.3. Significant fibre reorientation occurred in zone A. The edges of the elements indicate the occurring fibre re–arrangement. The angle between the fibres reached a minimum of 30°. A relatively high stiffness and low thermal expansion results in the global 45° direction from these fibre directions. Very little shearing occurred in zone B. The enclosed fibre angle remains 90°, resulting in a more evenly distributed thermo–elastic properties. Kinematic drape modelers are very well capable of predicting the fibre reorientation pattern for an hemispherical product.

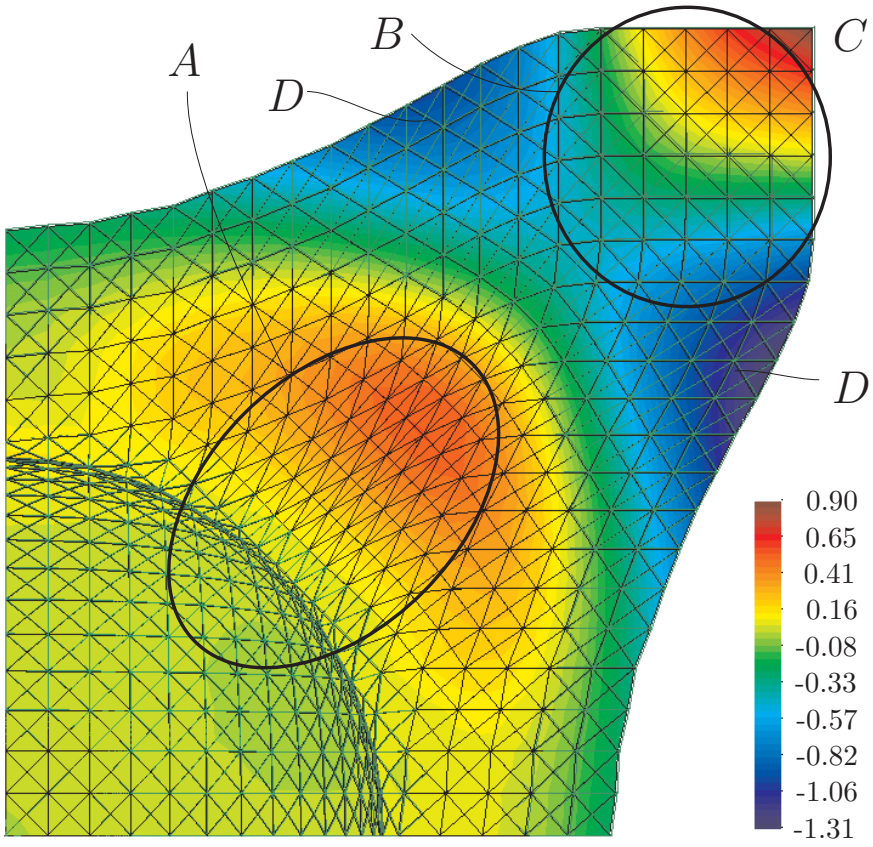

Figure 5.3: Deformed mesh of the hemispherical product after cooling, relative to the mesh after draping. The out–of–plane displacements of the product are depicted in mm.

The mesh resulting from draping is used as a reference for the distortions of the product. The in–plane deformations due to cooling are quite small, only up to 0.1 mm. The out–of–plane deformations are shown by the coloured areas in the mesh after cooling. Significant out–of–plane deformations occur in the flange of the released product. A wave develops in the flange. The maximum negative out–of–plane displacement is approximately -1.3 mm and occurs at positions D. The maximum positive out–of–plane displacement occurs at position C and is 0.9 mm. Zone A also has of positive out–of–plane displacement.

The thermo–elastic properties change locally due to fibre orientation. The mismatch in stiffness and thermal expansion during cooling in the areas with little shearing B and

significant shearing A results in membrane stresses. The out–of–plane displacements develop from the membrane stresses builtup during cooling.

The maximum predicted fibre stress by the drape simulation was 220 MPa and occurred in the spherical part of the product. Fibre stresses are very small in the flanges, only up to 7 MPa. Incorporating or neglecting the drape predicted fibre stresses in the cooling simulation resulted in a maximum difference of 0.013 mm in the out–of–plane displacement. This difference occurred at position C in figure 5.3. The fibre stresses have an insignificant effect on the shape distortions in this example since the geometric stiffness in the hemispherical part of the product is high.

The time used for modelling the shape distortions of the product was 9 minutes on an Athlon XP2000+ PC. Draping was simulated in 5 minutes; the remaining time was used for the cooling simulation.

5.3.3 Wing leading edge stiffener

Draping and subsequent cooling of a wing leading edge stiffener is simulated in the RPF process. The pre–form of the rib is modelled using an unstructured mesh of 11055 elements. The size of the product is approximately 280 × 250 × 60 mm. The shape of the pre–form and the lower steel tool are depicted in figure 5.4.

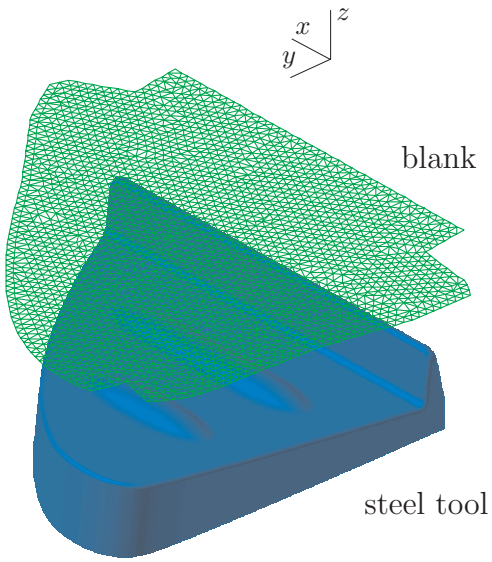

Figure 5.4: Wing leading edge rib set–up; the lower steel mould and the meshed pre–form. The upper rubber tool and the blank holder are not shown for clarity purposes.

The press velocity during draping and further input parameters for the drape simulations can be found in section 3.6. The initial fibre arrangement of the satin 8H weave glass fibre reinforced PPS laminates was a $[45°/\text{-}45°|0°/90°]_s$, or QI, lay–up. The orientation of the fibres was with respect to the xyz–coordinate system. Again, the temperature at which the matrix material was able to sustain stresses was assumed to be 180°C. The additional parameters for the satin 8H weave are listed in table 4.2.

The results after draping are depicted in figure 5.5. Wrinkles are observed in the experiments and the simulated shape. These wrinkles are indicated with arrows and occur at the nose and next to the nose of the rib. Here, the material is actually folded. Little fibre reorientation occurred in the top surface, indicated with an A in figure 5.5,

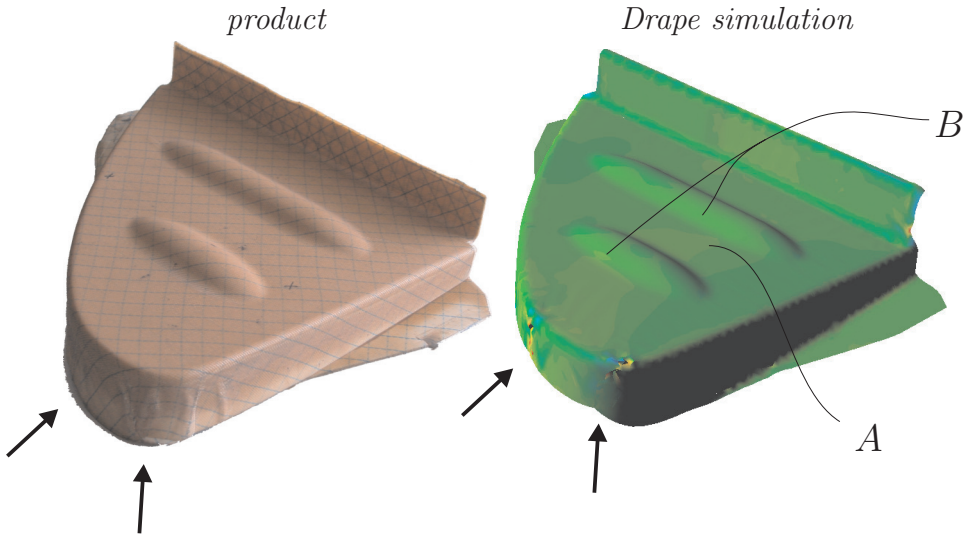

Figure 5.5: Wing leading edge rib after draping; experimental and modelled shape. Wrinkles are indicated with arrows

of the product. The fabric layers only sheared approximately 5° in this area. More shearing, up to 20° shear deformation, occurred in the flanges of the product.

The pressed product is milled prior to mounting it in the wing leading edge. Milling was simulated by removing elements from the mesh. This operation is called trimming [4]. The wrinkles, occurring due to forming, are removed from the product due to this operation, both in reality and in the simulation. Trimming was performed while the moulds were closed in the FE simulation, at the end of the drape simulation. The mesh reduced from 11055 elements to 7359 elements during this operation. The transition from the drape analysis into the cooling analysis was performed after trimming. The trimmed mesh and its internal CLT load vector in x– and y–direction are depicted in figure 5.6.

The modelled CLT load and moment vector in the mesh are very high and considered an overestimation of the "true" internal CLT load and moment vector. The high load vector is caused by the overestimation of the fibre stresses during the drape simulation. The maximum predicted fibre stress by the drape simulation was approximately 1600 MPa in each of the individual layers. These stresses occurred in the area between the two cigar shaped stiffeners on the top surface of the rib, indicated with B in figure 5.5.

The shape distortions are predicted while neglecting and accounting for the drape–induced fibre stresses. The out–of–plane displacements are depicted relatively to the shape of the mesh after trimming in figure 5.7.

The shape distortions due to cooling are quite small when neglecting the fibre stresses. Basically, the product becomes smaller, and little out–of–plane displacement, or warpage, is predicted. The absence of warpage can be explained from the fairly homogenous thermal expansion coefficients of the QI lay–up, even after draping. Most fabric shearing

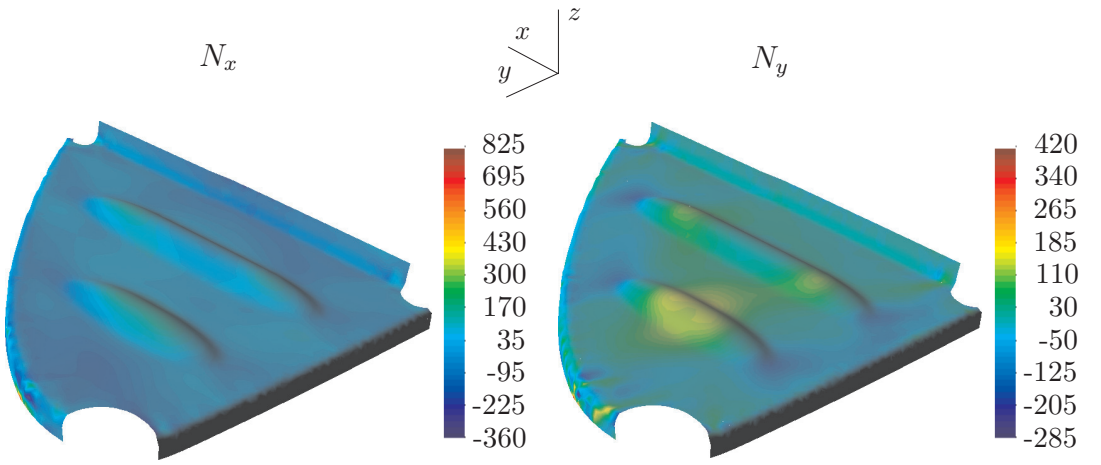

Figure 5.6: Milling of the rib was simulated by trimming the FE mesh. The CLT load vector (N/mm) in the x– and y–direction in the trimmed mesh, prior to the release of the product from the mould, are depicted. The CLT load vector accounts for the drape–induced fibre stresses.

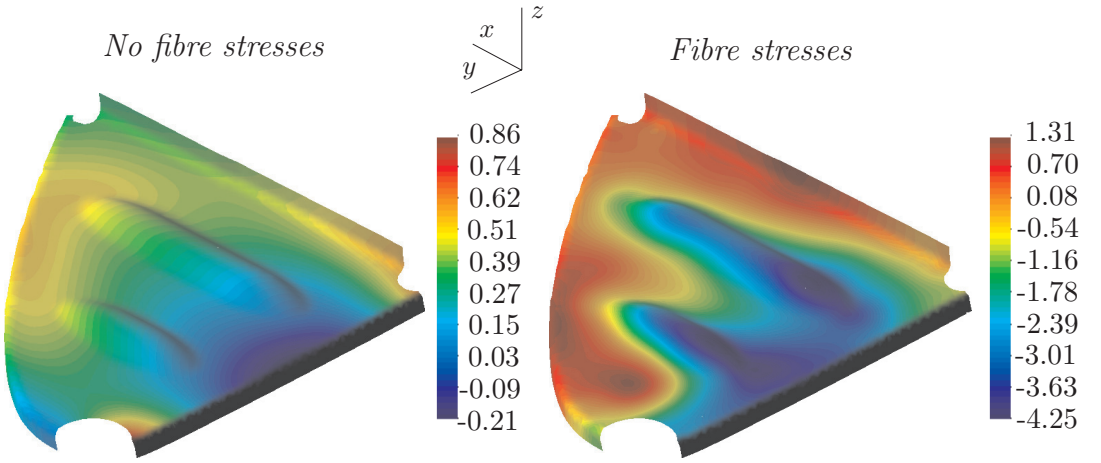

Figure 5.7: Deformed mesh of the wing leading edge rib after cooling, relative to the mesh after trimming. The out–of–plane displacements of the product are depicted in mm.

occurs in the flanges of the product, not in the top surface. Little membrane stresses due to a mismatch in thermal expansion coefficient results from this.

Significant warpage is predicted when accounting for the drape–induced fibre stresses. Out–of–plane displacements of approximately 5 mm are predicted. Warpage results from the inhomogeneous distribution of the fibre stresses after draping. Membrane stresses result from this inhomogeneous distribution, in turn leading to shape distortion. However, the drape–induced fibre stresses are overestimated by the model, resulting in an overestimation of the membrane stresses and consequently the shape distortions.

5.4 Conclusion

A method was presented to model the shape distortions of woven fabric reinforced composite materials. It incorporates the fibre reorientation due to draping and the subsequent effect on the local thermo–elastic properties of the product.

Incorporating the fibre directions into the model is required to find the shape distortions of the woven fabric reinforced products. Mismatch in thermal expansion in the product can result in out–of–plane distortions when membrane stresses can develop.

Incorporating fibre stresses resulting from draping results in small changes in product distortions for both the double dome product and the hemispherical product. When accounting for the drape–induced fibre stresses, significantly more shape distortions are predicted for the wing leading edge rib, with a $[45\%\text{-}45°|0\%90°]_s$ lay–up. These distortions are considered as an upperbound for the shape distortions since the drape–induced fibre stresses are considered an overestimation of the true fibre stresses.

5.5 Recommendations

The matrix material is a plastic, hence viscoelastic and temperature dependent by nature. The effect of viscoelasticity or temperature is not incorporated in the model. Currently, a temperature is assumed at which the matrix material is able to sustain stresses. Investigation of the effect of viscoelasticity and thermal dependency of the plastic material on the composite properties is therefore recommended for further research.

The shrinkage of the matrix material is currently based in thermal expansion behaviour only. Semi–crystalline polymers also shrink due to crystallisation. Similarly, thermosetting polymers shrink during curing. Extending the material to incorporate chemical and crystallisation shrinkage is therefore recommended.

Chapter 6

Conclusions and recommendations

A method for modelling the processing–induced shape distortions of composite materials has been presented. It incorporates the fibre reorientation and the thermal shrinkage and warpage of the composite during forming while accounting for the process specific boundary conditions. A two stage strategy is used to simulate the shape distortions of the product: first the fibre reorientation, or draping, is modelled, whereafter the cooling stage is modelled.

The method incorporates an improved prediction for the fibre re–arrangement for multi–layered composites compared to the models available in literature. Both the draping and cooling stage are modelled in the same software package. The model uses computationally attractive plate elements, providing an computationally attractive modelling tool. The model is used in the development stage of thermoplastic composite products at Fokker AESP.

A drape model has been presented to model the fibre reorientation of a woven fabric composite during forming. The model, a multi–layer extension to the fabric reinforced fluid model, was implemented into an implicit Finite Element (FE) code. It incorporates a bi–axial fabric, including its shear response, in a Newtonian viscous–like matrix material, using a constant slip law between the individual layers.

Drape experiments of woven fabric reinforced thermoplastic composites were performed using the Rubber Press Forming process. The pressing process was simulated with the developed FE drape model, a geometrical drape model and an FE model with multiple membrane elements through–the–thickness of the sheet. The results of the experiments and modelling were compared. Both the experiments and the finite element models confirm a clear dependency between the drape–ability and the laminate lay–up. $[45°/\text{-}45°|0°/90°]_s$, or Quasi Isotropic (QI), lay–ups drape significantly worse than $[0°/90°|90°/0°]_s$ and $[45°/\text{-}45°|\text{-}45°/45°]_s$ lay–ups. The QI lay–ups lead to wrinkling while the other lay–ups do not. The reduced drape–ability of QI lay–ups is caused by the interlaminar shear between the individual fabric layers. Therefore, only drape models that account for the interlaminar shear between the fabric layers during forming are capable of modelling the draping of multilayered composite accurately. Geometrical drape models do not incorporate a mechanism for interlaminar shear and appear incapable of modelling the drape behaviour of multilayered composites accurately.

Measurements on a double dome geometry revealed that the predicted enclosed fibre angles of the FE simulations are slightly better than those of the geometrical drape method for $[0°/90°|90°/0°]_s$ and $[45°/\text{-}45°|\text{-}45°/45°]_s$ lay–ups. Bridging during forming

contributes to the reduction of accuracy of the geometrical model.

The results of the developed multi–layer FE model and the FE model with multiple membrane elements through–the–thickness of the sheet are similar. However, the multi–layer drape model is far less CPU intensive. A time reduction by a factor of seven was obtained for the double dome geometry, which will increase with mesh refinement. Both models predict unrealistically high fibre stresses. Further research on the effects of fibre straightening, fibre slip and the interlaminar shear behaviour of these composites during forming is therefore recommended.

Material parameters can be determined using the picture frame experiment. These experiments show a clear dependency of the formability of the composite and the temperature. Temperature dependent drape behaviour during forming seems an important mechanism to incorporate into the model.

A model to determine the in–plane thermomechanical properties of laminates built from non–orthogonal, or sheared, bi–axially woven fabric composites is presented. It is capable of including the variable fibre directions due to draping in a mechanical analysis. The model assumes constant properties of the fibres and plastic while accounting for the linear thermo–elastic properties only. Biaxial woven fabrics of arbitrary structure can be described by this model.

The model gives good correlation with the experimental results for a plain weave and an 8H satin weave when a uniform state of basic element strain is used. The uniform state of basic element strain provides an upper bound for the stiffness. The modelled and experimental results both show a significant difference between the thermomechanical properties of sheared and orthogonal woven fabrics. It is thus necessary to account for the change in fibre directions in woven fabric composites in order to accurately predict the thermomechanical properties.

Combining the variable fibre directions with a mechanical analysis enables the prediction of the effect of local stiffness variations on the global mechanical behaviour of the product. Similarly, the local change in thermal expansion of the composite due to fibre reorientation is required to predict the shape distortions of the products.

The internal stresses in the product result in shape distortions when releasing it from the mould. These stresses occur due to local changes in thermal expansion or drape–induced stresses. The effect of the processing–induced fibre stresses is incorporated into the prediction of these product distortions. Irreversible shrinkage, such as cure shrinkage and crystallisation shrinkage is not accounted for in the model. Incorporating these shrinkage effects would increase the applicability of the model. Besides, no criterion is included to determine when the matrix is capable of transferring stresses during cooling or curing.

A mismatch in thermal expansion due to the locally changed fibre directions in the product can result in significant out–of–plane distortions when membrane stresses develop. The effect is illustrated with a numerical example of a hemispherical product. Drape–induced residual stresses can also results in out–of–plane distortions of the product, as illustrated with the numerical example of the wing leading edge rib. Out–of–plane distortions in products involves flexural deformations and this effect is most important in thin structures, without double curvature, having a low bending stiffness. Incorporating the effect of fibre re–arrangement and processing induced stresses is essential to the prediction of shape distortions during cooling.

The time required for simulating the processing induced shape distortions of a composite product is reasonable. Simulating the distortions of the double dome geometry is possible within 45 minutes using a mesh of approximately 7000 elements on a moderate personal computer. Modelling the shape distortions of the hemispherical used 9 minutes, using a mesh of 1600 elements.

Bibliography

[1] Akkerman, R., and de Vries, R. Thermomechanical properties of woven fabric composites. In *Proceedings of the International Conference on Fibre Reinforced Composites FRC '98, Newcastle, United Kingdom* (1998), A. Gibson, Ed., Woodhead publishing limited, pp. 422–429.

[2] ASTM. Astm d 3039–76. *Annual book of ASTM Standards 08.01* (1989).

[3] Atkinson, K. *An introduction to numerical analysis*. John Wiley & Sons, 1989.

[4] Avetisyan, M., Meinders, T., and Huétink, J. Improvement of springback predictability after forming and trimming operations. In *Proceedings of the 7th ESAForm conference on material forming, Trondheim, Norway* (2004), F. Chinesta, E. Cueto, N. Sukumar, C. Rey, and D. Ryckelynck, Eds., p. arcticle in press.

[5] Batoz, J. A study of three–node triangular plate bending elements. *International Journal for Numerical Methods in Engineering 15* (1980), 1771–1812.

[6] Belytschko, T., Liu, W., and Moran, B. *Nonlinear Finite Elements for Continua and Structures*. John Wiley & Sons, 2000.

[7] Bergsma, O. *Three–dimensional Simulation of Fabric Draping*. PhD thesis, Delft University of Technology, November 1995. Ph.D. Thesis, Structures and Materials Laboratory.

[8] Boisse, P., Borr, M., Buet, K., and Cheroaut, A. Finite element simulation of textile composite forming including the biaxial fabric behaviour. *Composites Part B*, 28 (1997), 453–464.

[9] Boisse, P., Gasser, A., and Hivet, G. Analyses of fabric tensile behaviour: determination of the biaxial tension–strain surface and their use in forming simulations. *Composites Part A*, 32–10 (October 2001), 1395–1414.

[10] Bowles, D., and S.S., T. Prediction of coefficients of thermal expansion for unidirectional composites. *Journal of Composite Materials 23* (1989), 370–388.

[11] Breen, D., House, D., and Wozny, M. A particle–based model for simulating the draping behavior of woven cloth. *Textile Research Journal 64*, 11 (November 1994), 663–685.

[12] Bunsell, A. *Fibre Reinforcements for Composite Materials*, vol. 2 of *Composite Materials Series*. Elesevier, 1988.

[13] Carleer, B. *Finite Element analysis of deep drawing.* PhD thesis, Twente University, March 1997. Ph.D. Thesis, Applied Mechanics Group.

[14] Chamis, C. Nasa tech. memo 8320. *MEMO* (1983).

[15] Chen, B., and Govindaraj, M. A physically based model of fabric drape using flexible shell theory. *Textile Research Journal 65*, 6 (1995), 324–330.

[16] Cherouat, A., and Billoët, J. Mechanical and numerical modelling of composite manufacturing processes in deep–drawing and laying–up of thin pre–impregnated woven fabrics. *Materials Processing Technology 118* (2001), 460–471.

[17] Cheruet, A., Soulat, D., Boisse, P., Touratier, M., Soccard, E., Maison-Le Poec, S., and Guinard, S. Simulation of thermoplastic composite forming using shells with pinching elements. In *Proceedings of the sixth conference on Computational structures technology* (2002), Civil–Comp press, pp. 209–210.

[18] Chou, T., and Ishikawa, T. Analysis of two dimensional fabric composites. *Textile Structural Composites* (1991), 209–264.

[19] Chou, T., and Ishikawa, T. Mechanics of composite materials. *Textile Structural Composites* (1991), 31–37.

[20] Colombo, G., Prati, M., and Rizzi, C. Design and evaluation of a car soft top. In *XII ADM International Conference, Rimini, Italy* (2001).

[21] Cordier, F., and Magnenat-Thalmann, N. Real–time aninmation of dressed virtual humans. *Eurographics 2002 21*, 3 (2002).

[22] Daniel, I., and Ishai, O. *Engineering Mechanics of Composite Materials.* Oxford University Press, 1994.

[23] de Luca, P., Lefébure, P., and Pickett, A. Numerical and experimental investigation of some press forming parameters of two fibre reinforced thermoplastics: APC2–AS4 and PEI–CETEX. *Composites Part A*, 29 (1998), 101–110.

[24] dieka. *DiekA manual.* university of Twente, Enschede, the Netherlands, 2003.

[25] Falzon, P., and Herzberg, I. Effects of compaction on the stiffness and strength of plain weave fabric RTM composites. *Journal of Composite Materials 30* (1996), 1211–1247.

[26] Hashin, Z. Analysis of composite materials – a survey. *Journal of Applied Mechanics 50* (1983), 481–505.

[27] Heisley, F., and Haller, K. Fitting woven fabric to surfaces in three dimensions. *Journal of the Textile Institute 2* (1988), 250–263.

[28] Hofstee, J., de Boer, H., and van Keulen, F. Elastic stiffness analysis of thermo–formed plain–weave composite part iii: experimental verification. *Composites Science & Technology 62* (2002), 401–418.

[29] Hsiao, S.-W., and Kikuchi, N. Numerical analysis and optimal design of composite thermoforming process. *Computer methods in applied mechanics and engineering 177* (1999), 1–34.

[30] Ivanov, I., and Tabiei, A. Flexible woven fabric micromechanical material model with fiber reorientation. *Mechanics of Advanced materials and structures 9* (July 2002), 37–51.

[31] Kang, T., and Yu, W. Drape simulation of woven fabric by using the finite–element method. *Journal of the Textile Institute 86*, 4 (1995), 635–648.

[32] Kato, S., Yoshino, T., and Minami, H. Formulation of constitutive equations for fabric membranes based on the concept of fabric lattice model. *Engineering Structures 21* (1999), 691–708.

[33] Kawabata, S. The standardization and analysis of hand evaluation. In *Hand evaluation and standardization committee of the Textile Machinery Society of Japan: Osaka, Japan* (1975).

[34] Kloosterman, G. *Contact Methods in Finite Element Simulations.* PhD thesis, Twente University, December 2002. Ph.D. Thesis, Applied Mechanics and Polymers Group.

[35] Lamers, E., Akkerman, R., and Wijskamp, S. Fibre orientation modelling for rubber press forming of thermoplastic laminates. In *Proceedings of the 5th ESAForm conference on material forming, Krakow, Poland* (2002), M. Pietrzyk, Z. Mitura, and J. Kaczmar, Eds., pp. 323–326.

[36] Lamers, E., Wijskamp, S., and Akkerman, R. Modelling the thermo–elastic properties of skewed woven fabric reinforced composites. In *Proceedings of ECCM 9, Brighton, UK* (2000), pp. CD–proceedings.

[37] Lim, T.-C., and Ramakrishna, S. Modelling of composite sheet forming: a review. *Composites Part A*, 33 (October 2002), 515–537.

[38] Long, A., Crookston, J., Gil, R., Jones, I., and M.J., C. Effects of intra–ply shear during forming on tensile properties of textile composites. In *Texcomp–6, International Conference on Textile Composites, Philadelphia, Pennsylvania, USA* (2002), M. Marmel, Ed.

[39] Long, A., and Rudd, C. A simulation of reinforcement deformation during the production of preforms for liquid moulding processes. *Journal of Engineering Manufacture, The Institution of Mechanical Engineers 208* (1994), 269–278.

[40] Mack, C., and Taylor, H. The fitting of woven cloth to surfaces. *Journal of Textile Institute 47* (1956), 477–487.

[41] Moldflow Cooperation. *Moldflow plastics advisor database.* www.Moldflow.com, 2004.

[42] Ticona GmbH. *Datasheet Fortron.* Campus V4.1, www.CAMPUSPlatics.com, 1998.

[43] McEntee, S., and Ó Brádaigh, C. Large deformation finite element modelling of single–curvature composite sheet forming with tool contact. *Composites Part A*, 29 (1998), 207–213.

[44] McGuinness, G., and Ó Brádaigh, C. Development of rheological models for forming flows and picture– frame shear testing of fabric reinforced thermoplastic sheets. *Journal of Non–Newtonian Fluid Mechanics 73*, 1–2 (November 1997), 1–28.

[45] Meinders, V. *Developments in numerical simulations of the real–life deep drawing process*. PhD thesis, Twente University, February 2000. Ph.D. Thesis, Applied Mechanics Group.

[46] Meriam, J., and Kraige, L. *Engineering mechanics, statics, SI version*. Wiley & Sons inc., 1998.

[47] Mohammed, M., Lekakou, C., Dong, L., and Bader, M. Shear deformation and micromechanics of woven fabrics. *Composites Part A*, 31 (2000), 299–308.

[48] Murtagh, A., and Mallon, P. Characterisation of shearing and frictional behaviour during sheet forming. In *Composite sheet forming*, D. Bhattacharyya and R. Pipes, Eds., vol. 11 of *Composite material series*. Elsevier, Amsterdam, 1997, pp. 163–214.

[49] Naik, N., and Shembekar, P. Elastic behaviour of woven fabric composites: I–laminate analysis. *Journal of Composite Materials 26* (1992), 2196–2225.

[50] Naik, N., and Shembekar, P. Elastic behaviour of woven fabric composites: II–laminate analysis. *Journal of Composite Materials 26* (1992), 2227–2246.

[51] Nijhof, A. *Ontwerpen in vezelversterkte kunststoffen*. TU Delft, 1990.

[52] Åström, B. T. Thermoplastic composite sheet forming: materials and manufacturing techniques. In *Composite sheet forming*, D. Bhattacharyya and R. Pipes, Eds., vol. 11 of *Composite material series*. Elsevier, Amsterdam, 1997, pp. 27–72.

[53] Peng, X., Xue, P., Chao, J., Lussier, D., and Chen, J. Normalization in the picture frame test of woven composites, length or area. In *Proceedings of the 5th ESAForm conference on material forming, Krakow, Poland* (2002), M. Pietrzyk, Z. Mitura, and J. Kaczmar, Eds.

[54] Peters, S. *Handbook of composiets*. Chapman & Hall, 1998.

[55] Potter, K. The influence of accurate stretch data for reinforcements on the production of complex structural mouldings. *Composites* (July 1979).

[56] Powell, P. *Engineering with Fibre–Polymer Laminates*. Chapman & Hall, 1994.

[57] Prodromou, A., and Chen, J. On the relationship between shear angle and wrinkling of textile composite preforms. *Composites Part A*, 28A (October 1997), 491–503.

[58] Robertson, R., Hsiue, E., and Yeh, G. Fibre rearrangements during the moulding of continuous fibre composites ii. *Polymer Composites 5* (1984), 191–197.

[59] Rogers, T. Rheological characterisation of anisotropic materials. *Composites Vol. 20*, 1 (1989), 21–27.

[60] Rosato, D. V. *Plastic processing data handbook*. Chapman & Hall, 1997.

[61] Rosen, B. W., and Hashin, Z. Effective thermal expansion coefficients and specific heats of composite materials. *Journal of Composite Materials 8* (1970), 157–173.

[62] Schapery, R. Thermal expansion coefficients of composite materials based on energy principles. *Journal of Composite Materials 2*, 3 (1968), 380–404.

[63] Schneider, W. Wärmeausdehnungskoeffizienten und wärmespannungen von glassfaser/kuststoff–verbunden. *Kunststoffe 63* (1973), 992.

[64] Schowalter, W. *Mechanics of non–Newtonian fluids*. Pergamon press, 1978.

[65] Sharma, S., and Sutcliffe, M. A simplified finite element approach to draping of woven fabric. In *Proceedings of the 6th ESAForm conference on material forming, Salerno, Italy* (2003), P. Boisse, R. Akkerman, A. Long, and L. Nicolais, Eds.

[66] Sidhu, R., Averill, R., Riaz, M., and Pourboghrat, F. Finite element analysis of textile composite preform stamping. *Composite Structures 52* (2001), 483–497.

[67] Smiley, A., and Pipes, R. Analysis of the diaphragm forming of continuous fiber reinforced thermoplastics. *Journal of Thermoplastic Composite Materials 1* (1988), 298–321.

[68] Spencer, A. Theory of fabric–reinforced viscous fluids. *Composites Part A*, 31 (2000), 1311–1321.

[69] Spencer, A. A theory of viscoplasticity for fabric–reinforced composites. *Journal of the Mechanics and Physics of Solids 49* (2001), 2667–2687.

[70] Stoker, H. *Developments of the Arbitratry Lagrangian–Eulerian Method in non–linear Solid Mechanics*. PhD thesis, Twente University, February 1999. Ph.D. Thesis, Applied Mechanics and Polymers Group.

[71] Sweeting, R., Liu, X., and Paton, R. Prediction of processing–induced distortion of curved flanged composite laminates. *Composite Structures 57* (2002), 79–84.

[72] Tanov, R., and Brueggert, M. Finite element modelling of non–orthogonal loosely woven fabrics in advanced occupant restraint systems. *Finite Elements in Analysis and Design 39* (2003), 357–367.

[73] Trochu, F., Hammami, A., and Benoit, Y. Prediction of fibre orientation and net shape definition of complex composite parts. *Composites Part A*, 27 (1996), 319–328.

[74] van den Boogaard, A. *Thermally enhanced forming of aluminium sheet*. PhD thesis, Twente University, December 2002. Ph.D. Thesis, Applied Mechanics Group.

[75] Van Leer, B. Towards the ultimate conservative difference scheme. iv. a new approach to numerical convection. *Journal of Computational Physics 23* (1977), 276–299.

[76] Vandeurzen, P., Ivens, J., and Verpoest, I. A three dimensional micro mechanical analysis of woven fabric composites: I. elastic analysis. *Composites Science and Technology 56* (1996), 1317–1327.

[77] Vandeurzen, P., Ivens, J., and Verpoest, I. A three dimensional micro mechanical analysis of woven fabric composites: I. geometric analysis. *Composites Science and Technology 56* (1996), 1303–1315.

[78] Vreugdenhil, C., and Koren, B. Numerical methods for advection–diffusion problems. *Notes on numerical fluid mechanics 54* (1993).

[79] Weeën, F. v. d. Algorithms for draping fabric on doubly–curved surfaces. *International journal for numerical methods in engineering 31* (1991), 1415–1426.

[80] Whitney, J., and McCullough, R. *Micromechanical Materials Modelling*, vol. 2 of *Delaware composites and design encyclopaedia*. Technomic, Lancaster PA, 1990.

List of symbols

Scalars

d	Fibre diameter
d	Contact penetration
E	Modulus of elasticity
F	Force
G	Shear modulus
h	height, thickness
l	length
K	Bulk modulus
m	Constant for fabric shear response
M	Moment
n	Constant for fabric shear response
P	Power
Pi	Work
p	Hydrostatic pressure
p_n	Contact penalty parameter
t	time
T	Temperature
U	Undulation factor
V_m	Matrix volume fraction
V_f	Fibre volume fraction
β	Viscous friction factor
Γ	Body surface
η	Viscosities
θ	Material deformation angle
ϑ	Arbitrary scalar
λ	Stretch
ν	Poisson's constant
ϕ	Half of the enclosed fibre angle between the fibre families
Ω	Body volume
ρ	Density
ϱ	Undulation angle of the yarn
Φ	Interface surface

Vectors

$\boldsymbol{a}$	Direction of fibre family a
$\boldsymbol{b}$	Direction of fibre family b
$\boldsymbol{s}$	bias direction of the weave
$\boldsymbol{f}$	Sum of forces on boundary
$\boldsymbol{n}$	Normal vector
$\boldsymbol{t}$	Traction
$\boldsymbol{N}$	Force per unit width
$\boldsymbol{M}$	Moment per unit width
$\boldsymbol{u}$	Displacement
$\boldsymbol{v}$	Velocity
$\boldsymbol{x}$	Spatial position
$\boldsymbol{X}$	Reference position
$\boldsymbol{\alpha}$	Thermal expansion
$\boldsymbol{\gamma}$	Interface traction
$\boldsymbol{\varepsilon}$	Linear strain
$\boldsymbol{\vartheta}$	Arbitrary position
$\boldsymbol{\kappa}$	Curvature
$\boldsymbol{\sigma}$	True stress
$\boldsymbol{\varphi}$	Rotation
$\boldsymbol{\chi}$	Reference position

Matrices

$[ABD]$	Classical Laminate Theory stiffness matrix
$[abhd]$	Classical Laminate Theory compliance matrix
$[Q]$	In–plane stiffness matrix
$[R]$	Reuter matrix
$[T]$	Rotation matrix

2nd order tensors

$\underline{D}$	Rate–of–deformation tensor
$\underline{F}$	Deformation gradient tensor
$\underline{I}$	Unit (Idendity) tensor
$\underline{L}$	Velocity gradient tensor
$\underline{R}$	Rotation tensor
$\underline{T}$	Transformation tensor
$\underline{W}$	Spin tensor
$\underline{\varepsilon}$	Linear strain tensor
$\underline{\sigma}$	True stress tensor

$\underline{\tau}$	True stress tensor
$\underline{\omega}$	Rotation tensor

4th order tensors

$\underline{\underline{M}}$	Material tensor

Functions

m	Fibre trajectory function
s	Fibre cross–sectional shape function
$\boldsymbol{\varphi}$	Mapping function
$\boldsymbol{\psi}$	Invariant function

Operators

I_A	first invariant of $\underline{A}$
II_A	second invariant of $\underline{A}$
III_A	third invariant of $\underline{A}$
$\underline{A}^{-1}$	Inverse of $\underline{A}$
$\underline{A}^{\mathrm{T}}$	Transpose of $\underline{A}$
$\underline{A}^{-\mathrm{T}}$	Inverse transpose of $\underline{A}$
$\overleftarrow{\nabla}$	Post–gradient operator
$\vec{\nabla}$	Pre–gradient operator
$\cdot$	tensor contraction
:	double tensor contraction
$\mathrm{tr}\,\underline{A}$	trace of $\underline{A}$
$\|\vartheta\|$	2–norm of ϑ

Appendix A

Continuum mechanics

Generally, a continuum mechanics approach is used in order to describe deformations in forming processes. The method relates the movement of an arbitrary continuous media (section A.1) to its deformations (section A.2) and the resulting stresses (section A.3). Continuum mechanism have to obey conservation laws, these are: the conservation of mass, momentum and energy (section A.4).

When discretising the continuum into smaller parts, these smaller parts contribute to the macroscopic deformation and by using the Finite Element (FE) method, the macroscopic deformations can be determined. Continuum mechanics describe the deformation of the continuum. These deformations result in stresses. The relation between the deformations and stresses is defined in constitutive equations. This appendix is to a large extend based on the work of Belytschko *et al.* [6], Meinders [45], Stoker [70] and Van den Boogaard [74].

A.1 Kinematics

Kinematics are used in order to describe the movement of particles and coordinate system in a continuum. A coordinate system or frame is required to define kinematics. Three descriptions are generally used:

- the Lagrangian description of motion, where the particles are expressed in the initial coordinates;
- the Eulerian description of motion, where the particles are expressed in the current coordinates;
- the referential description of motion, where the particles are expressed in the reference coordinates.

Each description has its benefits. The Lagrangian description of motion is generally applied for describing physical variables that are associated with material points. The Eulerian description is used when the objective is to describe physical variables in space. The referential description of motion is the combination of the Lagrangian and Eulerian position. It is used when both the spatial and material description are less suitable.

A.1.1 Coordinate systems

A particle located at position $\boldsymbol{X}$ in the initial state is moving in time to the current state $\boldsymbol{x}(\boldsymbol{X}, t)$ in a domain, as shown in Figure A.1.

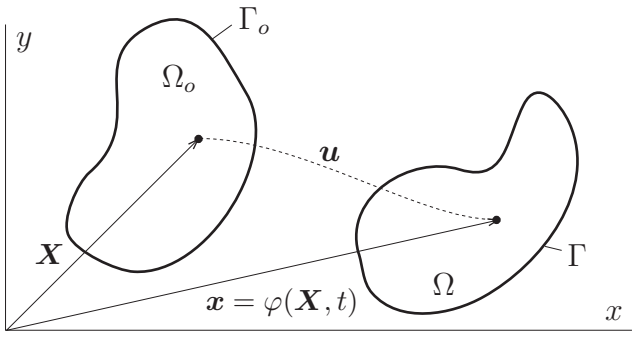

Figure A.1: Body deforming from initial state to current state.

The domain $\boldsymbol{\Omega}_o$ in the initial configuration with the boundary $\boldsymbol{\Gamma}_o$, changes to the current domain $\boldsymbol{\Omega}$ with boundary $\boldsymbol{\Gamma}$. The function $\varphi(\boldsymbol{X}, t)$ maps the initial configuration onto the current configuration at time t. In a Lagrangian description of motion, the material point is related to the initial configuration as:

$$\boldsymbol{x} = \varphi(\boldsymbol{X}, t), \tag{A.1}$$

where $\boldsymbol{X}$ is the position of the material point $\boldsymbol{x}$ at time t is zero. Then the displacement of a material point becomes:

$$\boldsymbol{u} = \boldsymbol{u}(\boldsymbol{X}, t) = \varphi(\boldsymbol{X}, t) - \varphi(\boldsymbol{X}, t = 0) = \boldsymbol{x} - \boldsymbol{X}. \tag{A.2}$$

The material velocity $\boldsymbol{v}(\boldsymbol{X}, t)$ is the time derivative of the position vector:

$$\boldsymbol{v}(\boldsymbol{X}, t) = \frac{\mathrm{d}\varphi(\boldsymbol{X}, t)}{\mathrm{d}t} = \left.\frac{\partial\varphi(\boldsymbol{X}, t)}{\partial t}\right|_{\boldsymbol{X}} = \left.\frac{\partial\boldsymbol{u}(\boldsymbol{X}, t)}{\partial t}\right|_{\boldsymbol{X}} \equiv \dot{\boldsymbol{u}}(\boldsymbol{X}, t). \tag{A.3}$$

The conservation laws require the time derivatives of the field and state variables. The material time derivative of a state variable ϑ in the Lagrangian frame is:

$$\dot{\vartheta}(\boldsymbol{X}, t) = \left.\frac{\partial\vartheta(\boldsymbol{X}, t)}{\partial t}\right|_{\boldsymbol{X}}. \tag{A.4}$$

The chain rule is used to find the material time derivative in an Eulerian frame. The material time derivative of the state variable in the spatial coordinates $\boldsymbol{x}$ is obtained by the chain rule,

$$\frac{\mathrm{d}\vartheta(\boldsymbol{x}, t)}{\mathrm{d}t} = \left.\frac{\partial\vartheta(\boldsymbol{x}, t)}{\partial t}\right|_{\boldsymbol{x}} + \frac{\partial\vartheta(\boldsymbol{x}, t)}{\partial x}\frac{\partial\boldsymbol{x}}{\partial t} = \left.\frac{\partial\vartheta(\boldsymbol{x}, t)}{\partial t}\right|_{\boldsymbol{x}} + \boldsymbol{v}\cdot\vec{\nabla}\vartheta(\boldsymbol{x}, t), \tag{A.5}$$

where $\vec{\nabla}$ is the pre–gradient operator and $\boldsymbol{v}$ is the spatial velocity. The last part on the right hand side of equation (A.5) is referred to as the convective term.

A variable is not connected to the material or the current position in the referential description. The current position is expressed as a function of the referential position and time. The referential displacement becomes:

$$\boldsymbol{u_g} = \boldsymbol{u_g}(\boldsymbol{\chi}, t) = \hat{\varphi}(\boldsymbol{\chi}, t) - \hat{\varphi}(\boldsymbol{\chi}, t = 0), \tag{A.6}$$

where g indicates the referential frame or grid. The referential or grid velocity is defined as:

$$\boldsymbol{v_g} = \frac{\mathrm{d}\hat{\varphi}(\boldsymbol{\chi}, t)}{\mathrm{d}t} = \left.\frac{\partial\hat{\varphi}(\boldsymbol{\chi}, t)}{\partial t}\right|_{\boldsymbol{\chi}}. \tag{A.7}$$

The material time derivative of a state variable ϑ in the referential frame is:

$$\frac{\mathrm{d}\vartheta(\boldsymbol{\chi}, t)}{\mathrm{d}t} = \left.\frac{\partial\vartheta(\boldsymbol{\chi}, t)}{\partial t}\right|_{\boldsymbol{\chi}} + \boldsymbol{v_c} \cdot \vec{\nabla}\vartheta(\boldsymbol{\chi}, t), \tag{A.8}$$

in which the convective velocity $\boldsymbol{v_c}$ is:

$$\boldsymbol{v_c} = \boldsymbol{v} - \boldsymbol{v_g}, \tag{A.9}$$

and $\boldsymbol{v}$ is the material velocity.

The Lagrangian and Eulerian description basically are a special case of the referential description. The Lagrangian and Eulerian description are obtained when $\boldsymbol{\chi}$ equals $\boldsymbol{X}$ and $\boldsymbol{x}$ respectively.

A.1.2 Deformation

The deformation gradient $\underline{F}$ is the relation between the spatial configuration of a material particle and its reference configuration:

$$\underline{F}(\boldsymbol{X}, t) \equiv \frac{\partial \boldsymbol{x}}{\partial \boldsymbol{X}} = \boldsymbol{x}\overleftarrow{\nabla}_o \tag{A.10}$$

where $\overleftarrow{\nabla}_o$ is the post–gradient operator with respect to the initial configuration or material gradient. The determinant of $\underline{F}$, or Jacobian determinant, provides the relation for the change in volume between the current and reference configuration.

Taking the material time derivative of the deformation gradient $\underline{F}$ gives:

$$\dot{\underline{F}} = \frac{\partial}{\partial t}\frac{\partial \boldsymbol{x}}{\partial \boldsymbol{X}} = \frac{\partial \boldsymbol{v}}{\partial \boldsymbol{X}} = \frac{\partial \boldsymbol{v}}{\partial \boldsymbol{x}}\frac{\partial \boldsymbol{x}}{\partial \boldsymbol{X}} = \boldsymbol{v}\overleftarrow{\nabla} \cdot \underline{F} \tag{A.11}$$

From this equation, the velocity gradient $\underline{L}$ is defined as:

$$\underline{L} = \boldsymbol{v}\overleftarrow{\nabla} = \frac{\partial \boldsymbol{v}}{\partial \boldsymbol{x}} = \dot{\underline{F}} \cdot \underline{F}^{-1} \tag{A.12}$$

As any tensor, also the velocity gradient can be decomposed into a symmetric and a skew symmetric part, or:

$$\underline{L} = \underline{D} + \underline{W} \tag{A.13}$$

The symmetric part $\underline{D}$, or spatial rate-of-deformation, is defined as:

$$\underline{D} = \tfrac{1}{2}(\underline{L} + \underline{L}^{\mathrm{T}}) \tag{A.14}$$

or

$$\underline{D} = \tfrac{1}{2}(\boldsymbol{v}\overleftarrow{\nabla} + \vec{\nabla}\boldsymbol{v}),$$

and the skew symmetric spin tensor $\underline{W}$ is:

$$\underline{W} = \tfrac{1}{2}(\underline{L} - \underline{L}^{\mathrm{T}}) \tag{A.15}$$

or

$$\underline{W} = \tfrac{1}{2}(\boldsymbol{v}\overleftarrow{\nabla} - \vec{\nabla}\boldsymbol{v}).$$

A.1.3 Vector kinematics

In the material model, the fibres are represented as vectors $\boldsymbol{a}(\boldsymbol{x}, t)$, moving with the material in time. The current state of the fibres can be related to the deformation gradient and the initial state as:

$$\boldsymbol{a} = \underline{F} \cdot \boldsymbol{a}_o \tag{A.16}$$

The rate of change in $\boldsymbol{a}$ is the derivative of $\boldsymbol{a}$ to time or:

$$\begin{aligned} \frac{\partial \boldsymbol{a}}{\partial t} &= \frac{\partial}{\partial t}(\underline{F} \cdot \boldsymbol{a}_o) \\ &= \underline{\dot{F}} \cdot \boldsymbol{a}_o \\ &= \underline{\dot{F}} \cdot \underline{F}^{-1} \cdot \boldsymbol{a} \end{aligned} \tag{A.17}$$

and with relation (A.12):

$$\frac{\partial \boldsymbol{a}}{\partial t} = \underline{L} \cdot \boldsymbol{a} \tag{A.18}$$

These vectors change of length in time. The following normalised vector:

$$\boldsymbol{a}^* = \frac{\boldsymbol{a}}{\|\boldsymbol{a}\|} \qquad \text{where } \|\boldsymbol{a}\| = (\boldsymbol{a} \cdot \boldsymbol{a})^{\frac{1}{2}} \tag{A.19}$$

will not change in length. The rate of change in length will always be zero and can be found via the chain-rule:

$$\begin{aligned} \frac{\mathrm{D}}{\mathrm{D}t}\boldsymbol{a}^* &= \frac{\partial}{\partial t}\left(\frac{\boldsymbol{a}}{\|\boldsymbol{a}\|}\right) \\ &= \frac{\partial}{\partial t}\left(\frac{1}{\|\boldsymbol{a}\|}\right)\boldsymbol{a} + \frac{1}{\|\boldsymbol{a}\|}\frac{\partial}{\partial t}(\boldsymbol{a}) \end{aligned} \tag{A.20}$$

the first term in equation (A.20) becomes:

$$\begin{aligned} \frac{\partial}{\partial t}\left(\frac{1}{\|\boldsymbol{a}\|}\right)\boldsymbol{a} &= \frac{\partial}{\partial t}(\boldsymbol{a} \cdot \boldsymbol{a})^{-\frac{1}{2}}\boldsymbol{a} \\ &= -\tfrac{1}{2}(\boldsymbol{a} \cdot \boldsymbol{a})^{-\frac{3}{2}}\frac{\partial}{\partial t}(\boldsymbol{a} \cdot \boldsymbol{a})\,\boldsymbol{a} \\ &= -\tfrac{1}{2}(\boldsymbol{a} \cdot \boldsymbol{a})^{-\frac{3}{2}}2\boldsymbol{a} \cdot \frac{\partial}{\partial t}(\boldsymbol{a})\,\boldsymbol{a} \\ &= -\frac{1}{\|\boldsymbol{a}\|^3}\boldsymbol{a} \cdot \frac{\partial}{\partial t}(\boldsymbol{a})\,\boldsymbol{a} \\ &= -\frac{1}{\|\boldsymbol{a}\|^3}(\boldsymbol{a} \cdot \underline{L} \cdot \boldsymbol{a})\,\boldsymbol{a} \end{aligned} \tag{A.21}$$

and the second term is:

$$\frac{1}{\|\boldsymbol{a}\|}\frac{\partial}{\partial t}(\boldsymbol{a}) = \frac{1}{\|\boldsymbol{a}\|}\underline{L}\cdot\boldsymbol{a} \tag{A.22}$$

thus equation (A.20) evolves to:

$$\begin{aligned}\frac{\mathrm{D}}{\mathrm{D}t}\boldsymbol{a}^* &= \frac{1}{\|\boldsymbol{a}\|}\underline{L}\cdot\boldsymbol{a} - \frac{1}{\|\boldsymbol{a}\|^3}(\boldsymbol{a}\cdot\underline{L}\cdot\boldsymbol{a})\,\boldsymbol{a}\\ &= (\underline{I} - \boldsymbol{a}^*\boldsymbol{a}^*)\cdot\underline{L}\cdot\boldsymbol{a}^*\end{aligned} \tag{A.23}$$

A.2 Strain measures

Knowing the deformation of a continuum, a strain measure can be derived. In the reference configuration of the continuum in a Lagrangian description of motion, a vector $d\boldsymbol{x}_o$ deforms to a vector $d\boldsymbol{x}$ in the current configuration. The length ratio of the vector, the stretch λ, is defined as:

$$\begin{aligned}\lambda &= \frac{\|d\boldsymbol{x}\|}{\|d\boldsymbol{x}_o\|} = \frac{\sqrt{d\boldsymbol{x}\cdot d\boldsymbol{x}}}{\sqrt{d\boldsymbol{x}_o\cdot d\boldsymbol{x}_o}}\\ &= \frac{\sqrt{d\boldsymbol{x}_o\cdot\underline{F}^{\mathrm{T}}\cdot\underline{F}\cdot d\boldsymbol{x}_o}}{\sqrt{d\boldsymbol{x}_o\cdot d\boldsymbol{x}_o}}\\ &= \sqrt{\boldsymbol{a}_o\cdot\underline{F}^{\mathrm{T}}\cdot\underline{F}\cdot\boldsymbol{a}_o}\end{aligned} \tag{A.24}$$

where $\boldsymbol{a}_o$ is the orientation of the vector $d\boldsymbol{x}_o$ in the original configuration. The right Cauchy–Green deformation tensor $\underline{C}$ is defined as:

$$\underline{C} = \underline{F}^{\mathrm{T}}\cdot\underline{F} \tag{A.25}$$

The right Cauchy–Green deformation tensor is invariant under ridged body rotations. The left Cauchy–Green deformation tensor $\underline{B}$ or Finger tensor is objective, and also related to the deformation gradient tensor by:

$$\underline{B} = \underline{F}\cdot\underline{F}^{\mathrm{T}} \tag{A.26}$$

Both the Cauchy deformation tensors are measures of strain since they map the length of an infinitesimal vector $d\boldsymbol{x}_o$ into the vector $d\boldsymbol{x}$. Both equal the unit tensor if no deformation is applied.

A strain that vanishes with no deformation is more frequently used in engineering. Considering the length difference before and after deformation:

$$\begin{aligned}d\boldsymbol{x}\cdot d\boldsymbol{x} - d\boldsymbol{X}\cdot d\boldsymbol{X} &= (\underline{C} - \underline{I}) : d\boldsymbol{X}d\boldsymbol{X} = 2\underline{E} : d\boldsymbol{X}d\boldsymbol{X}\\ &= (\underline{I} - \underline{B}^{-1}) : d\boldsymbol{X}d\boldsymbol{X} = 2\underline{e} : d\boldsymbol{X}d\boldsymbol{X}\end{aligned}\text{,} \tag{A.27}$$

where $\underline{E}$ is the Green–Lagrange strain tensor and $\underline{e}$ is the Euler–Almansi strain tensor. Both tensors approach the classical linear strain tensor $\underline{\varepsilon}$ when the displacements are small, it reads:

$$\underline{\varepsilon} = \tfrac{1}{2}(\boldsymbol{u}\overleftarrow{\nabla} + \vec{\nabla}\boldsymbol{u}) \approx \underline{E} \approx \underline{e}. \tag{A.28}$$

A.3 Stress measures

Many stress definitions can be found in the literature. One of the most commonly used stresses is the Cauchy or true stress $\underline{\sigma}$. The Cauchy stress tensor is defined in the deformed state and is objective and symmetrical. The stress is determined from the Cauchy law:

$$\underline{\sigma} \cdot \boldsymbol{n}\, d\Gamma_c = d\boldsymbol{f} \tag{A.29}$$

where $\boldsymbol{n}$ is the outward normal vector on the infinitesimal surface $d\Gamma_c$ and $d\boldsymbol{f}$ is the force acting on $d\Gamma_c$ (see figure A.2). The traction $\boldsymbol{t}$ is defined as:

$$\boldsymbol{t} = \frac{d\boldsymbol{f}}{d\Gamma_c}. \tag{A.30}$$

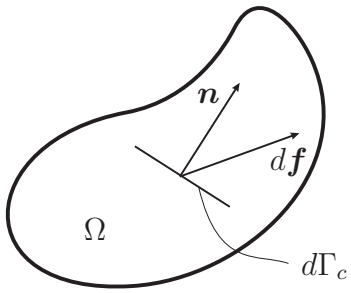

Figure A.2: Body force vector $d\boldsymbol{f}$ acting on infinitesimal surface $d\Gamma_c$.

The hydrostatic pressure can is found from the Cauchy stress tensor, it is defined as:

$$p = -\tfrac{1}{3}\,\mathrm{tr}\,\underline{\sigma}, \tag{A.31}$$

where $\mathrm{tr}\,\underline{\sigma}$ represents the trace of $\underline{\sigma}$, or its first invariant. The deviatoric stress can be found from:

$$\underline{\sigma}^d = \underline{\sigma} - \tfrac{1}{3}\,\mathrm{tr}\,\underline{\sigma I} = \underline{\sigma} + p\,\underline{I} \tag{A.32}$$

A.4 The equilibrium problem

Thermo–mechanical processes must obey conservation laws. These conservation laws are the *conservation of mass*, *linear momentum*, *angular momentum* and *energy* and must hold at any position in the continuum. They result in the following equations:

$$\begin{aligned}
-\rho\,\boldsymbol{v} \cdot \overleftarrow{\nabla} &= \dot{\rho}, && \text{(A.33a)}\\
\underline{\sigma} \cdot \overleftarrow{\nabla} + \rho\boldsymbol{f} &= \rho\,\dot{\boldsymbol{v}}, && \text{(A.33b)}\\
\underline{\sigma} &= \underline{\sigma}^T, && \text{(A.33c)}\\
\underline{\sigma} : \underline{D} - \boldsymbol{q} \cdot \overleftarrow{\nabla} + \rho r &= \rho\,\dot{u}_{int}, && \text{(A.33d)}
\end{aligned}$$

where ρ is the mass density, $\boldsymbol{v}$ the velocity, $\underline{\sigma}$ is the Cauchy stress, $\boldsymbol{f}$ is the body force per unit of mass, $\underline{D}$ is the rate-of-deformation, $\boldsymbol{q}$ is the heat flux and r is the heat production per unit of mass. The superimposed dot represents the material time derivative.

The material velocities in forming processes are generally relatively low. Therefore inertia effects can be neglected. When also neglecting the thermal effects during forming, only the momentum equilibrium remains from equation (A.33), or:

$$\underline{\sigma} \cdot \overleftarrow{\nabla} + \rho \boldsymbol{f} = \boldsymbol{0}, \tag{A.34a}$$

$$\underline{\sigma} = \underline{\sigma}^T. \tag{A.34b}$$

When $\underline{\sigma}$ is symmetrical and can be expressed as a function of the strain and strain history, and this strain can be expressed as a function of the displacements $\boldsymbol{u}$ of the domain, the objective is to solve a displacement field $\boldsymbol{u}$ that fulfills mechanical equilibrium condition (A.34) and the the boundary conditions on the surface Γ of the domain Ω, or:

$$\underline{\sigma} \cdot \overleftarrow{\nabla} + \rho \boldsymbol{f} = \boldsymbol{0} \quad \text{in} \quad \Omega, \tag{A.35a}$$

$$\boldsymbol{u} - \boldsymbol{u}_u = \boldsymbol{0} \quad \text{on} \quad \Gamma_u, \tag{A.35b}$$

$$\underline{\sigma} \cdot \boldsymbol{n} - \boldsymbol{t} = \boldsymbol{0} \quad \text{on} \quad \Gamma_t, \tag{A.35c}$$

where Γ_u is the part of the boundary where the displacements $\boldsymbol{u}_u$ are described, Γ_t is the part of the boundary where the tractions $\boldsymbol{t}$ are described and $\boldsymbol{n}$ is the normal vector at the boundary. Equation (A.35) is often referred to as the strong form of mechanical equilibrium.

A.4.1 Weak form

The strong form of equilibrium requires a continuous distribution of the stress in the domain. For numerical purposes, the stringent strong form is weighted by arbitrary weight functions $\delta \boldsymbol{w}$ to obtain a less constraint form. As a result, a discretised form, or weak form, of the strong form of equilibrium is solved.

When integrating the strong form equations over their individual domains and weighting them by an arbitrary weight functions $\delta \boldsymbol{v}$, the result is:

$$\delta P = \int_\Omega \delta \boldsymbol{w} \cdot (\underline{\sigma} \cdot \overleftarrow{\nabla})\, d\Omega + \int_\Omega \rho \delta \boldsymbol{w} \cdot \boldsymbol{f}\, d\Omega - \int_\Gamma \delta \boldsymbol{w} \cdot (\underline{\sigma} \cdot \boldsymbol{n} - \boldsymbol{t})\, d\Gamma \equiv 0. \tag{A.36}$$

Expanding the derivative of the first multiplication leads to:

$$\delta \boldsymbol{w} \cdot (\underline{\sigma} \cdot \overleftarrow{\nabla}) = (\delta \boldsymbol{w} \cdot \underline{\sigma}) \cdot \overleftarrow{\nabla} - (\delta \boldsymbol{w} \cdot \overleftarrow{\nabla}) : \underline{\sigma}. \tag{A.37}$$

Applying the divergence theorem of Gauss, the weak form of the mechanical equilibrium equation becomes (with a sign change):

$$\int_\Omega \delta \boldsymbol{w} \overleftarrow{\nabla} : \underline{\sigma}\, d\Omega = \int_\Omega \delta \boldsymbol{w} \cdot \rho \boldsymbol{f}\, d\Omega + \int_\Gamma \delta \boldsymbol{w} \cdot \boldsymbol{t}\, d\Gamma. \tag{A.38}$$

In this form the stress, and not the derivative of the stress is required, and can be discontinuous in the domain. Using (A.12) and (A.13) the first term of (A.38) is often expressed in the following form:

$$\begin{aligned} \int_\Omega \delta \boldsymbol{w} \overleftarrow{\nabla} : \underline{\sigma}\, d\Omega &= \int_\Omega \delta \underline{L} : \underline{\sigma}\, d\Omega \\ &= \int_\Omega \delta (\underline{D} + \underline{W}) : \underline{\sigma}\, d\Omega \\ &= \int_\Omega \delta \underline{D} : \underline{\sigma}\, d\Omega. \end{aligned} \tag{A.39}$$

The skew symmetric part of the velocity gradient tensor, the spin tensor, vanishes from equation (A.39), since it does not contribute to the energy.

Appendix B

Material model implementation

B.1 Single layer fibre update

The fibre update for each fabric layer is done in the natural coordinates of the triangular element. The fibre directions are set as input in the global coordinates. The initial fibre directions for the warp and weft fibres are set at $[\frac{1}{2}\sqrt{2}, \frac{1}{2}\sqrt{2}]$ and $[\frac{1}{2}\sqrt{2}, -\frac{1}{2}\sqrt{2}]$ in the example shown here. The triangular element with the corner nodes $[0, 0]$, $[1, 1]$ and $[0, 2]$ is deformed from its original configuration into the current situation shown at the right hand side of figure B.1.

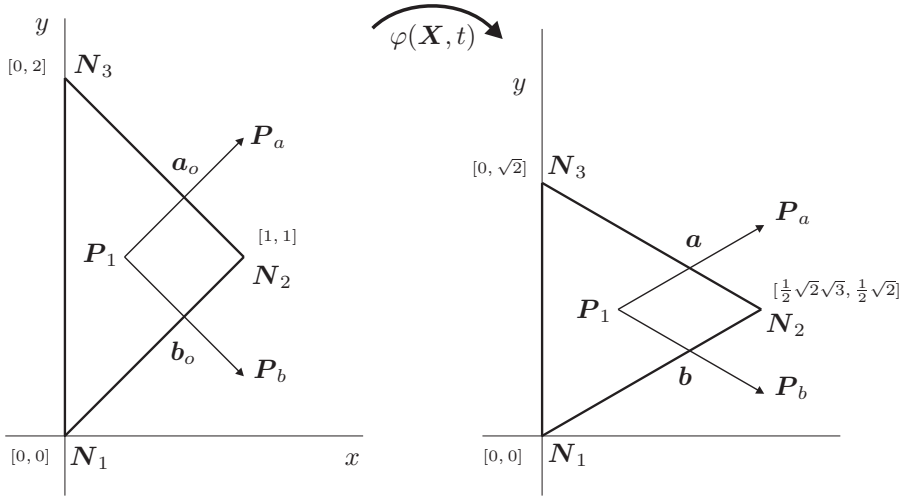

Figure B.1: Triangular element deforming resulting in a fibre reorientation.

The fibre directions of the fibre families are stored at the integration point $\boldsymbol{P}_I$ in the initial configuration, located at $[\frac{1}{3}, 1]$. Fibre family a initially points from the integration point to point $\boldsymbol{P}_a$, located at $[\frac{1}{3} + \frac{1}{2}\sqrt{2}, 1 + \frac{1}{2}\sqrt{2}]$ in xy–coordinates. The global xy–coordinates relate to the elements triangular coordinates $\boldsymbol{\xi}$ by:

$$\begin{aligned} x &= N_{1x}\xi_1 + N_{2x}\xi_2 + N_{3x}\xi_3 \\ y &= N_{1y}\xi_1 + N_{2y}\xi_2 + N_{3y}\xi_3 \end{aligned}, \tag{B.1}$$

with $\xi_1 + \xi_2 + \xi_3 = 1$. Using this relation, Point $\boldsymbol{P}_a$ is located at $[\frac{1}{3} - \frac{1}{2}\sqrt{2}, \frac{1}{3} + \frac{1}{2}\sqrt{2}, \frac{1}{3}]$ in triangular coordinates.

A change in nodal coordinates defines the element deformation. The fibre directions do also change, corresponding to the deformation within the elements. All points remain at the same position relatively to the nodes in the triangular element coordinates. So, the element integration point always remains at position $\boldsymbol{\xi} = [\frac{1}{3}, \frac{1}{3}, \frac{1}{3}]$ and position $\boldsymbol{P}_a$ at $[\frac{1}{3} - \frac{1}{2}\sqrt{2}, \frac{1}{3} + \frac{1}{2}\sqrt{2}, \frac{1}{3}]$. The resulting direction of vector $\boldsymbol{a}$ becomes $[\frac{1}{2}\sqrt{3}, \frac{1}{2}]$ in xy–coordinates. The length of vector $\boldsymbol{a}$ remains constant in this example. This is not necessary in general. An analogue relation hold for fibre family b.

B.2 Material tensor

Generally, $\underline{\sigma}$ is implemented in a Voigt notation. The tensor $\underline{\sigma}$ is then written as the vector $\{\sigma\}$:

$$\{\sigma\} = \begin{Bmatrix} \sigma_{11} \\ \sigma_{22} \\ \sigma_{33} \\ \sigma_{23} \\ \sigma_{13} \\ \sigma_{12} \end{Bmatrix}. \tag{B.2}$$

The material matrix $[M]$ for the single layer material model without plane–stress conditions reads:

$$[M] = [M_a] + [M_b] + [M_f] + [M_k] + [M_v], \tag{B.3}$$

where $[M_{a,b}]$ are the contributions of the fibre families a and b respectively, $[M_f]$ the contribution of the shear–locking, $[M_k]$ the contribution due to hydrostatic compression of the material and $[M_v]$ the contribution of the extra viscous stress.

The contribution of the fibres is modelled linearly elastic so the modulus of the fibres and their direction determines the contribution to the material matrix. The contribution of fibre family a in Voigt notation reads:

$$[M_a] = V_{f_a} [T_a]^{-1} \cdot [M_a] \cdot [T_a], \tag{B.4}$$

with the in–plane rotation matrix $[T_a]$ as:

$$[T_a] = \begin{bmatrix} a_1^2 & a_2^2 & 0 & 0 & 0 & -2a_1a_2 \\ a_2^2 & a_1^2 & 0 & 0 & 0 & 2a_1a_2 \\ 0 & 0 & 1 & 0 & 0 & 0 \\ 0 & 0 & 0 & a_1 & a_2 & 0 \\ 0 & 0 & 0 & -a_2 & a_1 & 0 \\ a_1a_2 & -a_1a_2 & 0 & 0 & 0 & a_1^2 - a_2^2 \end{bmatrix}, \tag{B.5}$$

and the material stiffness $[M_a]$ as:

$$[M_a] = \begin{bmatrix} E_a & 0 & 0 & 0 & 0 & 0 \\ 0 & 0 & 0 & 0 & 0 & 0 \\ 0 & 0 & 0 & 0 & 0 & 0 \\ 0 & 0 & 0 & 0 & 0 & 0 \\ 0 & 0 & 0 & 0 & 0 & 0 \\ 0 & 0 & 0 & 0 & 0 & 0 \end{bmatrix}. \tag{B.6}$$

Similarly, the material stiffness contribution of fibre family b is determined.

The contribution due to hydrostatic compression of the material $[M_k]$ reads:

$$[M_k] = V_m \begin{bmatrix} K & K & K & 0 & 0 & 0 \\ K & K & K & 0 & 0 & 0 \\ K & K & K & 0 & 0 & 0 \\ 0 & 0 & 0 & 0 & 0 & 0 \\ 0 & 0 & 0 & 0 & 0 & 0 \\ 0 & 0 & 0 & 0 & 0 & 0 \end{bmatrix}, \tag{B.7}$$

where K is the bulk modulus.

The extra viscous stress contribution is written as:

$$[M_v] = [M_\eta] + [M_{\eta_1}] + [M_{\eta_2}] + [M_{\eta_3}] + [M_{\eta_4}], \tag{B.8}$$

where $[M_{\eta,\eta_1,\eta_2,\eta_3,\eta_4}]$ are the viscosity contributions.

$$[M_\eta] = V_m \frac{\eta}{\Delta t} \begin{bmatrix} 2 & 0 & 0 & 0 & 0 & 0 \\ 0 & 2 & 0 & 0 & 0 & 0 \\ 0 & 0 & 2 & 0 & 0 & 0 \\ 0 & 0 & 0 & 1 & 0 & 0 \\ 0 & 0 & 0 & 0 & 1 & 0 \\ 0 & 0 & 0 & 0 & 0 & 1 \end{bmatrix}. \tag{B.9}$$

The contributions of the viscosities $\eta_{1,2,3,4}$ are determined by expansion of equation (2.19) and subsequently writing in Voigt notation. When additionally assuming that the fibres are in the plane of the composites, the results read:

$$[M_{\eta_1}] = V_m \frac{\eta_1^*}{\Delta t} \begin{bmatrix} 4a_1^2 & 0 & 0 & 0 & 0 & 2a_1a_2 \\ 0 & 4a_2^2 & 0 & 0 & 0 & 2a_1a_2 \\ 0 & 0 & 0 & 0 & 0 & 0 \\ 0 & 0 & 0 & a_2^2 & a_1a_2 & 0 \\ 0 & 0 & 0 & a_1a_2 & a_1^2 & 0 \\ 2a_1a_2 & 2a_1a_2 & 0 & 0 & 0 & a_1^2 + a_2^2 \end{bmatrix}, \tag{B.10}$$

$$[M_{\eta_2}] = V_m \frac{\eta_2^*}{\Delta t} \begin{bmatrix} 4b_1^2 & 0 & 0 & 0 & 0 & 2b_1b_2 \\ 0 & 4a_2^2 & 0 & 0 & 0 & 2b_1b_2 \\ 0 & 0 & 0 & 0 & 0 & 0 \\ 0 & 0 & 0 & b_2^2 & b_1b_2 & 0 \\ 0 & 0 & 0 & b_1b_2 & b_1^2 & 0 \\ 2b_1b_2 & 2b_1b_2 & 0 & 0 & 0 & b_1^2 + b_2^2 \end{bmatrix}, \tag{B.11}$$

$$[M_{\eta_3}] = V_m \frac{\eta_3^*}{\Delta t} \begin{bmatrix} 4a_1b_1 & 0 & 0 & 0 & 0 & 2a_1b_2 \\ 0 & 4a_2b_2 & 0 & 0 & 0 & 2a_2b_1 \\ 0 & 0 & 0 & 0 & 0 & 0 \\ 0 & 0 & 0 & a_2b_2 & a_2b_1 & 0 \\ 0 & 0 & 0 & a_2b_1 & a_1b_1 & 0 \\ 2a_1b_2 & 2a_2b_1 & 0 & 0 & 0 & a_1b_1 + a_2b_2 \end{bmatrix}, \tag{B.12}$$

$$[M_{\eta_4}] = V_m \frac{\eta_4^*}{\Delta t} \begin{bmatrix} 4a_1b_1 & 0 & 0 & 0 & 0 & 2a_2b_1 \\ 0 & 4a_2b_2 & 0 & 0 & 0 & 2a_1b_2 \\ 0 & 0 & 0 & 0 & 0 & 0 \\ 0 & 0 & 0 & a_2b_2 & a_1b_2 & 0 \\ 0 & 0 & 0 & a_1b_2 & a_1b_1 & 0 \\ 2a_2b_1 & 2a_1b_2 & 0 & 0 & 0 & a_1b_1 + a_2b_2 \end{bmatrix}. \tag{B.13}$$

Subsequently, the matrix $[M]$ is reduced by imposing plane stress conditions.

Appendix C

Drape material model verification

C.1 Molenkamp test

Here, the fibre directions are convected in a Molenkamp [78] test. The initial fibre directions are oriented as depicted in figure C.1, at 0°.

The material rotates 360° counterclockwise around the midpoint of the plate in 281 steps. The fibre distribution is shown at a few steps in the simulation: 0°, 90°, 180°, 270° and 360°. The fibre directions are normalised after each convective step. The initial fibre distribution are nearly preserved at the end of a full rotation. Some distortions in the orientations are observed at the sides of the plate. These result form the inflow condition at the sides of the plate.

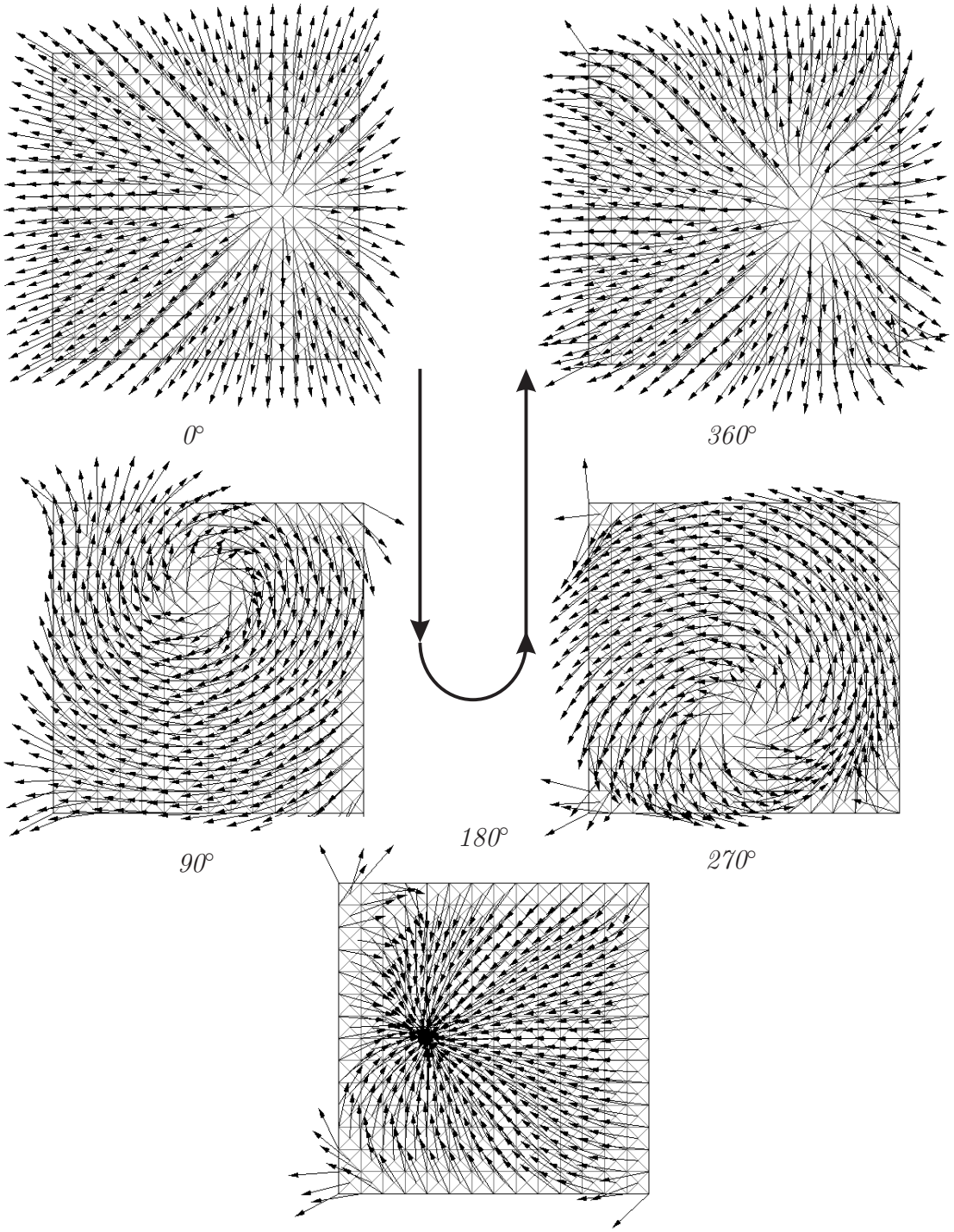

Figure C.1: Molenkamp test for fibre redistribution.

Appendix D

Drape applications

The single layer material model and multi–layer material models (section 2.2) were implemented in an implicit finite element code. The drape simulations were compared with experiments on the double dome geometry (section 3.6). Some examples of applications of the material models are given here.

D.1 Sphere

The forming of a hemispherical product is a widely used verification example for draping. The drape set–up for the hemispherical product is shown in figure D.1.

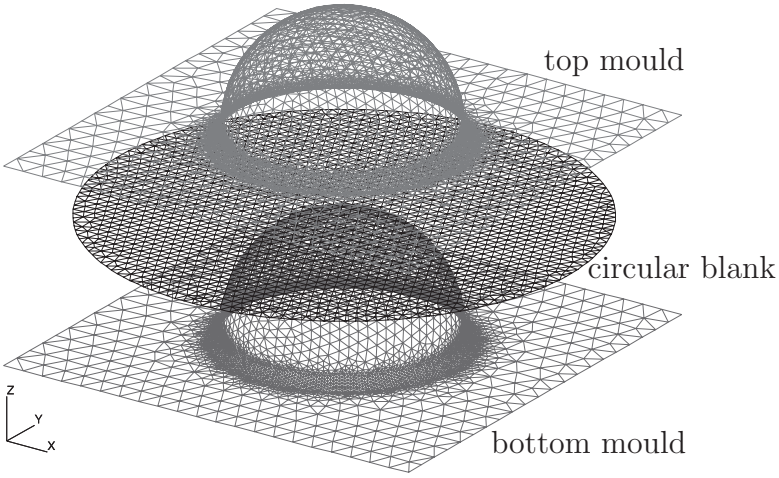

Figure D.1: Drape set–up for a hemispherical product; top mould, blank and bottom mould.

The meshes of the top mould, bottom mould and the blank are shown in figure D.1. The radius of the bottom mould was 89 mm while the radius of the top mould was 90 mm. The circular blank with a radius of 150 mm was placed between the moulds. The thickness of the blank was 1 mm. A mesh of 3886 triangular membrane elements was used to model the blank, resulting in a typical element side length of 6.5 mm.

The fibre directions were oriented to the x and y axes. The material properties used for draping are given in section 3.6.2. The press velocity was set at 500 mm/s. The drape results are shown in figure D.2.

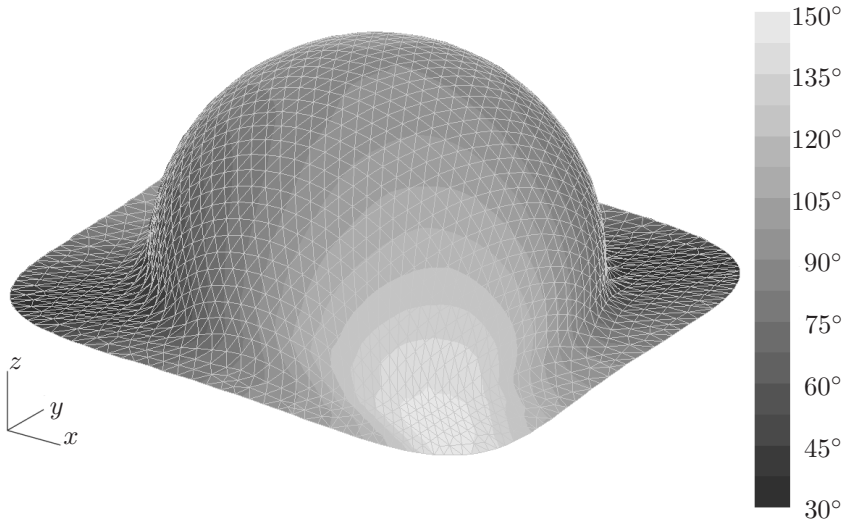

Figure D.2: Drape result for a hemispherical product: the enclosed fibre angle.

The hemispherical shape basically is a simplification of the double dome geometry. However, the resulting fibre redistribution is quite different. Large shear deformation occurs in the bias directions of the weave. The minimum enclosed fibre angle is approximately 30°. This angle is significantly smaller than the enclosed fibre angles in the double dome product. The smaller angle is caused by the increased double curvature in the hemispherical product due to the deeper product depth.

D.2 Cone

The draping of a conical product is also a widely used academic application, similarly to the hemispherical shape. The rubber pressed conical product and its dimensions are depicted in figure D.3.

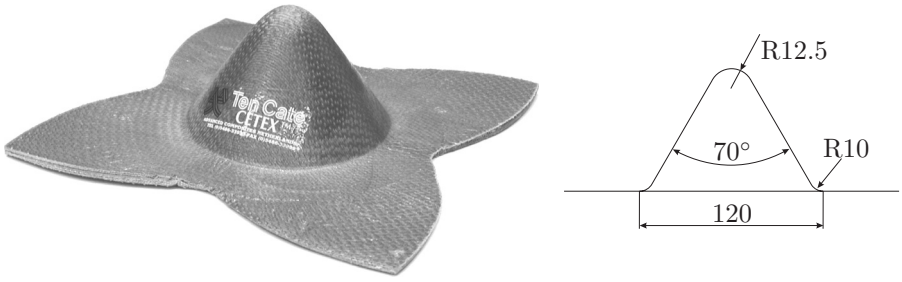

Figure D.3: Shape of the conical product. The dimensions are shown in mm.

A structured mesh of 10000 triangular elements is used to model the square blank of 250×250 mm^2. The press velocity during draping was set at a constant 500 mm/s, further input parameters for the drape simulations can be found in section 3.6. The initial fibre directions of the twill 3×1 weave composite were parallel to the sides of the blank and the thickness was 3.6 mm. All layers were orientated equally.

The top view of the deformed mesh after draping is shown in figure D.4. The edges of the elements indicate the occurring fibre re–arrangement. Good agreement is found for the modelled and the experimentally obtained contour of the product. The angle between the fibres reached a minimum of approximately 52°. Kinematic drape modelers can also predict the fibre reorientation pattern for an conical product well.

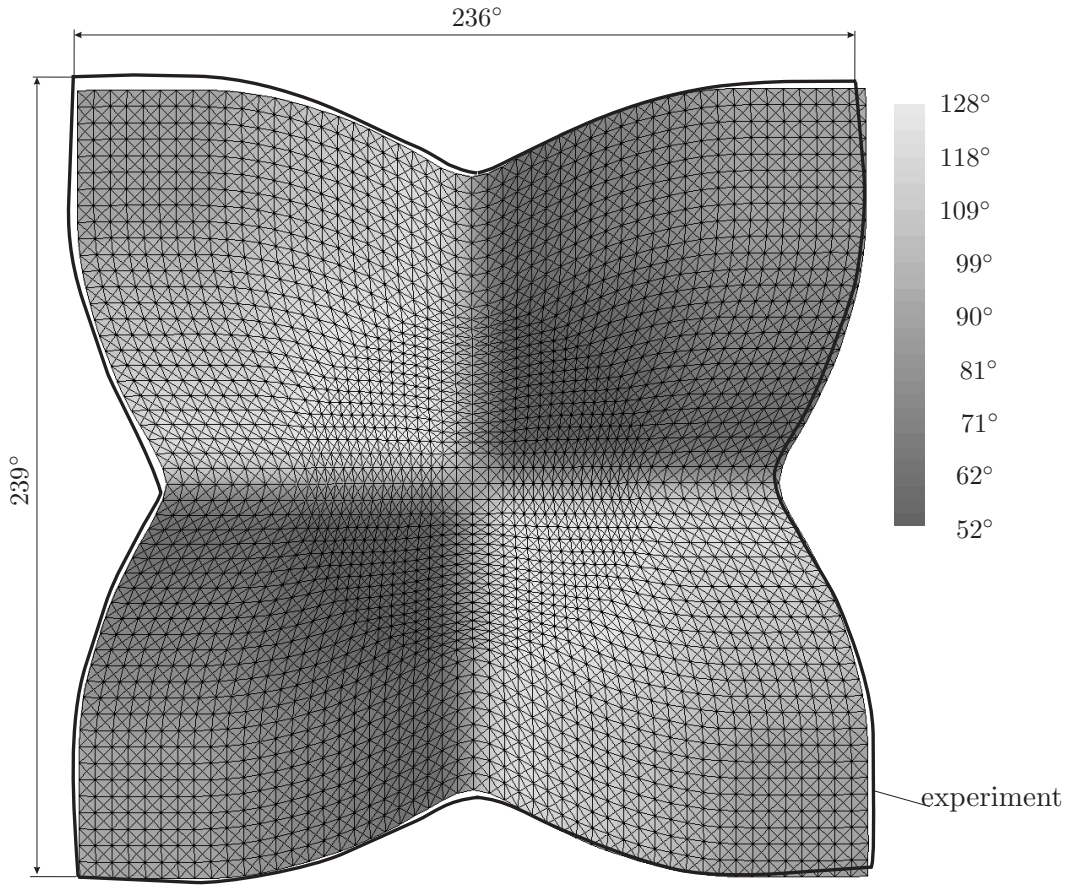

Figure D.4: Drape simulation versus shape of the conical product. The dimensions are shown in mm.

D.3 Rib

Lightweight shell shaped products are frequently applied in aerospace applications. Composite materials are used for ribs, stiffeners and skins in the last few years. An example of a composite application is the rib that stiffens the wing leading edge. The draping of a wing leading edge rib is modelled here. The drape set–up for the product is illustrated in figure D.5.

6500 membrane elements were used in the simulation. The Quasi Isotropic (QI) $[0°/90°|45°/\text{-}45°]_s$ laminate with a thickness of 0.9 mm was formed onto the mould using a constant velocity of 500 mm/s. The material input parameters are given in section 3.6.2. The enclosed fibre angles resulting from the simulation are given in figure D.6.

Both ply orientations of the QI lay–up do not shear more than 25°. Some extreme

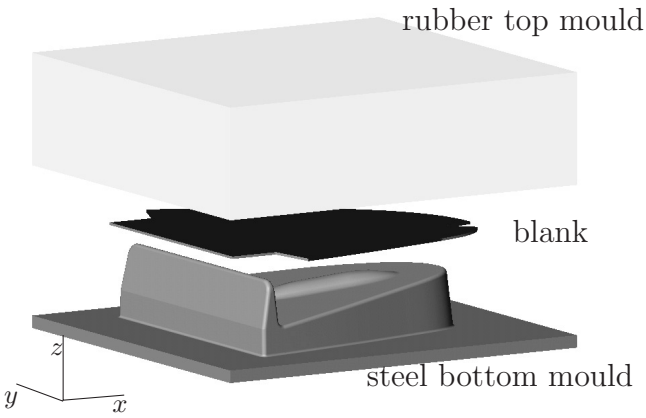

Figure D.5: Schematic view of the rib rubber press tooling and pre–form.

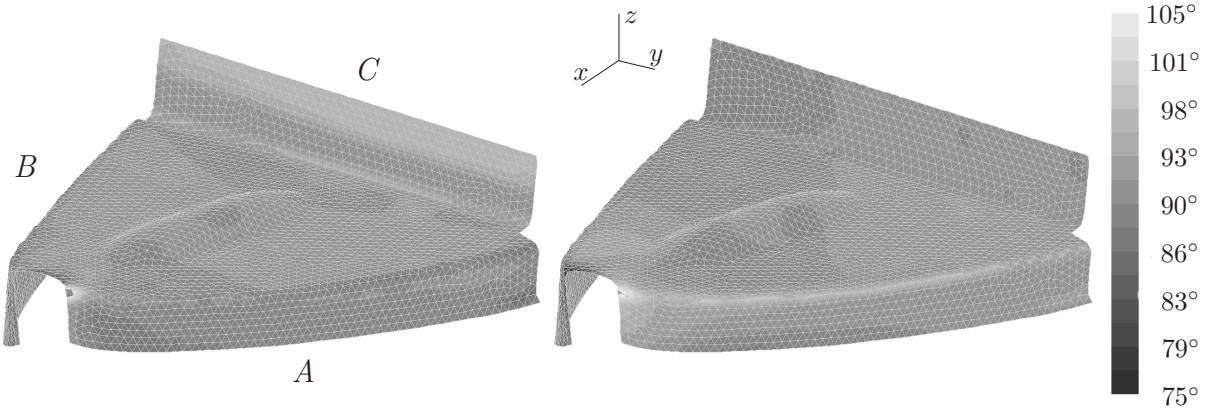

Figure D.6: Resulting fibre orientation for the QI lay–up; [0°/90°] *and* [45°/-45°] *layers, left and right picture respectively.*

deformations occur at the nose of the rib. Most deformation of both layers occurs in this area. The [45°/-45°] ply deforms extensively at the edges of the rib. Also shear deformations occurs for the [45°/-45°] layers in the vertical flanges A and B. The [0°/90°] layer does not deform significantly in the flange C. The [45°/-45°] plies do shear in this area, indicating ply slippage in this zone.

Acknowledgments

This project was made possible by the financial support of two research projects; the Brite Euram project *PRECIMOULD* and the Netherlands Agency for Aerospace Programs supported *High Precision Rubber Pressing* project. The partners of both projects are gratefully acknowledged. Additionally, I would like to thank Ten Cate Advanced Composites and Stork Fokker AESP for the pleasant co–operation during the last couple of years. I also would like to thank my colleagues in the Applied Mechanics group and the group of Productie Techniek for the enjoyable time I spent working with you.

The first person I want to thank is Remko Akkerman, my supervisor during this PhD project and my graduation project. His input is appreciated more than can be expressed in just a couple of words. I thank you Remko. The second person to say thanks to is Han Huétink, who let me work with his DiekA, and who gave me valuable support. Next, I would like to thank Sebastiaan Wijskamp, Richard Loendersloot, Laurent Warnet, Timo Meinders and Peter Reed for carefully reading my manuscript and their valuable comments.

Of course, my roommates, Sebastiaan, Richard and Rene. I have enjoyed the many interesting discussions, coffee breaks, beers in sometimes distant countries with you. Thanks.

Some other persons also deserve attention, Belinda, Debbie and Tanja, thank you for doing the necessary secretarial work. Also many thanks to Herman and Nico for and keeping the computers in shape and their programming support.

I would like to thank my family for their support, interest and encouragement. Last but most important, Berdie, Monique and Claudia, thank you for letting me finish this one. I know that I did not spent that much time with you lately, but you did not complain. Papa gaat nu eventjes minder werken.

About the author

The author was born on the second of september 1972 in Hengelo, the Netherlands. After graduating from the secondary school 'MAVO Woolde' in the same village in 1988, he entered the middle educational technical school 'Hofstede MTS'. He finished the theoretical educational program of the mechanical engineering study in 1991, where after he started the mechanical engineering study at the higher educational technical school 'Hogeschool Enschede'. After finishing his foundation course he entered the University of Twente in September 1992, studying again mechanical engineering.

He graduated on the temperature dependent properties of fibre reinforced plastics in 1998, after choosing the engineering in plastics group to do his final project in. He started working in the section of applied mechanics and polymers group in the brite Euram program *Precimould* on precision moulding of thermosetting composite materials. A few years later, a national research project named *High Precision Rubber Pressing* was initiated in 2001 in order to solve similar production related dimensional accuracy problems with thermoplastic composites. His PhD study was performed in the scope of these research projects.